Imaging vortex pinning and gyration by time-resolved and in-situ Lorentz microscopy

Dissertation

for the award of the degree

"Doctor rerum naturalium" (Dr.rer.nat.)

of the Georg-August-Universität Göttingen

within the doctoral program Physics

of the Georg-August University School of Science (GAUSS)

submitted by

Marcel Möller

from Fulda

Göttingen, 2022

Thesis advisory committee

Prof. Dr. Claus Ropers, IV. Physical Institute
and Max Planck Institute for Multidisciplinary Sciences

Prof. Dr. Stefan Mathias, I. Physical Institute

Dr. Henning Ulrichs, I. Physical Institute

Members of the examination board

Referee: Prof. Dr. Claus Ropers, IV. Physical Institute
and Max Planck Institute for Multidisciplinary Sciences

Co-referee: Prof. Dr. Stefan Mathias, I. Physical Institute

Other members of the examination board

Prof. Dr. Timo Betz, III. Physical Institute

Prof. Dr. Matthias Krüger, Institute of Theoretical Physics

Prof. Dr. Thomas Weitz, I. Physical Institute

Dr. Daniel Steil, I. Physical Institute

Day of the oral examination: August 30th, 2022

To Simone and Jona

Acknowledgements

I am grateful to everyone who has helped me throughout my PhD journey. Without their support, encouragement, and guidance, this thesis would not have been possible.

First and foremost, I would like to express my sincere gratitude to my supervisor Prof. Dr. Claus Ropers, for his enduring mentorship, insightful feedback, and patient guidance. I have learned so much from him and am grateful for the opportunity to work under his supervision.

I am also grateful to the members of my thesis committee, Prof. Dr. Stefan Mathias, and Dr. Henning Ulrichs, for their constructive feedback and suggestions. Their insights have helped me to improve the quality of this thesis.

Special thanks go to my colleague John Henri Gaida. His contribution was invaluable and his expertise and insights were instrumental in the successful completion of my research projects.

I would like to extend my appreciation to my other colleagues Thomas Danz, Armin Feist, Till Domröse, Nora Bach and Karin Ahlborn, for their friendship and support throughout my PhD journey. Their encouragement and advice have been invaluable.

Many thanks to my colleague Benjamin Schröder, who generously volunteered his time and expertise to proofread this thesis. His suggestions and attention to detail greatly improved the quality of this work.

To my beloved wife Simone and our wonderful son Jona, I am eternally grateful for their unflagging love and support. Their presence in my life has been a constant source of joy and motivation.

I am deeply thankful to my late father Werner and my mother Renate for their unwavering support. My father's passing during my PhD was a difficult time for me, but his memory and the values he instilled in me have continued to inspire and motivate me.

Abstract

Magnetism encompasses a large variety of scientifically interesting and industrially valuable phenomena. In particular, nanoscopic magnetic textures—such as vortices, merons and skyrmions—have been in the spotlight of contemporary research, due to various possible applications, such as three-dimensional memory, logic gates or neuromorphic computing. Studying the control of such textures employing electric, magnetic or optical fields, demands instruments with sufficient spatial and temporal resolution. With the development of high-brightness electron sources, ultrafast transmission electron microscopy was established as an essential tool for the study of optically-driven magnetization dynamics. Yet, its potential to probe current- or field-driven dynamics of magnetic textures remained unexplored.

In the first publication of this cumulative thesis, I and my coworkers use Lorentz microscopy in the Göttingen Ultrafast Transmission Electron Microscope to image the time-resolved gyration of a vortex in a magnetic nanostructure driven by radio-frequency currents. We demonstrate tracking of the vortex core with a localization precision of ± 2 nm with an electron pulse duration < 3 ps at few-minute integration time. In studying the decay of the gyration after the sudden removal of the driving current, we find a transient change in the frequency and damping of the core orbit, attributed to disorder in the sample.

The second study combines conventional and time-resolved Lorentz microscopy with bright-field imaging of the magnetic vortex nanostructures to identify the origin of this disorder. A comprehensive study of the time-resolved gyration is enabled by the implementation of a novel photoemission source, reducing the image acquisition time by multiple orders of magnitude. Furthermore, a new method for probing static pinning sites in magnetic nanostructures is developed, that allows for the reconstruction of the underlying pinning potential. The comparisons of the time-resolved and conventional results with bright-field images suggest grain boundaries in the polycrystalline film to be one source of pinning.

Contents

List of Figures

List of Abbreviations

AWG	arbitrary waveform generator
DPC	differential phase contrast
DTEM	dynamic transmission electron microscopy
CMOS	complementary metal-oxide-semiconductor
FWHM	full width at half maximum
LLG	Landau-Lifshitz-Gilbert
MOKE	magneto-optic Kerr effect
RF	radio-frequency
STT	spin-transfer torque
STEM	scanning transmission electron microscopy
STXM	scanning transmission X-ray microscopy
TEM	transmission electron microscopy
TRaPS	TEM rastering of pinning sites
UTEM	ultrafast transmission electron microscopy

Nomenclature

A	isotropic dilation factor	
A_{ex}	exchange stifness	$\mathrm{J\,m^{-1}}$
α_x, α_y	tilt angle along x and y axis	$^\circ$
$\mathbf{B}$	magnetic flux density	T
c	vortex curl	
χ	vortex displacement susceptibility	$\mathrm{m^2\,A^{-1}}$
$\tilde{\chi}$	modified displacement susceptibility $\tilde{\chi} = H\chi$	$\mathrm{m}/^\circ$
D	vortex core orbit diameter	m
Δf	objective lens defocus	m
$\mathbf{e}_i$	uni vector along i	
E_{pin}	depth of the pinning potential at a single pinning site	eV
$E_{\mathrm{pin,all}}$	sum of the individual pinning potentials	eV
E_{quad}	energy of the vortex in a quadratic potential	eV
E_{total}	total vortex potential, i.e. $E_{\mathrm{total}} = E_{\mathrm{quad}} + E_{\mathrm{pin,all}}$	eV
f_0	free oscillation frequency	Hz
f_{ex}	external driving frequency	Hz

$\mathbf{F}_\mathrm{L}$	Lorentz Force	N
f_r	resonace frequency	Hz
f_rep	repetition rate of the photoemission laser	Hz
Γ	exponential damping parameter	s^{-1}
H	magnetic field strength	$\mathrm{A\,m}^{-1}$
I_S	sample current	$\mathrm{A_{rms}}$
j	electrical current density	$\mathrm{A_{rms}\,m}^{-2}$
k	stiffness factor of the quadratic vortex potential	$\mathrm{eV\,m}^{-2}$
$\mathbf{M}$	magnetization	$\mathrm{A\,m}^{-1}$
M_S	saturation magnetization	$\mathrm{A\,m}^{-1}$
Ω	angular velocity of external driving frequency	$\mathrm{rad\,s}^{-1}$
ω	angular velocity of free oscillation frequency	$\mathrm{rad\,s}^{-1}$
p	vortex polarity	
φ	excitation phase relative to the electron probe pulse	rad
φ_AB	Aharonov-Bohm phase shift	rad
$\varphi_\mathrm{M}, \varphi_\mathrm{E}$	magnetic and electric component of the Aharonov-Bohm phase shift	rad
$\hat{R}$	rotation matrix	
r_med	median radial deviation	m
σ_pin	width of a single pinning potential	m
t	time delay	s
v_C	velocity of the vortex core	$\mathrm{m\,s}^{-1}$
$\mathbf{v}_e$	electron velocity	$\mathrm{m\,s}^{-1}$
X, Y	position coordinates of the vortex core	m
ξ	non-adiabaticity parameter	
x, y, z	axes of the coordinate system	

1

Introduction

The rapid progress of our modern information society is based on a progressive reduction and acceleration of technological components. This goes hand in hand with the ongoing search for new technological approaches to sustain this trend. The field of magnetism is here considered a beacon of hope as it gives rise to a rich set of nanoscale phenomena. Especially magnetic textures like vortices [1, 2], (anti-)skyrmions [3–6] and merons [7–9] have seen sustained interest in recent research. Possible technological applications utilizing such textures range from racetrack memorys [10–12], over logic gates [13, 14], and neuromorphic computing [15–17] to radio-frequency current sources [18, 19]. These applications are enabled by a variety of mechanisms that allow control over the magnetic properties of the materials involved, such as the use of optical [20–26] or magnetic fields [26–29], or spin-currents [30–35]. Current-based control mechanisms are of particular interest as they allow direct integration with complementary metal-oxide-semiconductor (CMOS) technology [36, 37], demonstrated with the commercialization of a magnetic random-access memory utilizing spin-transfer torques [38].

The study of the dynamics involved in the manipulation of nanoscale magnetic textures demands experimental methods with sufficient spatiotemporal resolution. Based on transmission electron microscopy (TEM), Lorentz microscopy [39–41] is an established method for the static imaging of nanoscopic magnetic structures, capable of resolving magnetic features $< 1\,\mathrm{nm}$ [42]. While early attempts of time-resolved Lorentz microscopy do exist, these fell short in providing the spatial resolution achievable in static measurements [43, 44]. This changed with the recent advent of high-brightness sources for ultrafast transmission electron microscopy (UTEM) [45–47], which enabled a number of studies imaging the nanoscale response of magnetic samples excited with optical pulses [48–50]. However, its application to the field of current-induced magnetization dynamics has remained unexplored to date.

This cumulative thesis addressed this topic and demonstrates the capabilities of time-resolved Lorentz microscopy by imaging the current-driven gyration dynamics of a vortex confined in a magnetic nanostructure. In addition, I showcase the unique capabilities of TEM, which allows the collection of both time-resolved magnetic and structural information on a sample system in the same instrument. This provides insights into the interaction of magnetic textures with defects in their host films.

Outline

While chapters 4 and 5 are reprints of the original papers that comprise this cumulative thesis, chapters 2 and 3 contain a more comprehensive introduction into the method and sample system studies throughout these publications.

The publication in Chap. 4 presents the first implementation of UTEM for the study of current-driven magnetization dynamics. The examined sample is a vortex domain configuration in a square magnetic nanostructure. Driven by a combination of spin-transfer torques and an in-plane magnetic field, the gyrotropic motion of the vortex core is mapped using Lorentz microscopy.

The paper presented in Chap. 5 focuses on studying the interaction between the vortex core and defects, initially identified in the previous work. This investigation is made possible by the following three efforts: Firstly, the implementation of a novel photoemission source, which accelerates the data acquisition for probing the time-resolved vortex gyration dynamics by two orders of magnitude. Secondly, the identification of static pinning sites in the polycrystalline film employing a new technique developed for this publication. Lastly, the comparison of the data gathered via the previous two methods with structural information on the magnetic film recorded via bright-field imaging.

Chapter 2 comprises a detailed description of time-resolved Lorentz microscopy as a method to image magnetization dynamics with high spatiotemporal resolution. This includes a discussion of the contrast formation in Lorentz microscopy and a presentation of the basic principles allowing for a temporally resolved TEM, with a focus on ultrafast transmission electron microscopy.

Chapter 3 provides a focused introduction to the vortex domain configuration that occurs within magnetic nanostructures. It includes a description of a theoretical model that explains the current-driven gyration dynamics of the vortex core. Additionally, the chapter presents a review of previous studies that examined the impact of defects on the dynamics in vortex nanostructures.

Lastly, I summarize the achievements of the work presented in this thesis in Chap. 6 and provide an outlook of potential future studies, enabled by these accomplishments.

2

Time-resolved Lorentz microscopy

I begin this chapter with a brief introduction of TEM followed by a description of how Lorentz microscopy can be used to study magnetization dynamics with a high spatial-temporal resolution. For this purpose, I discuss the two topics Lorentz microscopy and UTEM independently, before finally presenting the current state of research on the combination of both techniques.

2.1 | Transmission electron microscopy

Transmission electron microscopy is a technique applied across many scientific fields, from biology to material sciences and magnetism. As a comprehensive discussion of the capabilities of TEM is beyond the scope of this thesis, I will only cover its basic aspects in this chapter. A comprehensive review is provided by each of the many excellent textbooks on this subject [51–53].

Set out to surpass the limitations in the resolution of light microcopy governed by the Abbe-limit, the first TEM was developed by Max Knoll and Ernst Ruska in 1931 [54, 55]. While modern aberration-corrected TEMs routinely achieve sub-ångström resolution, there is still an active pursuit to bring the spatial resolution closer to the electron wavelength, i.e., 2.7 pm at a typical electron acceleration voltage of 200 kV [56, 57].

Transmission electron microscopes share much of their layout with their counterparts in light microscopy (cf. Fig. 2.1). The first building block of a TEM is the gun. It contains an electron source and an accelerator, operating typically at voltages from tens to hundreds of kilovolts. Leaving the gun, the electrons enter the condenser, a set of magnetic lenses and apertures used to prepare the electron beam to illuminate the sample. Being able to choose from a large set of spot sizes and angles, the illumination

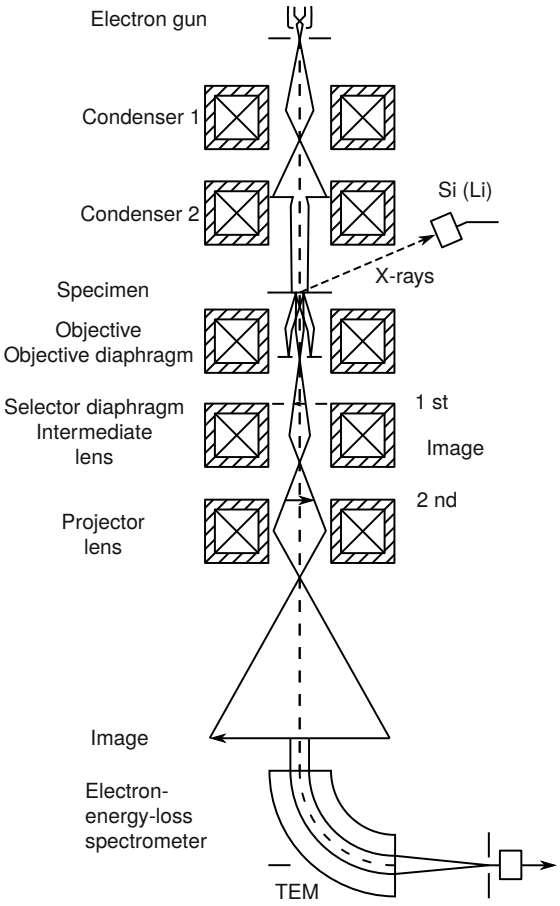

Figure 2.1: **Schematic ray diagram of a transmission electron microscope operated in an imaging mode.** Note that this sketch, with a single objective lens below the sample, is not representative of modern TEMs, often equipped with a twin-lens pole piece. However, it closely approximates the ray diagram encountered in Lorentz microscopy, where a secondary lens below the sample serves as the objective. Reproduced with permission from Springer Nature from Ref. [52]. © 2008, Springer-Verlag New York

can range from a several hundred-micron large near-parallel beam to a tightly focused sub-ångström spot with a large conversion angle.

Below the sample is a strong objective lens that generates an intermediate image of the sample. In the standard imaging mode, this intermediate image is brought to the final magnification—between 50X to over 1.00.000X—by another set of adjustable lenses. Alternatively, these lenses can be used to image the back-focal plane of the objective lens, enabling diffraction experiments within the same instrument. The final image of the sample or its diffraction pattern is then acquired with a TEM camera (more details about such cameras are presented in Chap. 2.3).

Besides conventional TEM, relying on a camera for image acquisition, most modern instruments can also operate as scanning transmission electron microscopes. In this mode, a tightly focused electron probe is scanned across the sample. In the simplest case, the image of the sample is then formed by measuring the transmitted current of the undiffracted beam with a single-pixel electron detector at each scan position. One advantage of this mode is that it allows for the parallel acquisition of additional signals, e.g., the locally emitted X-ray spectrum for a spatially resolved elemental analysis of the sample.

Due to the limited mean-free path of electrons in solids, TEM samples have to be sufficiently thin. While lighter elements still provide acceptable transmission at thicknesses $> 200\,\mathrm{nm}$, more demanding methods, such as high-resolution TEM, might even require samples as thin as some tens of nanometers to not disturb the desired contrast.

In high-resolution TEM, as in many other related techniques, this contrast is given rise to by a phase (rather than a change in intensity) acquired by the electron wave after passing the sample. Therefore, the question of how to achieve and optimize this phase contrast is often one of the crucial aspects of electron microscopy. In the following section, I will answer this question in the context of imaging magnetic samples.

2.2 | Lorentz microscopy

Lorentz microscopy encompasses various methods for the imaging of magnetic domains using TEM [58, 59]. It derives its name from the Lorentz force and includes methods such as Fresnel and Foucault imaging, as well as differential phase contrast [58, 59]. In addition, electron holography is also worth mentioning as a capable TEM-based technique for imaging magnetic structures[60]. In the following section, I will focus on the discussion of Fresnel imaging, which was used in the publications presented as part of this thesis.

Figure 2.2 illustrates a classical explanation for the contrast formation mechanism for Fresnel and Foucault imaging. A magnetic sample with thickness h is transmitted by a parallel electron beam, which is subsequently projected to an image plane by the objective lens. While the electrons pass the sample, they interact with its magnetic field via the Lorentz force and are deflected perpendicular to their initial direction of motion.

Generally, the Lorentz force between a samples magnetic field $\mathbf{B}$ and an electron is given by

$$\mathbf{F}_\mathrm{L} = -e\mathbf{v}_e \times \mathbf{B}\ , \tag{2.1}$$

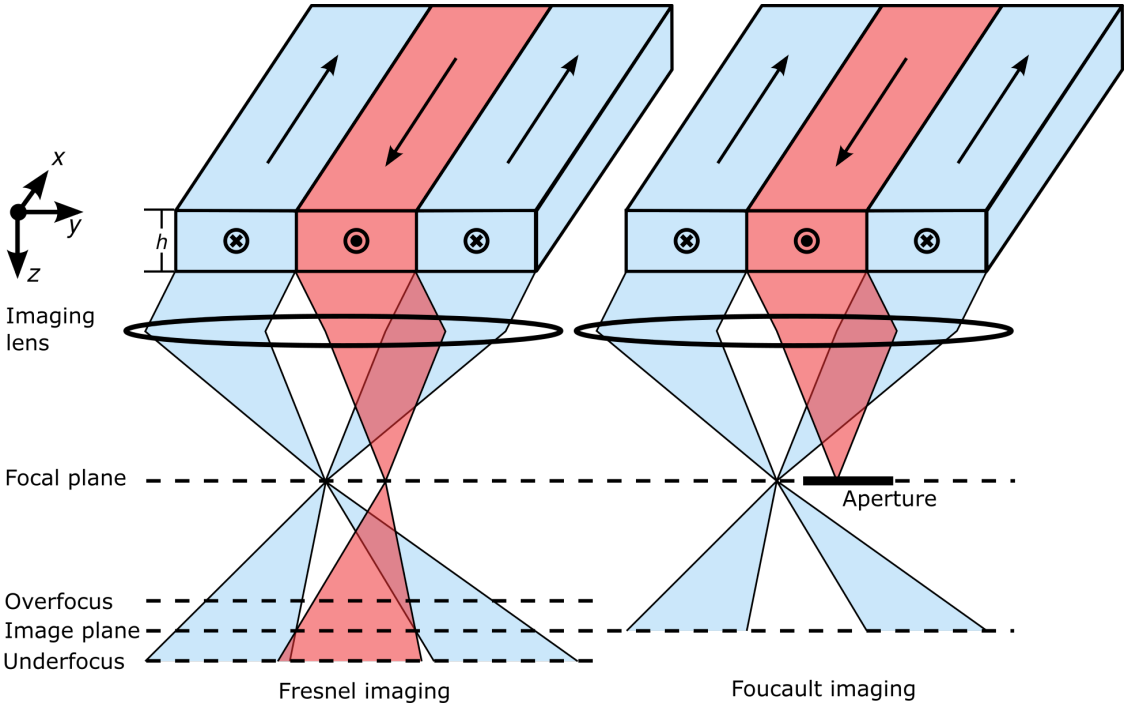

Figure 2.2: **Illustration of the image formation in Fresnel and Foucault imaging.**

where e is the electron charge, and $\mathbf{v}_e$ is the electron velocity. In our simplified model (Fig. 2.2) with the incoming electron velocity along the z-direction and the magnetization along the x-direction, only the y component of the Lorentz force remains nonzero

$$F_{\mathrm{L},y} = -ev_{e,z}B_x \ . \tag{2.2}$$

After passing the sample the electrons gained a transverse momentum of

$$p_y = \int F_{\mathrm{L},y}\,\mathrm{d}t = -eB_x\,h \ , \tag{2.3}$$

which translates to an angular deflection of

$$\theta = \frac{p_y}{p_z} = \frac{-eB_x\,h}{m_e v_{e,z}} \ , \tag{2.4}$$

where m_e is the relativistic mass of the electron. For a typical acceleration voltage of 200 keV this corresponds to a deflection of approximately 0.61 µrad T^{-1} nm^{-1}, or about 30 µrad for a 50 nm thick sample with a magnetic inductance of 1 T [41]. These angles are relatively small, compared to crystallographic Bragg deflection angles, which are on the order of several milliradians.

In the back focal plane of the objective lens—sensitive to the transverse momentum of the electrons, only—the electrons are separated according to the magnetization direction of the material they passed (see Fig. 2.2). Leaving the back focal plane, the different beams will eventually reach the image plane of the lens. Without further action, a detector placed in this plane will produce a micrograph of the sample containing no magnetic information.

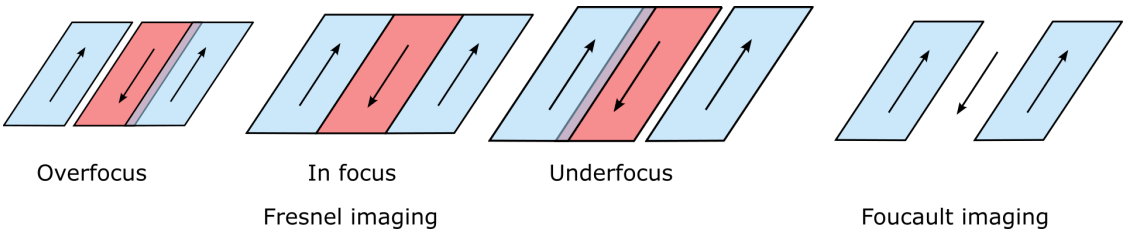

Figure 2.3: **Illustration of the resulting Fresnel and Foucault images produced by the schematic setups shown in Fig. 2.2.**

For Foucault imaging, one can insert a half-plane aperture into the back focal plane, which blocks electrons having passed through domains with one specific magnetization direction. While these domains will appear dark, antiparallel magnetized domains will be bright and domains with perpendicular magnetization grey. Therefore, Foucault imaging often involves acquiring two images where the apertures block half-planes that are perpendicular to each other.

To perform Fresnel imaging, the objective lens is slightly defocused, such that a plane below or above the image plane is recorded with the camera. Since electrons that have passed differently magnetized domains converge towards the image plane under different angles, regions of increased and decreased electron intensity will form where there is a change in the in-plane magnetization. Thus, a typical Fresnel image consists of dark and bright lines, indicating the position of domain walls in the sample.

In practice, Lorentz imaging is not performed with the main objective lens of the microscope but rather with a weaker long-focal-length lens that is placed relatively far (some centimeters) below the specimen. This is to avoid the magnetic field of the lens altering the state of the sample. If necessary, the main objective lens can be weakly excited to supply an out-of-plane bias field.

Imaging samples with an out-of-plane magnetization is also possible, especially using Fresnel imaging. While out-of-plane Néel walls directly produce an alternating dark and bright contrast along a single wall, Bloch walls can be imaged by tilting the sample. To provide a better understanding of the contrast formation in Fresnel imaging for all

types of domain walls, I will explain this process based on a quantum-mechanical wave formulation.

2.2.1 | Quantum-mechanical formulation of Fresnel imaging

Although the deflection-based explanation of Fresnel imaging gives an easy intuition of the image formation process, it does not suffice to explain effects caused by the coherent nature of the illuminating beam, e.g., fringes along domain walls. A more accurate quantum-mechanical description is based on contrast transfer theory, which also enables the simulation of Fresnel images based on micromagnetic models of magnetic samples [61]. A general description of contrast transfer theory can be found, e.g., in Refs. [51, 61]. The following section, however, is based on a summary of Ref. [41], which is tailored specifically to contrast transfer theory for magnetic imaging.

In this framework, we assume that the sample is illuminated with a plane wave. The electron wavefunction exiting the sample

$$\Psi\left(\mathbf{r}_{\perp}\right) = a\left(\mathbf{r}_{\perp}\right) e^{i\varphi_{\mathrm{AB}}\left(\mathbf{r}_{\perp}\right)} \tag{2.5}$$

can be written as a product of an amplitude $a\left(\mathbf{r}_{\perp}\right)$ and a phase term $\varphi_{\mathrm{AB}}\left(\mathbf{r}_{\perp}\right)$, both as a function of in-plane position $\mathbf{r}_{\perp}$. The phase shift

$$\varphi_{\mathrm{AB}}\left(\mathbf{r}_{\perp}\right) = \frac{\pi}{\lambda E_{\mathrm{t}}} \int_{L} V(\mathbf{r}_{\perp}, z)\mathrm{d}z - \frac{e}{\hbar} \int_{L} \mathbf{A}\left(\mathbf{r}_{\perp}, z\right) \mathrm{d}z \tag{2.6}$$

acquired by the electrons by passing the magnetic sample, is due to the Aharonov-Bohm effect [62]. Here, V and $\mathbf{A}$ are the electromagnetic potentials, E_t is the total energy of the electron beam, λ is the electron wavelength and $\hbar$ is the reduced Planck constant. The integral is along a straight line L, which runs parallel to the direction of the incident beam. The first term describes an electrostatic phase shift due to the inner potential in the sample material and decreases with an increasing acceleration voltage. The second term is the magnetic phase shift φ_{M} and is independent of the acceleration voltage.

The magnetic phase shift φ_{M} can either be calculated for a given vectorpotential $\mathbf{A}\left(\mathbf{r}_{\perp}, z\right)$ or for a periodic (or periodically expandable) magnetization $\mathbf{M}\left(\mathbf{r}_{\perp}, z\right)$ using a formula first published by Mansuripur [64]. Fig. 2.4 shows the connection between the magnetization and the phase for the example of a magnetic vortex in a microstructure (see Chap. 3.2), which consists of four domains curling counterclockwise around its center. The calculated magnetic phase φ_{M} consists of four linear slopes in the region corresponding to each domain. Note that the four phase gradients result in four deflection angles in the far-field, consistent with the classical explanation given in the previous section.

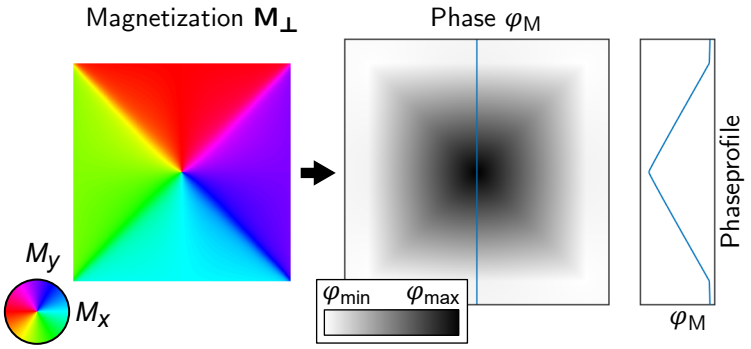

Figure 2.4: **Connection between the sample magnetization and the magnetic Aharonov-Bohm phase.** (Left) In-plane magnetization $\mathbf{M}_\perp$ of a magnetic vortex structure simulated using MuMax3 [63]. (Center) Magnetic Aharonov-Bohm phase φ_M calculated from the magnetic structure on the left. A section of the phase along the blue line is presented on the right. It shows a linear phase profile in either domain. Simulation details: $M_S = 500\,\mathrm{kA\,m^{-1}}$, $A_{ex} = 1.1 \times 10^{-11}\,\mathrm{J\,m^{-1}}$, 2 µm wide, 30 nm thick.

After the electron wave propagates through the sample, the exit wave $\Psi(\mathbf{r}_\perp)$ passes the objective lens of the microscope (see Fig. 2.5). In the context of contrast transfer theory, the effects of the objective lens, e.g., due to defocus or other image aberrations, are dealt with by multiplying the wavefunction with a transfer function $T(\mathbf{q}_\perp)$ in momentum space

$$\Psi(\mathbf{q}_\perp) = \mathbf{F}[\Psi(\mathbf{r}_\perp)]\, T(\mathbf{q}_\perp)\ , \tag{2.7}$$

where $\mathbf{F}[\Psi(\mathbf{r}_\perp)]$ is the fourier transform of $\Psi(\mathbf{r}_\perp)$.

A minimal transfer function to illustrate Lorentz imaging consists of three terms

$$T(\mathbf{q}_\perp) = A(\mathbf{q}_\perp)\, e^{-i\zeta(\mathbf{q}_\perp)} e^{-g(\mathbf{q}_\perp)}\ . \tag{2.8}$$

The aperture function $A(\mathbf{q}_\perp)$ is usually equal to 1. Setting it to zero in a specific half-plane allows us to simulate Foucault images. For Fresnel imaging, the second term is most important, as it describes the transfer from phase information to the intensity of the final image. Ignoring other types of aberration, its phase

$$\zeta(\mathbf{q}_\perp) = \pi\lambda\Delta f\, |\mathbf{q}_\perp|^2 \tag{2.9}$$

is a function of the objective lens defocus Δf. The last term is a damping envelope, which accounts for the limited size of the electron source. As a first-order approximation, its exponent is given by

$$g(\mathbf{q}_\perp) \approx \frac{(\pi\theta_c\Delta f)^2}{\ln 2}\, |\mathbf{q}_\perp|^2\ , \tag{2.10}$$

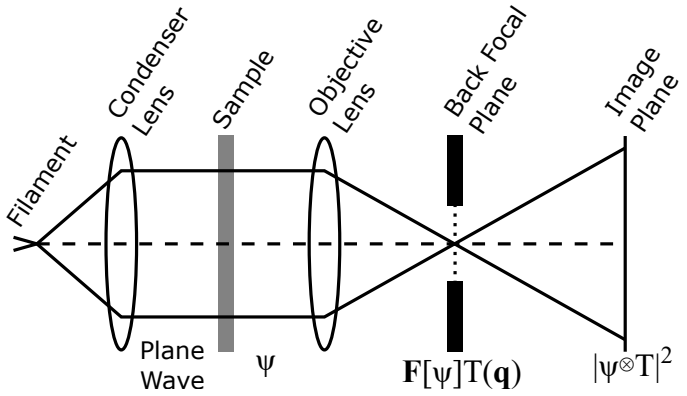

Figure 2.5: **Schematic representation of contrast transfer theory.** The sample is illuminated with a plane wave and the exit waveform Ψ is projected to the image plane via the objective lens. The effects of the lens on the final image are factored in, by multiplying a transfer function T to the wave in the back-focal plane $\mathbf{F}[\Psi]$. Reprinted from Ref. [41], © 2001 with permission from Elsevier.

where θ_c is a beam divergence half-angle and a measure of beam coherence. The final image intensity can then be obtained via an inverse Fourier transform

$$I = \left| \mathbf{F}^{-1} \left[\mathbf{F} \left[\Psi \left(\mathbf{r}_\perp \right) \right] T \left(\mathbf{q}_\perp \right) \right] \right|^2 . \tag{2.11}$$

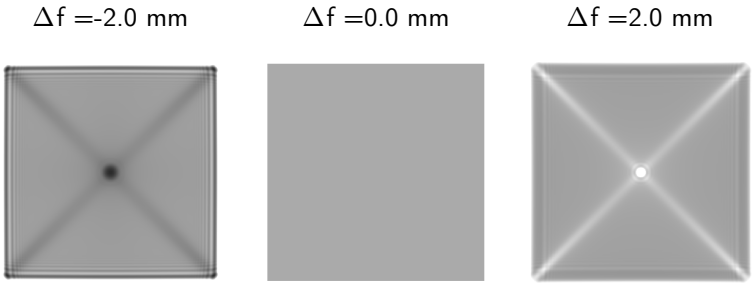

Figure 2.6: **Simulated Fresnel images of the vortex structure in Fig. 2.4.** While the infocus image at $\Delta f = 0\,\mathrm{mm}$ shows no magnetic contrast, the domain wall are clearly visible as bright or dark lines in the defocused images. In this example, the sign of the contrast is determined by a combination of the defocus and the vortex curl c (see Chap. 3.2).

Figure 2.6 shows a set of Fresnel images calculated based on the phase φ_M of the magnetic vortex in Fig. 2.4. We see that the infocus image $\Delta f = 0\,\mathrm{mm}$ does not contain magnetic contrast. In the defocused images, however, the domain walls appear as

bright and dark lines and the strongest contrast is in the center, where all domain walls intersect.

2.3 | Ultrafast transmission electron microscopy

In this section, I introduce ultrafast transmission electron microscopy (UTEM). I begin with a discussion on how to generally realize time-resolved TEM, followed by a brief review of the development of the various techniques relying on a pulsed electron beam. Finally, I will introduce the Göttingen Ultrafast Transmission Electron Microscope, which was used to perform the experiments presented in the two manuscripts contained in this thesis (see Chaps. 4 and 5).

Time-resolved imaging in the TEM can be achieved via detector- or beam-based approaches. Detector-based approaches rely on fast TEM cameras, with a time resolution limited by the fastest available read-out time. Previous generation TEM cameras consisted of an electron scintillator fiber-coupled to a charge-coupled device (CCD) camera [51]. In the last decade, however, camera manufacturing has transitioned to standard complementary metal-oxide semiconductor (CMOS) technology, which allows for much faster readout speeds [65]. These CMOS cameras are equipped with a fiber-coupled scintillator or come in the form of direct electron detectors, some providing readout speeds of over ten thousand frames per second [66, 67]. Furthermore, there exist specialized event-based cameras like Timepix3, which allow timing the arrival of an electron with a resolution $> 2\,\mathrm{ns}$ (at the caveat of a pixel dead-time of several hundreds of nanoseconds) [68, 69]. Similarly, the use of a delay line detector as a replacement for a camera has been reported, with a time resolution as low 120 ps [70, 71].

Beam-based approaches rely on the pulsing of the electron beam. This can either be achieved by modulating a continuous electron beam, e.g., using fast beam blankers or a sophisticated arrangement of microwave cavities, or by directly generating a pulsed electron beam using a photocathode and a pulsed laser. Recent reviews of both topics as well as some historic remarks can be found in Refs. [72–74]. The beam-based approach has been pioneered by the group of Oleg Bostanjoglo, who, among other instruments, built both a TEM equipped with a fast beam pulser [43, 75] as well as laser-driven electron source [76].

Depending on the number of electrons contained in a single pulse, one differentiates between two types of time-resolved electron microscopy: dynamic transmission electron microscopy (DTEM) and ultrafast transmission electron microscopy (UTEM). In single-frame DTEM, a dynamical process in a sample is initiated with a single optical

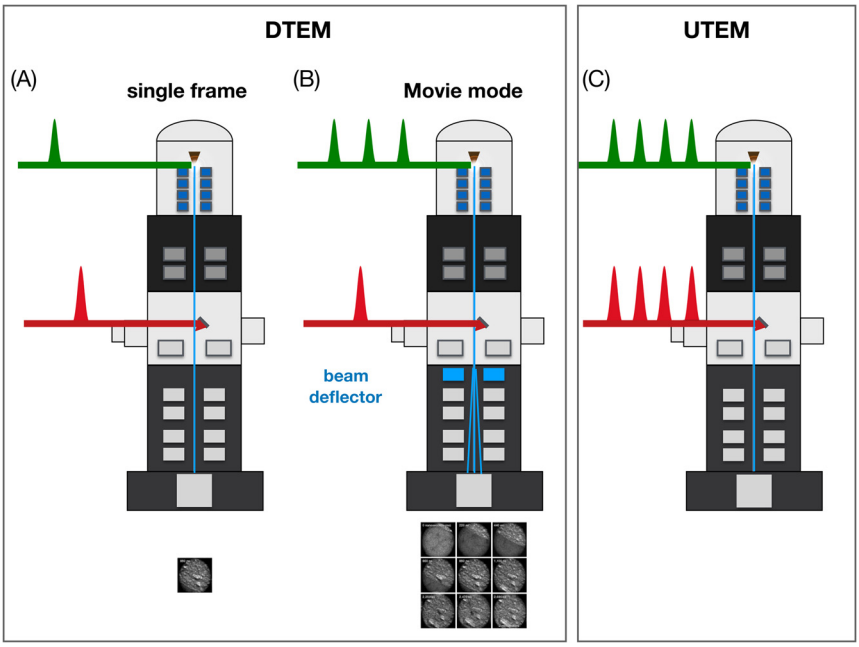

Figure 2.7: **Schematic representation of DTEM and UTEM.** (A) In single-frame DTEM a single pump and probe pulse are used to excite and image a dynamic process at one point in time. (B) In movie-mode DTEM a single pump pulse and several probe pulses are used to compile a movie of a dynamic process. A beam deflector below the sample separates frames stemming from the multiple probe pulses. (C) UTEM uses a stroboscopic approach with multiple pump and probe pulses to image reversible processes. Reprinted from Ref. [73], © 2018 with permission from Elsevier.

pump pulse and imaged with a single electron probe-pulse (Fig. 2.7A). To form an image on the camera, the electron pulse must contain a sufficient number of electrons (typically $> 10^8$). The electron probe-pulses can be as short as 10 ns, limited by Coulomb interaction between the electrons in the pulse. These space-charge effects would deteriorate other beam properties, such as the spatial resolution if the same number of electrons were to be contained in a significantly shorter pulse [77]. To observe the temporal evolution of a reversible process, several frames can be acquired with a slight variation in the time delay between the arrival of the pump and the probe pulse at the sample. For the study of irreversible dynamics, on the other hand, movie-mode DTEM has to be employed (Fig. 2.7B). In this mode, the pump pulse is again a single laser pulse, the probe, however, consists of a train of pulses, each imaging the sample at different time delays. A beam deflector in the microscope positioned below the sample then shifts the individual frames produced by each electron pulse to a separate region at the detector plane.

Building on the early work of Bostanjoglo [76, 78] major progress in DTEM has been achieved at the Lawrence Livermore National Laboratory. This includes the use of an additional condenser lens to allow a higher electron current to be transmitted from the source to the sample [79], as well as an improvement of the beam deflector below the sample, capable of acquiring up to 16 frames [80]. This enabled, e.g., studying the reaction dynamics in Ti–B-based reactive nanolaminates [80].

In UTEM the electron charge in a single pulse is usually between one and a few hundred electrons. This allows for much shorter pulses on the order of femtoseconds while still maintaining a high spatial resolution by avoiding space-charge effects. To acquire a single frame an experiment is carried out in a stroboscopic fashion, i.e., a train of pump pulses repeatedly excites the same dynamical process in the sample, which is simultaneously imaged by a train of probe pulses. The arrival time between a single pump and probe pulse is kept constant and the sample is required to return to its equilibrium state between two consecutive pulses. The acquisition time of a single frame can then vary between several seconds to minutes, depending on the repetition rate of the laser system, the average number of electrons in a pulse, and the desired signal-to-noise ratio. To obtain a movie of the temporal changes in the sample, multiple frames with different delays between the pump and the probe pulse are recorded.

Stroboscopic imaging using a beam pulser was initially accomplished by Bostanjoglo [43, 81]. UTEM—with access to higher temporal and spatial resolution—however, was first demonstrated in the group of Ahmed Zewail [82]. The instruments developed in his group used flat LaB_6 photocathodes with front facets measuring 15 µm and larger [83]. The high spatiotemporal resolution allowed, for example, the study of structural dynamics, both using diffraction and real space analysis [83].

Building upon the work of Ahmed Zewail, a major leap forward in UTEM came with the development of high-brightness sources. Similar to the revolution that Schottky and cold-field emitters brought in the field of conventional TEM, high-brightness emitters in UTEM enable new experimental opportunities, such as high-resolution, Lorentz and scanning transmission electron microscopy or electron holography [51, 73].

The first TEM to be equipped with a high-brightness pulsed source was the Göttingen UTEM [45, 46], featuring a laser-driven Schottky field emitter (details in Chap. 2.3.1). Its development was based on the research around laser-driven nanotip catodes [84, 85]. The first laser-driven cold field UTEM gun was developed in Toulouse [47, 86]. Similar instruments are now set up in various places, e.g., at the Institute of Physics of the Chinese Academy of Sciences [87] and the École Polytechnique Fédérale de Lausanne [88].

2.3.1 | Göttingen Ultrafast Transmission Electron Microscope

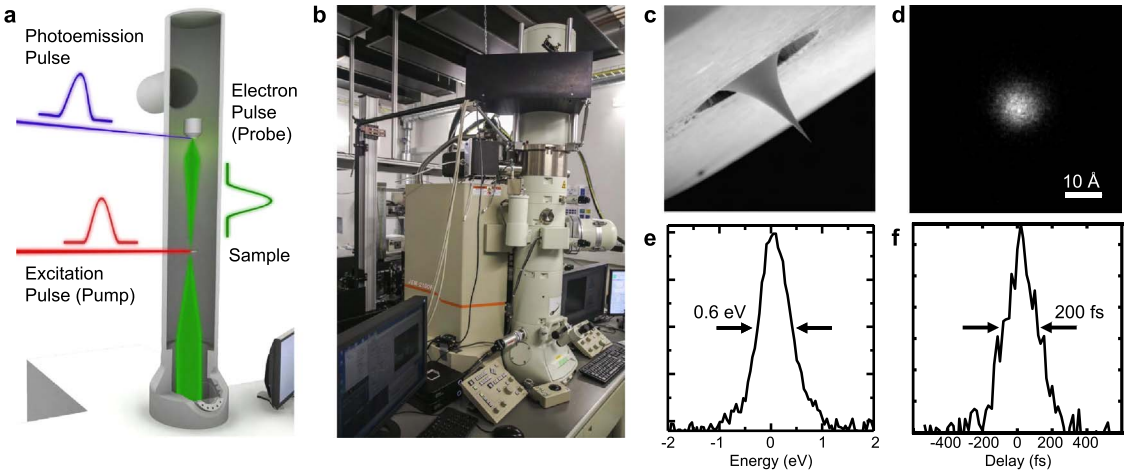

Figure 2.8: **The Göttingen Ultrafast Transmission Electron Microscope.** (a) A schematic representation of a laser-pump electron-probe scheme, which can be conducted at the instrument. (b) A photograph of the instrument. Visible in the front is the modified TEM with an optical cage around its gun. From there, an enclosed optical path leads to the table behind, where the laser system is located. (c) Scanning electron micrograph of the ZrO/W(100) nanoemitter, protruding out of the suppressor. This emitter is capable of delivering a minimum spot size of 0.89 nm (d), a spectral width of 0.6 eV and a pulse width as short as 200 fs. Reprinted from Ref. [46].

The Göttingen UTEM is a modified JEOL JEM-2100F TEM. It is the first TEM that was equipped with a laser-driven Schottky field emitter, featuring a peak brightness similar to conventional Schottky field emission guns [46]. Specifically, the emitter is a monocrystalline tungsten (W) tip with a (100) front facet and a zirconium oxide (ZrO) reservoir at its shaft [89, 90]. When the filament is heated to its conventional operating condition of about 1800 K the ZrO covers the tip and reduces its work function. With the application of an extraction field on the order of 1 V nm^{-1}, a continuous electron beam can be extracted from the tip.

To obtain a pulsed beam, the filament temperature is reduced to below 1500 K until the continuous electron emission ceases. Under these conditions, the emitter can be laser-driven via single-photon photoemission with a wavelength of up to 530 nm. The shortest electron pulses measured at the instrument were at around 200 fs, generated with the frequency-doubled output of a regenerative Ti:Sapphire amplifier (Coherent RegA) at 400 nm. Due to the linear photoemission employed, one can simply increase the electron pulse length by increasing the pulse length of the driving laser. This allows for a higher pulse charge and average emission current in the space-charge limited

regime for experiments that do not require ultimate temporal resolution [91].

In the experiments presented as part of this thesis, we use two lasers to drive the emission process. In the manuscript in Chap. 4 we employ the frequency-doubled output of a Coherent RegA at a repetition rate of 500 kHz and stretch its pulses to a length of about 2.2 ps using a glass bar. For the second experiment (chap. 5), to maximize the average electron current, we used a custom Onefive Katana 05-HP that operates at a pulse length of around 35 ps at 532 nm with a variable repetition rate between 20 and 80 MHz. Using the custom laser allowed us to reduce the image acquisition time by multiple orders of magnitude.

Samples in the Göttingen UTEM can be excited optically and electrically. Two optical ports allow for a laser excitation either under an angle of incidence of around 55° relative or near parallel to the electron beam. As part of this thesis, a custom-made *in-situ* sample holder was designed, which allows for electrical stimuli of the sample. It consists of a RF SMA vacuum-feedthrough connected to in-vacuum coaxial cables, which terminate in a coplanar waveguide [92].

Enabled by the vast experimental capabilities of TEM and its excellent spatiotemporal resolution, the Göttingen UTEM has proven to be an invaluable tool in various scientific fields. These include the study of structural dynamics [93, 94] and the imaging of phase transitions [95], as well as in the fields of nano-optics [96–101]. An overview of the capabilities of the instrument is presented in Fig. 2.3.1. The achievements of UTEM in the field of nano-magnetism together with a practical example of work that has been done in Göttingen is the topic of the next chapter.

2.4 | Time-resolved Lorentz microscopy

UTEM is a promising technique for the study of magnetization dynamics on the nanoscale [73], as it allows access to the length- and timescales of many interesting magnetic phenomena (see Fig. 2.10). Yet, the number of studies leveraging this potential is still fairly limited. A short review of the recent developments is in Ref. [102]. In the following, I will summarize the most important developments preceding the publications which are part of this thesis.

One of the first papers to study magnetization dynamics using a pulsed electron beam was published by the group of Oleg Bostanjoglo [43]. They utilized an electric beam blanker to generate 50 ns long pulses and stroboscopically acquired Lorentz micrographs of magnetic domains excited via an ultrasonic transducer with 10–50 kHz sine waves [103]. Later the group improved the time resolution of their setup to around 1 ns,

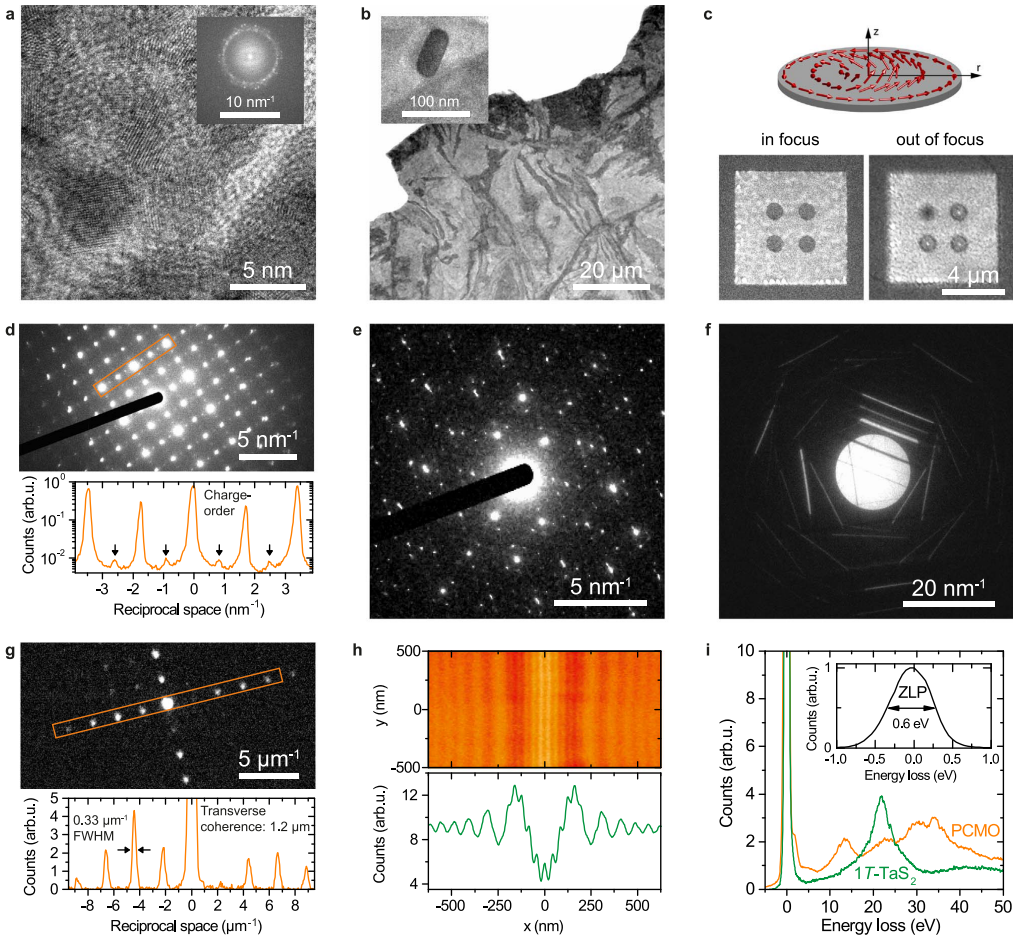

Figure 2.9: **Compilation of results recorded at the Göttingen UTEM.** (a) High-resolution TEM micrograph of gold/palladium nanoparticles on an amorphous carbon film acquire using thermal emission. Results in (b-i) were produced with photoemitted electrons at an acceleration voltage of 120 keV. (b) Bright-field image of a 50 nm thick 1T-TaS_2 sample with drop-cast gold particles (see inset). A majority of the contrast is due to a bending of the film. (c) Bottom: Lorentz micrographs of permalloy nanostructures prepared via focused-ion beam milling. Top: Illustration of the magnetization within the nanostructures. (d) Diffraction pattern of an ion-polished $Pr_{0.7}Ca_{0.3}MnO_3$ (PCMO) sample in a charge-ordered phase. (e) Diffraction pattern of 1T-TaS_2 in a nearly-commensurate charge density wave phase. (f) Convergent beam electron diffraction pattern of a 100 nm thick graphite single crystal. (g) High dispersion diffraction pattern of a square replica grating with a spacing of 432 nm. From the pattern, a transverse coherence length of 1.2 µm can be deduced. (h) Demonstration of the electron beam coherence via electron holography. The hologram was generated with a Möllenstedt biprism at a filament voltage of 9 V. (i) Presentation of two-electron energy loss spectra of 1T-TaS_2 and PCMO, together with a display of the zero-loss peak width in the inset. Reprinted from Ref. [46].

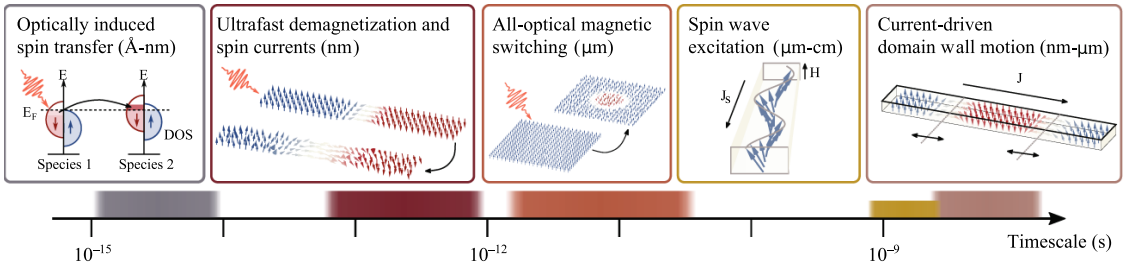

Figure 2.10: **Overview of a variety of magnetic phenomena with length- and timescales accessible to UTEM.** Reprinted from Ref. [102].

which allowed them to study the displacement of domain walls due to an alternating magnetic field with frequencies of up to 30 MHz [81].

Lorentz imaging with a pulsed beam from a photocathode has been demonstrated by Zewail and coworkers [83, 104]. They utilized the pulses of a nanosecond laser, both to excite and stroboscopically image the response in the thin ferromagnetic samples. Picosecond temporal resolution for Fresnel imaging was shown using a commercial TEM featuring a laser-driven electron source (FEI Tecnai Femto UEM) in 2017 in the group of David J. Flannigan [44].

A major enhancement in the spatiotemporal resolution of time-resolved Lorentz TEM was demonstrated by da Silva and coworkers at the Göttingen UTEM [48]. In this work, they imaged the ultrafast demagnetization of a single round permalloy nanostructure (1 µm diameter) excited with a femtosecond optical pulse. Prior studies utilizing flat photocathodes relied on defocus values on the order of several tens of millimeters to maximize image contrast [44, 104]. The high brightness of the source at the Göttingen UTEM allowed the use of a relatively small defocus of only 4.5 mm, which enabled a spatial resolution of 100 nm and a temporal resolution of up to 700 fs. Some of the results of this work are shown in Fig. 2.11. The micrographs in Fig. 2.11a show a fast loss in magnetic contrast after the optical excitation attributed to a decrease in the in-plane magnetization of the nanostructure.

A similar spatiotemporal resolution has lately also been achieved using a LaB_6 emitter with a 15 µm-diameter front facet [49]. In their work Zhang and coworkers, among other achievements, demonstrated that they can resolve a spin spiral with a periodicity of 70 nm in FeGe lamella. Similarly, the utilization of a guard-ring LaB_6 cathode was demonstrated to improve time-resolved imaging capabilities over traditional truncated tip LaB_6 with larger front facets [105]. This type of emitter was used by Cao and coworkers to study the magnetic precession of a permalloy film excited with a transient optical grating [50].

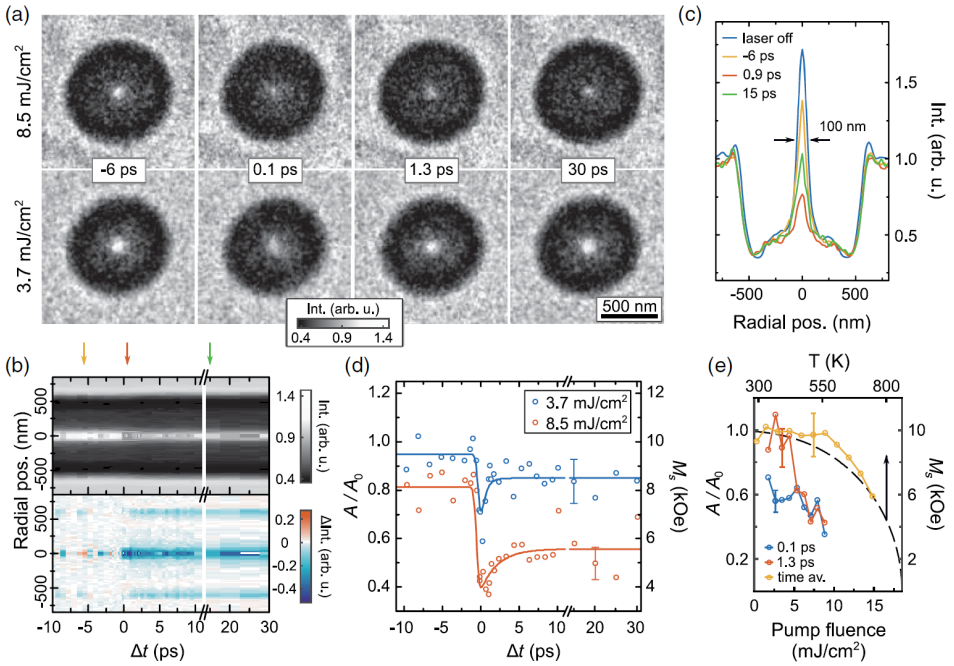

Figure 2.11: **Time-resolved Fresnel imaging of laser-driven demagnetization of** 1 µm**-wide and** 20 nm**-thick permalloy nanodisk.** (a) Fresnel micrographs at various delays, showing a loss of contrast at the vortex core after the optical excitation. (b) Azimuthally averaged profile as a function of delay. (c) Selected profiles marked with colored arrows in (b) showing the loss and recovery of contrast at the core position. (d) Temporal evolution of the core intensity. (e) Loss of core intensity as a function of the laser pump fluence measured at various delay times. Reprinted from Ref. [48] licensed under CC BY 4.0.

Other recent developments in the field of time-resolved Lorentz microscopy include the use of a delay line detector to image the precession of a vortex core with a continuous electron beam [70, 71]. Furthermore, the first Lorentz images acquired with a beam pulser based on two radiofrequency-driven traveling wave striplines have recently been published [106–109].

3

Current-driven magnetic vortex gyration

3.1 | Magnetic vortices in nanostructures

A magnetic vortex is a domain configuration often found in thin magnetic nanostructures. In a vortex configuration, the magnetization of the film is primarily in-plane and curls around a central out-of-plane magnetized core. Thus, the vortex has two degrees of freedom, a curl c and the polarity p, which indicate the sense of in-plane and the direction of out-of-plane magnetization, as depicted in Fig. 3.1.

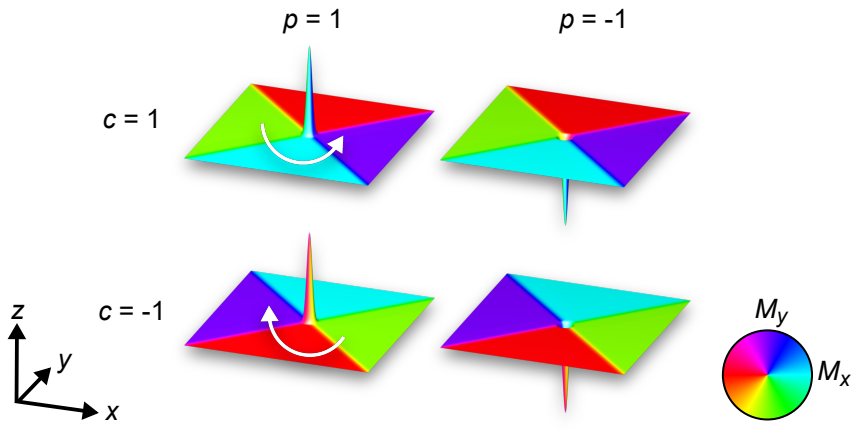

Figure 3.1: **Illustration of the four possible vortex ground states.** The direction of the in-plane magnetization is indicated by the color wheel on the right, while the sign and magnitude of the out-of-plane magnetization are plotted along the z-axis.

Much of the research on magnetic vortices was sparked by the seminal work of Cowburn et al., who measured the hysteresis curves of magnetic-nanostructure arrays using

magneto-optic Kerr effect (MOKE) microscopy [2]. Although they found small and/or thin nanostructures to form single domains (along the lines of Browns "Fundamental Theorem" [110]), they discovered a non-uniform domain state in larger nanostructures, which they interpreted as vortex states. Figure 3.2 illustrates this transition from a single-domain to a vortex ground state for round nanostructures. The depicted dimensions are specifically for a nanoisland made from permalloy, a soft-magnetic alloy made of around 80% nickel (Ni) and 20% iron (Fe).

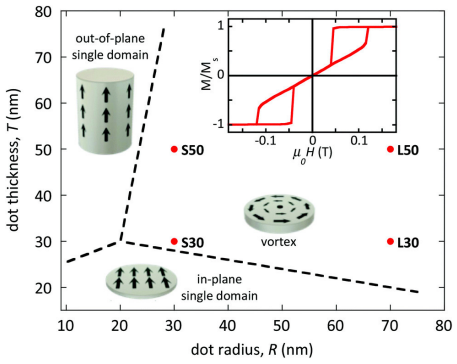

Figure 3.2: **Diagram indicating the magnetic ground state of round permalloy nanostructures as a function of their radius and thickness.** Based on the data of Refs. [111–115]. The inset shows a typical hysteresis curve of vortex nanostructure. Reproduced from Ref. [116] with permission from the Royal Society of Chemistry. © 2017 The Royal Society of Chemistry

The work of Cowburn et al. was quickly followed up by various studies, which directly imaged the vortex configuration in similar nanostructures [117–120]. Lorentz microscopy, for example, was used to visualize the curl of the in-plane magnetization, as shown in Fig. 3.3A [117]. With the overfocused imaging conditions employed in this example, the Lorentz force deflects the electrons towards the center, if the magnetization rotates counterclockwise ($c = 1$). This results in a bright spot at the center of the dot. If the magnetization rotates clockwise, the electrons are reflected away from the center, resulting in a dark spot. The polarization of the vortex core was initially probed using magnetic force microscopy (cf. Fig. 3.3B) [118]. Spin-polarized scanning tunneling microscopy later revealed the size of the core to be on the order of a few tens of nanometers [120].

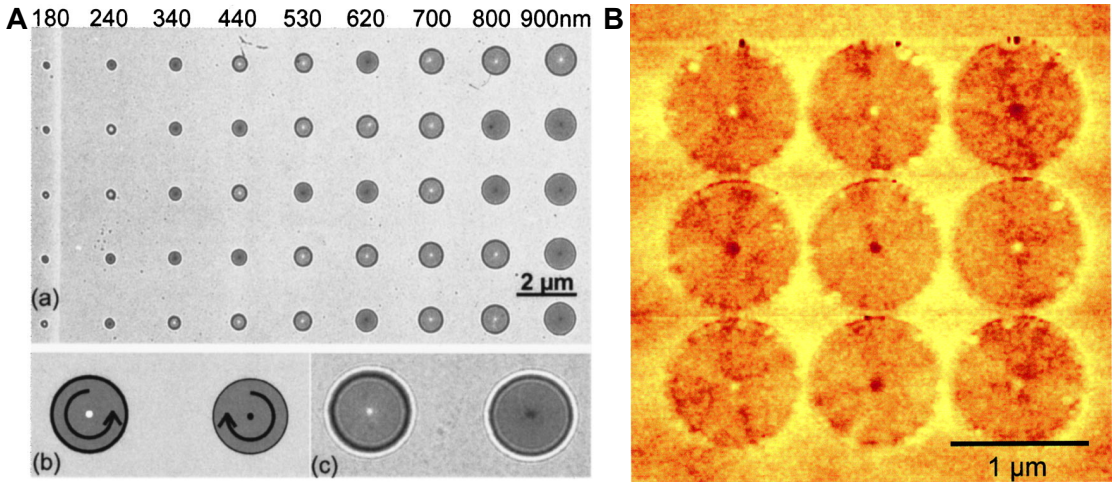

Figure 3.3: **Lorentz microscopy and magnetic force microscopy images of vortex nanostructures.** (A) Lorentz micrographs of permalloy nanostructures of various sizes (a,c). (b) Illustration detailing the image contrast in overfocus conditions. A counter-clockwise curl results in a bright central spot. Reprinted from Ref. [117], with the permission of AIP Publishing. © 2000 American Institute of Physics. (b) Magnetic force microscopy image, sensitive to the out-of-plane component of the magnetization of an array of permalloy nanostructures. The bright and dark spots in the center indicate the polarity of the vortex core. From Ref. [118]. Reprinted with permission from AAAS. © 2000 The American Association for the Advancement of Science.

3.2 | Current-driven vortex gyration

As a well-defined ground state in magnetic nanostructures, the vortex serves as an ideal testbed for studying magnetization dynamics. These dynamics include forcing the vortex core to follow an elliptical trajectory [28, 29, 121–123], or the controlled change of the vortex core polarity [124–129].

Figure 3.4 gives an overview of the most common methods used to excite dynamical processes in a vortex structure. The depicted methods include the use of in-plane and out-of-plane currents and magnetic fields. However, other means of excitation are also possible, e.g., the use of optical pulses [23, 24, 48]. In the publications that are part of this thesis, the configuration depicted in Fig. 3.4e is used to drive the gyrotropic mode of the vortex core with an alternating in-plane current. This current interacts with the vortex domains via an in-plane magnetic field and, by becoming partially spin-polarized, via spin-transfer torques.

In the following, I introduce a model that describes the interaction between an in-plane magnetic field and the vortex domains. This model is part of the theoretical expla-

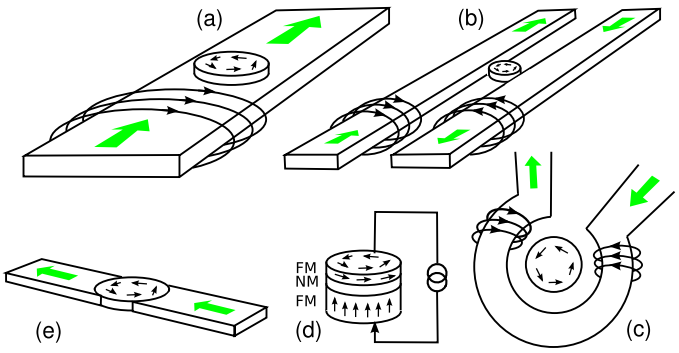

Figure 3.4: **Illustration detailing various configurations to excite dynamics in a vortex structure.** The means of excitation are via (a) in-plane fields, (b,c) out-of-plane fields, (d) spin-polarized out-of-plane currents and (e) in-plane currents. Reprinted with permission from JPS from Ref. [130]. © 2008 The Physical Society of Japan

nation for the current-driven vortex gyration presented in Chap. 3.2.2. I treat this model separately since it is also used for the calculation of the pinning potential based on the TRaPS data (see Chap. 5.3.2). Lastly, I provide an overview of the experimental studies dedicated to the imaging of the current-driven vortex gyration.

3.2.1 | Displacement by static field

The simplest type of excitation of a vortex nanostructure is the application of a constant in-plane magnetic field (H_x, H_y). For small displacements (X, Y) of the vortex core from its zero-field position, experimental studies found the displacement to be linearly dependent on the strength of the field [131, 132]. Thus, the energy of the vortex can be approximated using a quadratic potential

$$E_{\text{quad}} = \frac{1}{2}k(X^2 + Y^2) + ck\chi\left(-H_x Y + H_y X\right) \ . \tag{3.1}$$

Here, k is the stiffness of the restoring potential, χ is the displacement susceptibility and c is the curl of the vortex. Both values, k and χ, depend on the properties of the magnetic material as well as the geometry of the nanostructure. They can be calculated either based on a model, e.g., the rigid-vortex model [131, 133, 134], or via micromagnetic simulations, for example, using OOMMF or MuMax3 [63, 135].

The minimum of the quadratic potential in equation 3.1 represents the equilibrium position of the vortex core

$$\begin{pmatrix} X \\ Y \end{pmatrix} = c\chi \begin{pmatrix} -H_y \\ H_x \end{pmatrix} \tag{3.2}$$

and linearly depends on the applied field (H_x, H_y). Note that the displacement of the core is perpendicular to the field direction. Based on the potential in Eq. 3.1, we can also calculate the force

$$\mathbf{F} = -\nabla E_{\text{quad}} = -k \begin{pmatrix} X + c\chi H_y \\ Y - c\chi H_x \end{pmatrix} \tag{3.3}$$

that acts on the vortex core due the quadratic potential and the external magnetic field.

To describe the behavior of the vortex core for larger displacements, higher-order models exist, such as the two-vortex model [114, 121] and the deformable vortex pinning model [136].

3.2.2 | Theoretical model

Passing an alternating in-plane current through a vortex nanostructure allows driving the vortex core on an elliptical trajectory around the center of the nanostructure. To understand the origin of this behavior, Krüger et al. and coworkers developed a theoretical model, which I outline in the following [137, 138].

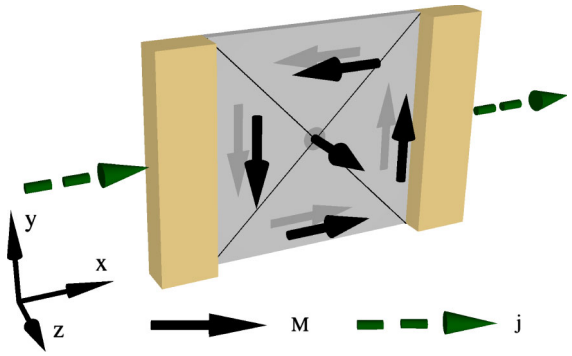

Figure 3.5: **Model of the sample system.** The magnetic nanostructure is depicted in gray, with black arrows indicating the magnetization direction of the four domains and the polarization of the vortex core. Contacts (beige) on either side of the nanostructure allow passing an in-plane current (green) through the magnetic film. Reprinted figure with permission from Ref. [137]. © 2010 by the American Physical Society

The model is based on the Landau-Lifshitz-Gilbert [139, 140] equation:

$$\frac{\mathrm{d}\mathbf{M}}{\mathrm{d}t} = -\gamma \mathbf{M} \times \mathbf{H}_{\text{eff}} + \frac{\alpha}{M_S} \mathbf{M} \times \frac{\mathrm{d}\mathbf{M}}{\mathrm{d}t} \,. \tag{3.4}$$

This equation describes the temporal evolution of the local magnetization $\mathbf{M}$ under the effective local field $\mathbf{H}_{\text{eff}}$, which combines external, demagnetizing, and exchange fields. The first term describes the precession of the magnetic moment around this effective

field, where γ is the gyromagnetic ratio. The second term specifies the damping of the precession with the material-specific Gilbert damping parameter α.

To take into account the effects of spin currents on the magnetic moments in the sample, Krüger et al. and coworkers use an extended Landau-Lifshitz-Gilbert equation by Zhang and Li [141]:

$$\begin{aligned}\frac{\mathrm{d}\mathbf{M}}{\mathrm{d}t} =& -\gamma\mathbf{M}\times\mathbf{H}_{\mathrm{eff}} + \frac{\alpha}{M_{\mathrm{S}}}\mathbf{M}\times\frac{\mathrm{d}\mathbf{M}}{\mathrm{d}t} \\ &- \frac{b_j}{M_{\mathrm{S}}^2}\mathbf{M}\times[\mathbf{M}\times(\mathbf{j}\cdot\nabla)\mathbf{M}] - \xi\frac{b_j}{M_{\mathrm{S}}}\mathbf{M}\times(\mathbf{j}\cdot\nabla)\mathbf{M}\,.\end{aligned} \tag{3.5}$$

Here, $b_j = P\mu_B/\left(eM_{\mathrm{S}}\left(1+\xi^2\right)\right)$ is a coupling constant between the current $\mathbf{j}$ and the magnetization, with P being the fraction of spin polarization in the current and μ_B the Bohr magneton. The additional terms by Zhang and Li describe the effects of the adiabatic and nonadiabatic spin-transfer torques, where ξ describes the degree of nonadiabaticity. These torques originate in the response of the spins of the conduction electrons to the spatial variations of the magnetization at domain walls and have first been proposed in the context of current-driven domain wall motion [141, 142].

Assuming the vortex domains retain their shape during excitation, Krüger et al. formulated a model, which reduces equation 3.5 to effective forces acting on the vortex core. This approach follows the ansatz of Thiele [143, 144], who studied the steady-state motion of domain walls based on the Landau-Lifshitz-Gilbert equation, and Thiaville et al., who extended Thiele's ansatz with the effects of spin-transfer torques [145].

For a confined vortex excited with a current, this force equation reads

$$\mathbf{F} + G_0\mathbf{e}_z\times\mathbf{v}_{\mathrm{c}} + D_\Gamma\alpha\mathbf{v}_{\mathrm{c}} + G_0\mathbf{e}_z\times b_j\mathbf{j} + D_0\xi b_j\mathbf{j} = 0\,. \tag{3.6}$$

The static forces $\mathbf{F}$ are due to an external magnetic field and a confining quadratic potential as discussed in the previous section. The second term is the gyrocoupling force perpendicular to the vortex velocity $\mathbf{v}_{\mathrm{c}}$, where G_0 is the amplitude of the so-called gyrovector. The viscous drag in the third term results from the Gilbert damping, where D_Γ is a phenomenological damping parameter, which considers a reduction in the damping due to the deformation of the vortex domains. The last two terms originate from the adiabatic and nonadiabatic spin-transfer torque, respectively. While the adiabatic spin-transfer torque acts to displace the vortex perpendicular to the current direction, the nonadiabatic torque results in a force along the current direction.

Krüger et al. also provide a solution of Eq. (3.6) for an alternating current $\mathbf{j}(t) = j_0 e^{i\Omega t}\mathbf{e}_x$ and a magnetic field $\mathbf{H}(t) = H_0 e^{i\Omega t}\mathbf{e}_y$. The direction of the magnetic field accompanying the electrical current has been identified experimentally and is assumed to

be caused by an inhomogeneous current distribution along the contacts of the nanostructure [137, 146]. The solution is given as

$$\begin{aligned}\begin{pmatrix} X \\ Y \end{pmatrix} =& C_1 \begin{pmatrix} i \\ p \end{pmatrix} e^{-\Gamma t + i\omega t} + C_2 \begin{pmatrix} -i \\ p \end{pmatrix} e^{-\Gamma t - i\omega t} \\ & - \frac{e^{i\Omega t}}{\omega^2 + (i\Omega + \Gamma)^2} \begin{pmatrix} \tilde{j} & \tilde{H}cp + \left|\frac{D_0}{G_0}\right| p\xi\tilde{j} \\ -\tilde{H}cp - \left|\frac{D_0}{G_0}\right| p\xi\tilde{j} & \tilde{j} \end{pmatrix} \begin{pmatrix} \frac{\omega^2}{\omega^2+\Gamma^2} i\Omega \\ \omega p + \frac{\omega\Gamma}{\omega^2+\Gamma^2} i\Omega p \end{pmatrix},\end{aligned} \tag{3.7}$$

where ω and Γ are the free oscillation frequency and the damping coefficient, and $\tilde{H} = \gamma H_0 l/(2\pi)$ and $\tilde{j} = b_j j_0$. The constants C_1 and C_2 are integration constants and depend on the initial vortex position. The trajectory of the vortex is then given by the real part of Eq. 3.7 and resembles an ellipse when reaching its steady state.

It is important to point out that this result should not be mistaken for a two-dimensional harmonic oscillator. While the latter possesses a four-dimensional phase space, i.e., two spatial and two momentum dimensions, the presented vortex model only has a two-dimensional phase space and is fully characterized by its spatial coordinates. This difference is due to the lack of an inertia term in the Thiele equation in Eq. (3.6).

3.2.3 | Experimental imaging

Experimentally, the current-driven vortex gyration has first been studied via a resistive measurement utilizing the anisotropic magnetoresistance effect [30]. Direct insights into the response of the magnetic domain were later provided by various imaging techniques [92, 146, 147]. In the following, I discuss two of these studies most relevant to this thesis. It is also important to point out that there are several investigations, with a focus on the vortex gyration driven by in-plane fields instead of currents [123, 148], some of which I further discuss in Chap. 3.3.

The first study imaging the time-resolved vortex gyration excited via spin-transfer torques was conducted by Bolte et al. [146]. They used scanning transmission X-ray microscopy to resolve the movement of the vortex core in a 2 µm×2 µm permalloy square at the Advanced Light Source in Berkley. This technique relies on X-ray magnetic circular dichroism, i.e., a difference in the absorption of circularly polarized X-rays depending on the angle and magnitude of the magnetization [149].

Bolte et al. imaged the gyration of a vortex driven by an in-plane current at an excitation frequency of 62.5 MHz. They compared their results to a case, where the vortex was driven by an in-plane magnetic field only. Specifically, they measured a difference in the phase of the two gyration trajectories with respect to the maximum of the driving

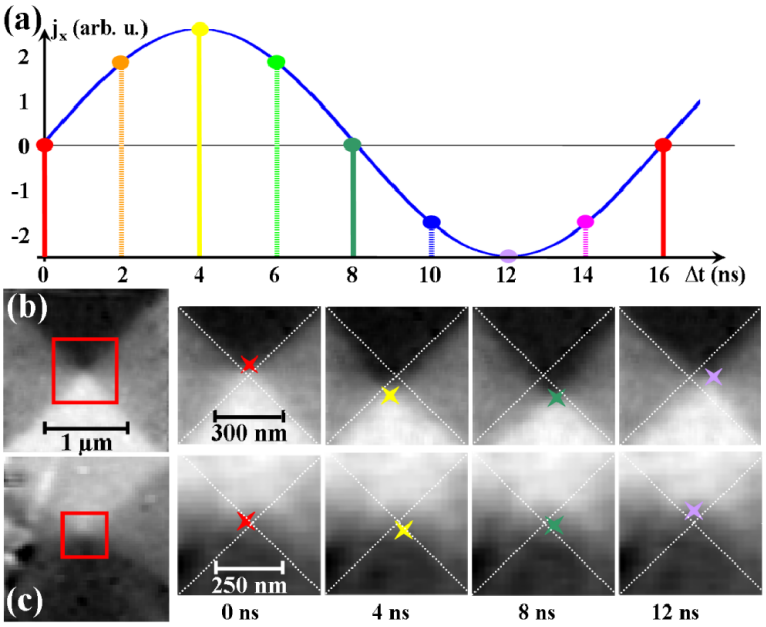

Figure 3.6: **Time-resolved STT-driven vortex gyration probed using scanning transmission X-ray microscopy.** (a) Schematic illustration of the phase of the current passing the sample in the horizontal direction. (b,c) STXM images of the hole vortex structure (left) and zoom-ins of the center (right). White and black regions in the image indicate the magnetization to be parallel or antiparallel to the horizontal x-axis. At the various excitation phases, the vortex is displaced from its equilibrium position following an elliptical orbit. Reprinted figure with permission from Ref. [146]. © 2008 by the American Physical Society

current. This led to the discovery of an additional in-plane magnetic field accompanying the spin-transfer torques and helped to guide the development of the model of the gyration detailed in Chap. 3.2.2.

In another work, Pollard et al. imaged the time-averaged trajectories of the current-driven vortex gyration using Lorentz microscopy for a larger range of excitation frequencies (c.f. Fig. 3.7) [92]. Using a self-build *in-situ* sample holder they were able to excite a permalloy nanostructure with an alternating in-plane current in their microscope. The electron microscope used for the study was equipped with a special Lorentz lens, which allows for higher magnifications in field-free conditions [150]. Thereby, they achieved a point-resolution of about 20 nm, estimated from the size of a vortex feature in a static image.

A set of micrographs showing the resulting vortex trajectories measured at various frequencies around the resonance is shown in Fig. 3.7a. As expected from the model de-

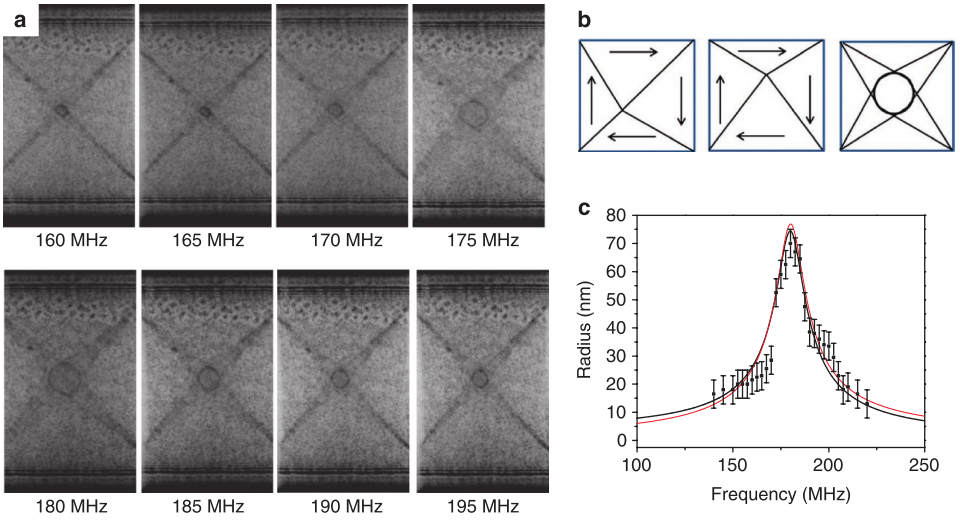

Figure 3.7: **Spin-transfer torque driven vortex gyration imaged using Lorentz microscopy.** (a) Series of Lorentz micrographs of the time-averaged trajectory of the vortex core excited at various frequencies. (b) Schematics of the vortex domains during different phases of the excitation. Time-averaged, the trajectory resembles the shape of an ellipse. (c) Gyration radius as a function of driving frequency. Reproduced with permission from Springer Nature from Ref. [92]. © 2012 Nature Publishing Group

tailed in Chap. 3.2.2, they found the ellipticity of the gyration to change with frequency, becoming almost circular at resonance. By measuring the trajectory size for both vortex helicities, they were able to factor out the effects of the in-plane magnetic field accompanying the current. This, together with a micromagnetic simulation, allowed them to estimate a lower bound for the nonadiabaticity factor ξ.

Interestingly, the resonance curve they present (c.f., Fig. 3.7c) is not smooth but shows jumps at certain frequencies. Although, this indicates the presence of defects their influence cannot be directly investigated by this time-averaged measurement. Studies directly aimed at the investigation of the effects of defects in the nanostructure are the topic of the next section.

3.3 | Pinning and gyration of magnetic vortices in the presence of defects

The first types of defects investigated in the context of confined vortices were artificially introduced to the sample [132, 151–155]. For example, it could be shown, that magnetic vortices are attracted by holes in the magnetic material, which also leads to a suppres-

sion of its gyrotropic motion [132, 153]. This is due to avoiding the high cost of exchange energy of the vortex core. Besides their artificial introduction, defects can also occur naturally in nanostructured magnetic films, which I discuss in more detail in the following chapter.

For atomically flat samples spin-polarized scanning tunneling transmission microscopy provides sub-nanometer resolution. It allowed the discovery of a short-range repulsive and long-range attractive pinning potential between the vortex core and adatoms on the surface of magnetic nanostructures [156]. While intrinsic defects in polycrystalline samples have also been investigated using nanomechanical torque magnetometry [157], the majority of studies have been performed in the groups of Paul A. Crowell [158–160] and Jesse Berezovsky [161–164] using time-resolved Kerr microscopy.

Figure 3.8 details a sketch of the setup and the typical Kerr signal recorded in an experiment conducted in the group of Paul A. Crowell [159]. With their setup, they displaced the vortex core in a magnetic nanoisland using a short magnetic pulse and followed its gyration to its equilibrium position by measuring the change in the Kerr signal of the tightly focused static laser spot on the sample. The magnetic pump pulse was generated by passing a current pulse through a stripline below the sample, synchronized to the laser pulse probing the magnetization. By increasing the delay between the pump and probe pulse, they were able to follow the temporal evolution of the damped gyration (cf. Fig. 3.8). To study the effect of intrinsic defects in the sample, they additionally applied static magnetic fields in both in-plane directions to move the equilibrium position of the core (see Chap. 3.2.1).

They found that for large field pulses, the vortex core would initially gyrate at a frequency predicted via analytical and micromagnetic models solely by the size and magnetic properties of the nanoisland. Below a certain field threshold, however, the gyration frequency would increase above the analytically predicted value and would show strong variations with the static in-plane fields.

By raster-scanning the in-plane fields, they were able to map out the variations in the gyration frequency for samples with different grain sizes. The resulting contours together with representative atomic force micrographs of the films used to prepare the nanostructures are shown in Fig. 3.9. While there is no direct correspondence between the grain size and the distribution of defects (which can be identified as peaks in Figs 3.9a-c), one can see that the average distance between the defects increases, with increasing grain size.

In a later work, the group of Paul A. Crowell used a similar technique to demonstrate that vortex pinning is correlated to surface roughness [160]. They prepared samples with varying surface roughness and estimated the depth of the local pinning potential

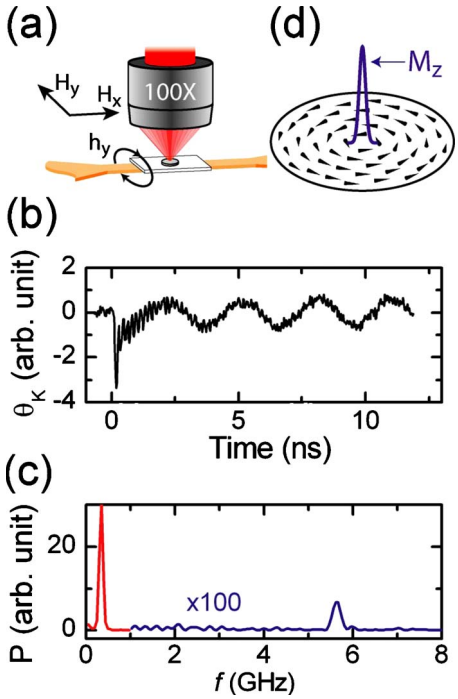

Figure 3.8: **Free vortex gyration after core displacement by a short magnetic field pulse studied via time-resolved Kerr microscopy.** (a) Magnetization in a magnetic nanostructure is probed using a focused laser spot via the magneto-optical Kerr effect. A pulse in a stripline below the sample generates a magnetic field pulse to displace the vortex. Static in-plane fields are used to shift the equilibrium position of the core. (b) Kerr angle after the field pulse as a function of time. A quickly decaying high-frequency signal indicates the generation of spin waves. It overlays the slowly decaying low-frequency signal from the gyration of the vortex to its equilibrium position. (c) The spectrum of the signal in (b), showing its high- and low-frequency components. (d) Illustration of the magnetization inside the round nanostructure. Reprinted figure with permission from Ref. [159]. © 2010 by the American Physical Society

from the amplitude of the static in-plane field needed to depin the core from a defect. They found, that the average pinning energy increases if the surface roughness on the length scale of the vortex core increases.

The group of Jesse Berezovsky developed a similar experimental approach to study vortex pinning slightly altering the type of excitation [161–164]. Instead of displacing the core with a short current pulse, they generate a sinusoidal magnetic field at 15 kHz using a stripline. Since this frequency is much smaller than the gyration frequency, which is on the order of tens or hundreds of megahertz, this field probes the static pinning of vortices. Based on a slow change of the maximum and minimum amplitude of the alternating field, they developed a procedure that allows them to calculate the one-

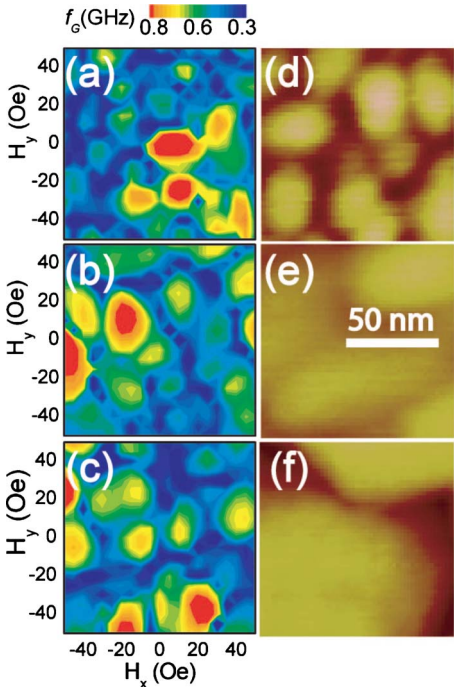

Figure 3.9: **Variations of the gyration frequency for samples of different grain sizes.** (a-c) Variations in the gyration frequency for small displacement pulses mapped as a function of the static in-plane fields. The grain size of the samples increases from top to bottom. (d-f) Atomic force micrographs of the unpatterned films corresponding to the samples in (a-c), demonstrating the different grain sizes of the prepared films. Reprinted figure with permission from Ref. [159]. © 2010 by the American Physical Society

dimensional pinning potential along the field direction. A perpendicular static in-plane field allows the consecutive acquisition of a series of one-dimensional pinning fields to construct maps of the local pinning energy as shown in Fig. 3.10. This approach allowed identifying the cause of the strongest pinning centers to be protrusions on the surface of the nanostructure.

There also exist some theoretical studies on the pinning of vortices in nanostructures. This includes a micromagnetic simulation, studying the vortex gyration in nanostructures with local variations of the saturation magnetization [165, 166]. These variations shall imitate a fluctuation in the film thickness and were shown to lead to increased damping of the gyration. Another study developed a higher-order model for the vortex potential, extending the rigid-vortex model It takes into account the deformation of the magnetic domains under pinning, which is necessary if very deep pinning potentials are encountered [136].

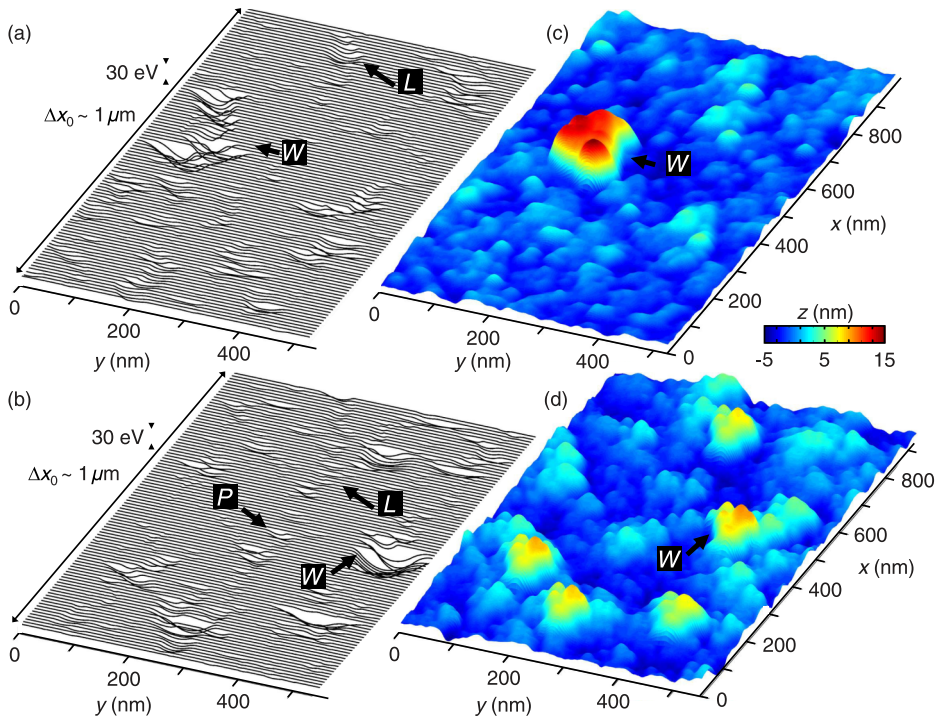

Figure 3.10: **Pinning energy landscape and topography of two permalloy nanoislands.** (a,b) Two-dimensional maps of the pinning potential compiled from a sequence of one-dimensional pinning potentials for two permalloy nanoislands. (c,d) Topographical map of the same samples as in (a,b) measured via atomic force microscopy.
Reprinted figure with permission from Ref. [162]. © 2016 by the American Physical Society

4

Few-nm tracking of current-driven magnetic vortex orbits using ultrafast Lorentz microscopy

Marcel Möller[1], John H. Gaida[1], Sascha Schäfer[1] and Claus Ropers[1]

Communications Physics **3**, 36 (2020)

[1]4th Physical Institute-Solids and Nanostructures, University of Göttingen, 37077 Göttingen, Germany.

DOI:https://doi.org/10.1038/s42005-020-0301-y

Abstract

Transmission electron microscopy is one of the most powerful techniques to characterize nanoscale magnetic structures. In light of the importance of fast control schemes of magnetic states, time-resolved microscopy techniques are highly sought after in fundamental and applied research. Here, we implement time-resolved Lorentz imaging in combination with synchronous radio-frequency excitation using an ultrafast transmission electron microscope. As a model system, we examine the current-driven gyration of a vortex core in a 2 µm-sized magnetic nanoisland. We record the trajectory of the vortex core for continuous-wave excitation, achieving a localization precision of ± 2 nm with few-minute integration times. Furthermore, by tracking the core position after rapidly switching off the current, we find a transient increase of the free oscillation frequency and the orbital decay rate, both attributed to local disorder in the vortex potential.

4.1 | Introduction

Magnetism gives rise to an incredibly rich set of nanoscale phenomena, including topological textures such as skyrmions [3–5] and vortices [1]. Dynamical control of spin structures down to sub-picosecond timescales is facilitated by a multitude of interactions involving spin-torques [32–34] or optical excitations [20–23]. These features have shown immediate relevance in novel applications, exemplified in (skyrmion) racetrack memory [10, 11], magnetic random access memory [38], and vortex oscillators as radio-frequency sources [18, 19] or for neuromorphic computing [15, 16]. Observing these magnetic phenomena on their intrinsic length and time scales requires experimental tools capable of simultaneous nanometer spatial and nanosecond to femtosecond temporal resolution. Whereas photoelectron [167] and magneto-optical schemes using pulsed radiation sources from the visible [168] to the x-ray [169–171] regime inherently offer high temporal resolution, the particular advantages of electron beam techniques have yet to be fully exploited in the ultrafast domain.

Transmission electron microscopy (TEM) facilitates quantitative magnetic imaging with very high spatial resolution approaching the atomic level using aberration-corrected instruments [172, 173] and holographic approaches [150, 174–176], while also allowing for structural or chemical analysis. Importantly, the versatile *in-situ* environment of TEM enables the observation of nanoscale magnetic changes with optical [23, 24, 177] or electrical stimuli [92, 178, 179]. Time-resolved transmission electron microscopy [78, 82, 180] has in some instances been used to address magnetization dynamics [44, 81, 104, 181]. The recent advance of highly coherent photoelectron sources [46, 47] promises

substantially enhanced contrast and resolution in ultrafast magnetic imaging [48], but has, to date, not been combined with synchronized electrical stimuli.

In this work, we address this problem and realize ultrafast Lorentz microscopy with *in-situ* radio-frequency (RF) current excitation. The technique is made possible by using a transmission electron microscope with a pulsed photoelectron source. Synchronizing the electron pulses at the sample with the radio-frequency current, images of the instantaneous state of the system for a given RF phase can be acquired. The controlled variation of the phase allows for recording high-speed movies with a temporal resolution independent of the readout speed of the detector, but given by the duration of the electron pulses and the quality of the electrical synchronization.

4.2 | Results

4.2.1 | Time-resolved Lorentz Microscopy

The experiments were conducted at the Göttingen Ultrafast Transmission Electron Microscope (UTEM), which features ultrashort electron pulses of high beam quality from a laser-triggered field emitter [46]. Employing a linear photoemission process, the UTEM allows for a flexible variation of the electron pulse parameters in terms of repetition rate and pulse duration [46, 91]. In the present study, we employ electron pulses at a repetition rate of 500 kHz, driven by frequency doubled optical pulses from an amplified Ti:Sapphire laser with a central wavelength of 400 nm and a pulse duration of 2.2 ps.

We demonstrate the capabilities of our instrument by studying the model system of a spin-transfer torque driven vortex oscillator [29, 123, 146, 181, 182]. The sample is a $2.1 \times 2.1\,\mu m^2$ large and 26 nm thick polycrystalline permalloy ($Ni_{81}Fe_{19}$) square. Its magnetic configuration consists of four domains forming a flux closure (Landau) state with an in-plane magnetization pointing along the edges of the nanoisland and a perpendicular magnetized core with a diameter on the order of 10 nm [1, 118]. The curl c specifies whether the in-plane magnetization rotates counter-clockwise ($c = +1$) or clockwise ($c = -1$), whereas the polarity p indicates if the core magnetization is parallel ($p = 1$) or antiparallel ($p = -1$) to the z-axis of the coordinate system defined in Fig. 4.1.

Two edges of the structure are electrically contacted with 100 nm thick gold electrodes (see Fig. 4.1) which terminate in wire-bonding pads. The sample is installed in a custom-made TEM holder that allows for *in-situ* RF-current excitation up to the GHz-regime [92, 178, 179]. RF-currents are generated with an arbitrary waveform generator (AWG) synchronized to the photodiode signal from the laser oscillator. This allows us to create custom waveforms, such as continuous or few-cycle sine waves, with a fixed,

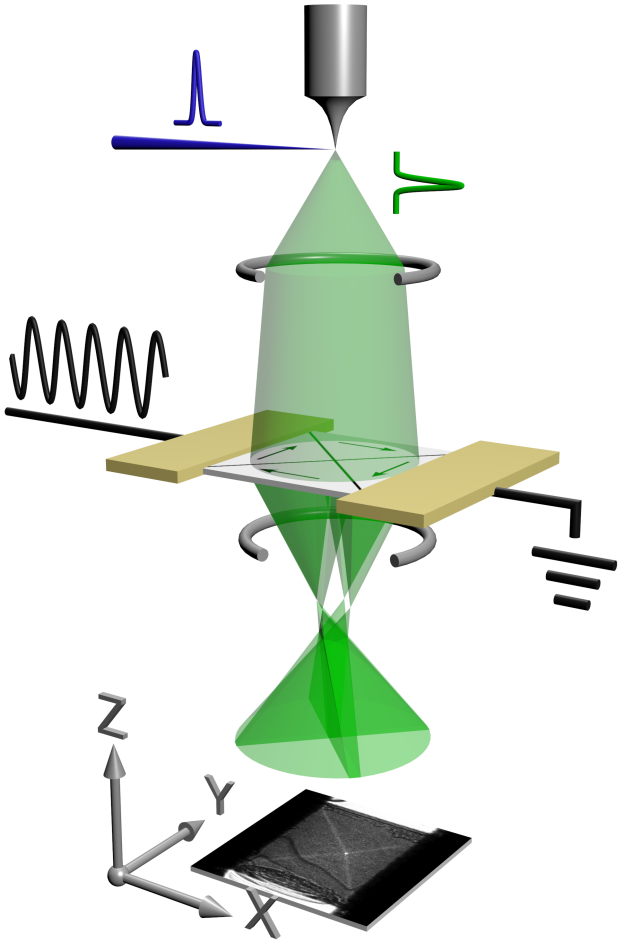

Figure 4.1: **Schematic representation of time-resolved Lorentz microscopy combined with synchronous radio-frequency sample excitation.** An ultrashort electron pulse (green) is generated via a linear photoemission process from an optical laser pulse (blue) inside the electron gun. A magnetic sample (light grey) is stroboscopically illuminated with a near-parallel electron beam and imaged onto a TEM camera. Employing a small defocus in the imaging conditions gives rise to magnetic contrast (exemplary image shown in the bottom). Dynamics in the sample are excited *in-situ* with radio-frequency currents (black) phase-locked to multiples of the laser repetition rate, creating the appearance of a static image. A controlled change of the radio-frequency phase between images allows the entire dynamic process to be mapped in time.

software-programmable timing between the probing electron pulse and the phase of the excitation. Driven by alternating currents, the vortex structure exhibits a resonance behaviour, in which the core traces out an ellipsoidal trajectory [92, 137, 138, 182]. The trajectory of the vortex core under the simultaneous influence of spin-transfer torques

and Oersted fields is predicted by a harmonic oscillator model [137, 138].

To image the magnetic configuration of our sample, we employ Fresnel-mode Lorentz microscopy [58, 183], a form of defocus phase contrast (see Fig. 4.1). In a classical picture, magnetic contrast arises from the Lorentz force: When the parallel beam of electrons passes through the magnetic field of the sample, electrons experience a momentum change perpendicular to their propagation direction and proportional to the local magnetic field. By slightly defocusing the imaging system of the microscope, this transverse momentum gives rise to a contrast which scales with the magnitude of the z-component of the curl of the sample's induction [58, 183].

A Lorentz micrograph of the sample acquired with a continuous electron beam is depicted in the bottom of Fig. 4.1. The X-shaped lines indicate the position of the domain walls. A peak in the contrast arises at the intersection of the domain walls, and marks the position of the vortex core. The core itself does not contribute to the magnetic contrast, as its magnetization points along the beam propagation direction. The dark lines in the lower half of the image are Bragg lines of the single-crystal silicon substrate, which locally scatter intensity out of the forward beam, and the dark areas at the lateral edges stem from the gold contacts.

4.2.2 | Continuous Excitation

In a first experiment, we excite the vortex with a continuous sinusoidal current at a frequency of $f_{\mathrm{ex}} = 101.5\,\mathrm{MHz}$. This frequency maximizes the orbit diameter of the gyration, as determined from a preliminary measurement using a continuous electron beam (see Chap. 4.3.2). To resolve a whole period, we acquire images for 21 delays t at intervals of 500 ps. At every delay t, we record 32 time-resolved micrographs, each with an integration time of one minute. The delay times given are quantitative with respect to the maximum of the driving field, enabled by *in-situ* electron beam deflection near the contacts (see Chap. 4.3.4) [178]. After applying a drift-correction, we sum over identical micrographs and obtain a movie of the vortex dynamics, which is presented in Supplementary Movie 1 [184].

Between the four exemplary frames in Fig. 4.2 a, acquired at time steps of 2.5 ns, the vortex core is clearly displaced and performs a clockwise rotation, implying a polarity of $p = -1$ [29, 138]. The curl of the vortex is $c = -1$, determined from the contrast of the domain walls (bright or dark; here: bright) and the choice of imaging conditions (over- or underfocus; here: overfocus) [117]. Line profiles along the x-direction at the position of the vortex core are displayed in Fig. 4.2 b, following a near-sinusoidal trajectory. The inset in Fig. 4.2 b depicts a single line profile (blue line) with a Lorentzian line-shape

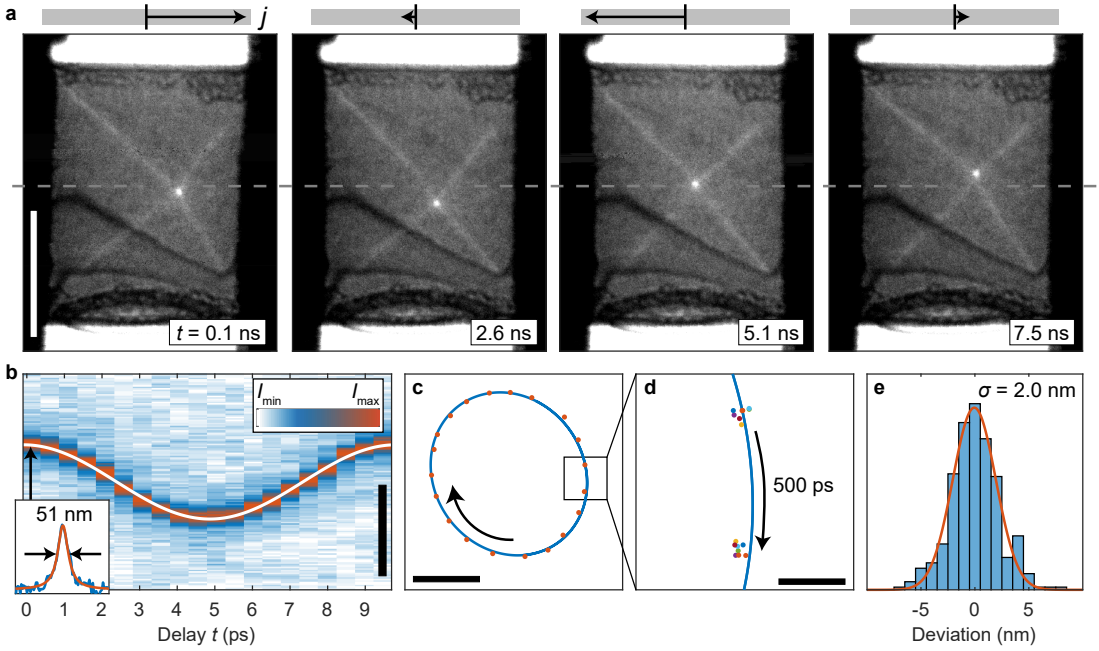

Figure 4.2: **Continuous-wave excitation at a frequency of $f_{ex} = 101.5\,\mathrm{MHz}$ and a current density of $j = 1.7 \times 10^{11}\,\mathrm{A\,m^{-2}}$.** (a) Four time-resolved Lorentz micrographs acquired in time steps of 2.5 ns at a defocus of 520 µm (scale bar: 1 µm). (b) Line profiles at the position of the vortex core along the x-direction, closely resembling a sinusoidal displacement. White: Best fit of a harmonic oscillator model (scale bar: 300 nm). (b, Inset) Blue: Example of a single line profile at $t = 0.1$ ns. Red: Fitted Lorentzian line shape. (c) Red: Mean vortex core position determined from set of 8 identical Lorentz micrographs at each delay t. Blue: Best fit of the harmonic oscillator model (scale bar: 100 nm). (d) Example of the spatial spread of the tracked vortex position (scale bar: 20 nm). (e) Distribution of the spatial deviation from the mean for all position measurements in x- and y-direction.

(red line) fitted to the data. The mean full-width-half-max (FWHM) of the the peak is 51 ± 1 nm, averaged over all delays t and both spatial dimensions. It should be noted, that this size does not represent the vortex core diameter – which is expected to be on the order of 10–20 nm [120] – but is a result of the imaging conditions. Thus, it represents an upper limit for the magnetic point resolution and constitutes the best spatial resolution of stroboscopic Lorentz-microscopy to date.

Due to the high signal-to-noise ratio, the position of the vortex core can be tracked with a precision far below the point resolution, as shown in the following. From the 32 images for every delay t, we form a set of eight identical images, each corresponding to an integration time of 4 min. In a single image, the position of the vortex core is

determined by the center of mass of the peak. To visualize the position of the vortex core during one oscillation period, we average over the eight individual measurements (Fig. 4.2 c). An example of their distribution is shown in Fig. 4.2 d. One can clearly see that the points accumulate in an area with a diameter of less than 10 nm. This is significantly smaller than the FWHM of the peak in the image contrast. The deviations from the mean of all position measurements are combined in Fig. 4.2 e. The histogram follows a Gaussian distribution with a standard deviation of $\sigma = 2\,\mathrm{nm}$, corresponding to the localization precision of $\pm 2\,\mathrm{nm}$ in each spatial dimension.

Knowledge of the absolute timing of the vortex gyration with respect to the driving current allows us to directly fit our results to the oscillator model presented by Krüger *et al.* [137] (see Chap. 4.3.5). Although the fitted trajectory agrees well with the data (white and blue lines in Figs. 4.2 b, c), the obtained resonance parameters of the free oscillation frequency $f_0 = 97.9 \pm 2.1\,\mathrm{MHz}$ and the damping $\Gamma = 74 \pm 13\,\mathrm{MHz}$ indicate a limitation of the description. Specifically, the damping appears unrealistically high, given the resonance curve presented in Chap. 4.3.2 and previous measurements [92]. This suggests that additional contributions in the restoring force or the damping may affect the vortex motion, arising, for example, from local disorder [158, 159, 165, 166, 185, 186] or global anharmonicities in the vortex potential (e.g., cubic corrections to the harmonic vortex potential) [155, 187–189]. In order to obtain direct time-domain information on the damping and possible deviations from a harmonic confinement, we conduct measurements of the free-running relaxation of the vortex in the absence of a driving force.

4.2.3 | Damped Motion

In the following measurements performed at the same sample, a current at an identical frequency of $f_{\mathrm{ex}} = 101.5\,\mathrm{MHz}$ is applied for a duration of 1 µs, and is switched off at a zero-crossing of the sine wave at $t = 0$ (see inset of Fig. 4.3 a). Again, the timing was directly determined via small-angle scattering in the vicinity of the permalloy square.

At delay steps of 1 ns, we acquire Lorentz micrographs with an integration time of 3 min. An assembled movie of the data is found in Supplementary Movie 2 [184]. The path of the core to its rest position is clearly visible both in the line profiles along the x-axis (Fig. 4.3 a) and in the tracked position of the vortex core (Fig. 4.3 b). A two-dimensional representation of the complete trajectory is given in Fig. 4.3 c. As can be seen from the sense of rotation in Fig. 4.3 c, the vortex polarity is $p = +1$ for this measurement. Thus, we chose a slightly higher current density of $j = 2.9 \times 10^{11}\,\mathrm{A\,m^{-2}}$, which compensates for the smaller orbits in case of an opposite sign between curl and

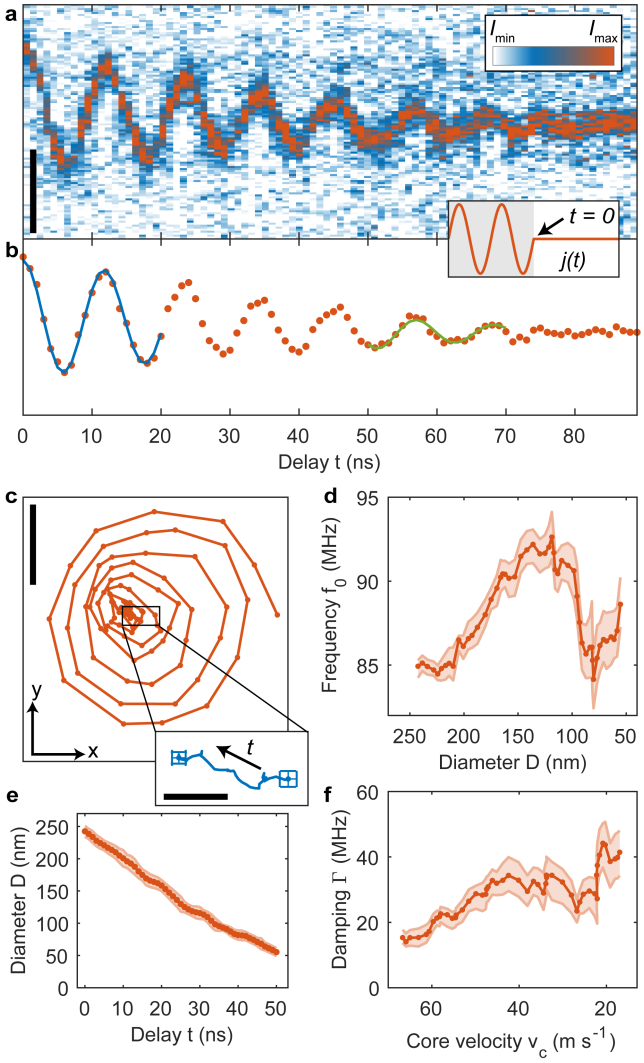

Figure 4.3: **Damped vortex gyration after switching off the current ($f_{ex} = 101.5$ MHz, $j = 2.9 \times 10^{11}$ A m^{-2}).** (a) Profiles of the vortex core along the x-axis, illustrating the damped sinusoidal motion towards the equilibrium position (scale bar: 200 nm). (b) Red: Tracked x-position of the vortex core as function of t (scale bar as in (a)). Blue/green: First/last result of the moving-window fit to the vortex trajectory. (c) Spatial vortex core trajectory during the damping. Spacing between the dots is 1 ns (scale bar: 100 nm). (c, Inset) Center of the gyration moving over time as determined from the fit (scale bar: 20 nm). (d, e, f) Fit results of the windowed fit. Shaded regions are one-sigma confidence intervals: (d) Free oscillation frequency f_0 as a function orbit diameter D. (e) Mean orbit diameter D over delay t. (f) Damping Γ as a function of the vortex core velocity v_c.

polarity (Eq. 4.2) [137].

The trajectory obtained can not be expressed in terms of a single exponentially decaying sinusoidal function, illustrating systematic deviations from the damped harmonic oscillator model. However, we can extract the momentary frequency and decay rate of the oscillation by fitting an exponentially decaying orbit in a moving window with a size of 20 ns. The blue and green curves in Fig. 4.3 b display the fitted x-component for windows starting at $t_w = 0$ ns and $t_w = 50$ ns, respectively. Good agreement was also obtained for all intermediate values.

The results of the fit are summarized in Figs. 4.3 d-e. The temporal evolution of the orbit diameter D exhibits an approximately linear rather than exponential decay (Fig. 4.3 e) In particular, this can also be seen from the increase of the instantaneous damping Γ, which is plotted as a function of the vortex core velocity v_C in Fig. 4.3 f. The trajectory further experiences a transient rise of the momentary frequency f_0 (Fig. 4.3 d) from 85 to about 92 MHz at medium orbit diameters D. Moreover, allowing for a variable gyration center, we find that the windowed fit reveals a continuous translation of the orbit towards the left (inset of Fig. 4.3 c).

The transient acceleration of the gyratory motion implies the presence of disorder in the vortex potential, and is consistent with time-resolved optical studies [158, 159]. Similarly, the movement of the orbit center suggests a trapping of the vortex core in a pinning site and is further supported by the broadening of the profile in Fig. 4.3 a for delays $t > 80$ ns, likely caused by a stochastic motion at very small diameters. As mentioned above, such frequency shifts have been characterized by other approaches [19, 158, 159]. Yet, we have not encountered a real-space measurement of the type of damping observed here. A micromagnetic theoretical study by Min *et al.* [166] points towards a possible microscopic origin of the enhanced dissipation. In that work, spatial disorder in the form of variations in the saturation magnetization was found to cause additional damping via deformations of the internal magnetic structure of the vortex. While our observations, in agreement with the theoretical calculations, show an increase in f_0 and Γ, particular differences are apparent. Specifically, the damping growth is much more pronounced in our case, such that the ratio Γ / f_0 increases over time, whereas Min *et al.* have found that it is decreasing [166]. Therefore, our measurements suggest additional contributions to the disorder potential, such as magnetic anisotropy or non-magnetic voids [185]. A detailed modeling may be guided by further correlative studies of the structural and chemical composition, facilitated by nanoscale diffraction and spectroscopy available in transmission electron microscopy.

In conclusion, we implemented ultrafast Lorentz microscopy with synchronous radio-frequency current excitation and demonstrated its high spatio-temporal resolution by

mapping the time-resolved gyration of a magnetic vortex core with an precision of $\pm 2.0\,\mathrm{nm}$. Future developments will include higher contrast and spatial resolution from enhanced beam coherence, increased sensitivity from larger duty-cycles and frequencies up to the terahertz range. In combination with more advanced imaging techniques like transport-of-intensity [58] based magnetization reconstructions or electron holography [150, 174–176], this will enable quantitative imaging of magnetic textures on ultrafast time scales. In our opinion, exposing spin textures, such as vortices and skyrmions, to electrical and electromagnetic stimuli and observing the nanoscopic response will make valuable contributions to fundamental research and device development in ultrafast magnetism. Moreover, the approach can be readily extended to *in-situ* phase contrast imaging in different areas, including electrical switching of multiferroic materials and other correlated systems and heterostructures.

4.3 | Methods

4.3.1 | Instrumentation

The data was acquired at a JEOL 2100F TEM at an acceleration voltage of 120 kV. The microscope is equipped with a Gatan Ultrascan US4000 camera and features an electron gun allowing for a photoemission of electron pulses. Details concerning the electron source have been presented by Feist *et al.* [46]. Fresnel imaging was performed at a defocus of 520 µm at a low magnification imaging mode, in which the main objective lens is current-free with a small residual field of about 10 mT. The laser system in use is a Ti:Sa regenerative amplifier and seed laser manufactured by Coherent, which outputs 35 fs pulses at a repetition rate of $f_{\mathrm{rep}} = 500\,\mathrm{kHz}$ and a central wavelength of 800 nm. The output of the amplifier is frequency doubled using a β-Barium borate crystal and subsequently stretched to 2.2 ps in a 10 cm SF6 bar before it is focused onto the electron source.

The design of our self-made sample holder is based on that of Pollard *et al.* [92] and consists of a coaxial SMA vacuum feedthrough and a coaxial vacuum cable connected to a coplanar waveguide on a printed circuit board. The laser amplifier system provides an electrical trigger signal which is synchronized to its optical output. This signal is fed into the trigger input of a Keysight 81160A arbitrary waveform generator, where it initiates the output of a sinusoidal wave with a fixed number of cycles n_{Burst}. For a quasi-continuous excitation of the sample, the burst number and the excitation frequency are set to the same multiple of the repetition rate of the laser amplifier, i.e. $f_{\mathrm{ex}} = n_{\mathrm{Burst}} \cdot f_{\mathrm{rep}}$.

For non-continuous excitations, there is no constraint on the waveform other than it being shorter than $1/f_{\mathrm{rep}}$.

In quasi-continuous operation special care has been taken to achieve a glitch- and gap-free output by monitoring the signal with a directional coupler (Mini-Circuits ZFDC-20-4L) and an oscilloscope (Tek DPO71604C with 16 GHz bandwidth). Additionally, we placed a 6 dB attenuator after the generator output to suppress standing waves at the RF transmission line, originating from the unmatched sample and a parasitic capacitance of the generator output.

4.3.2 | Sample System and Reference Measurements

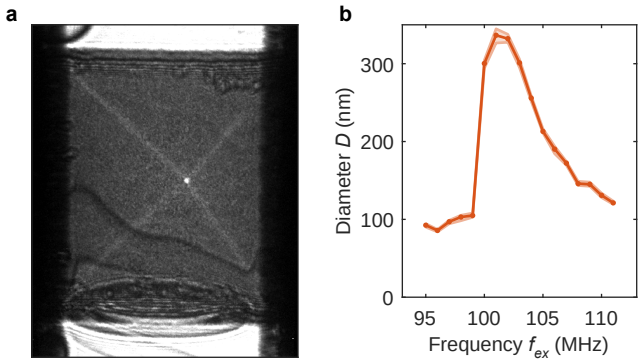

Figure 4.4: **Preliminary characterization of the sample utilizing an continuous electron beam.** (a) Lorentz-micrograph of the unexcited sample system acquired under continuous illumination (scale bar: 1 µm). (b) Orbit-diameter of the vortex gyration as a function of the driving frequency f_{ex}. Shaded regions are one-sigma confidence intervals obtained via bootstrapping the fitting routine.

The sample consists of a 26 nm thick permalloy ($Ni_{81}Fe_{19}$) square of $2.1 \times 2.1\,\mu m^2$ size, which is electrically connected with two gold contacts (100 nm thickness). From a comparison between experimental and simulated Fresnel images, we obtain a saturation magnetization of about $M_S = 600\,\mathrm{kA\,m^{-1}}$ (see Chap. 4.4.1). The substrate is a single crystalline, 35 nm thick silicon membrane with $100 \times 100\,\mu m^2$ windows. The magnetic structure and the contacts were fabricated using electron beam lithography and thermal evaporation. The quality of the lift-off was confirmed using Fresnel imaging, as fabrication errors (e.g., residual magnetic material in the center of the sample) would show up as strong phase objects. A Lorentz micrograph of the unexcited sample recorded with a continuous electron beam is depicted in Fig. 4.4 a. In its equilibrium position, the vortex

core is slightly shifted to the right, which is likely caused by a residual out-of-plane field of the current-free objective lens in combination with a small tilt of the sample.

The resonance curve of the vortex oscillator (Fig. 4.4 b) was determined from a Lorentz image series acquired prior to the time-resolved measurement using a continuous electron beam [92]. A maximum response near $f_{ex} = 101.5\,\mathrm{MHz}$ is found. Below and above frequencies of 95 MHz and 111 MHz, respectively, the vortex core is pinned and remains stationary.

A comment should be made about possible influences of Joule heating in the time-resolved experiments. The saturation magnetization directly affects the integrated intensity of the vortex feature above the background. From a comparison of the image contrast with and without excitation (Fig. 4.2 a at $t = 0$, and Fig. 4.4 a), this intensity varies by less than ten percent upon current excitation, within the margin of error. We can thus rule out a significant thermal reduction of the saturation magnetization. For the measurements in Fig. 4.3, despite a higher current density in the 5 cycles before switching off the current, the average thermal load was lower than in the measurement under continuous excitation. This was achieved by reducing the current amplitude prior to the last 5 cycles.

4.3.3 | Tracking the vortex core

To track the position of the vortex core, we denoised the frames by applying a 3 x 3 pixel^2 (4.85 nm/px) median filter and calculated the center of mass of the pixels of maximum intensity. These pixels were selected via thresholding. The threshold is chosen such that the contributing pixels correspond to a region of about 50 nm in diameter.

4.3.4 | Determination of time-zero

We utilize a diffraction mode with long camera length to determine the absolute timing of the current through the nanoisland by measuring the electrical field between the gold contacts [178]. Therefore, we form a parallel electron beam close to an edge of an Au electrode in a sufficient distance to the permalloy. This ensures that the electrons are only deflected due to the electric field between the contacts. In diffraction mode, this beam converges to a single point. Choosing a long camera length, we can image a deflection of this spot which is directly proportional to the electric field.

To determine $t = 0$ of the first measurement (continuous sinusoidal excitation), we fit a cosine-function to the delay-dependent position of the electron spot. For the second

measurement of the damped motion, we probe delays before and after $t = 0$, which allows us to directly find the last zero-crossing of the sinusoidal current.

4.3.5 | Harmonic Oscillator Model

Passing a current through a non-magnetic/magnetic (Au/Py) interface spin polarizes this current due to a difference in the scattering probability between the majority and minority electrons in the conduction band of the magnetic layer [32]. This spin-polarized current exerts a torque on the magnetic domains, altering their configuration and resulting in a displacement of the vortex core. Zhang and Li derived a general micro-magnetic model accounting for adiabatic and nonadiabatic contributions to this spin-transfer-torque (STT) by extending the the Landau-Lifshitz-Gilbert (LLG) equation [141]. Based on a generalized Thiele equation [143, 145], Krüger *et al.* published a harmonic oscillator model for the movement of a vortex core in a square magnetic thin film, which takes in-plane Oersted fields as well as spin-transfer torques into account. These Oersted fields originate in an inhomogeneous current density inside the magnetic conductor [137, 138, 146]. Krüger *et al.* specify the resulting steady state trajectory under the influence of a driving current $\mathbf{j}(t) \propto \exp(i\Omega t)\,\mathbf{e}_x$ and field $\mathbf{H}(t) \propto \exp(i\Omega t)\,\mathbf{e}_y$ as [137]:

$$\begin{pmatrix} X \\ Y \end{pmatrix} = \mathrm{Re}\left[-\frac{e^{i\Omega t}}{\omega^2 + (i\Omega + \Gamma)^2} \begin{pmatrix} \tilde{j} & \tilde{H}cp + \left|\frac{D_0}{G_0}\right| p\xi\tilde{j} \\ -\tilde{H}cp - \left|\frac{D_0}{G_0}\right| p\xi\tilde{j} & \tilde{j} \end{pmatrix} \begin{pmatrix} \frac{\omega^2}{\omega^2+\Gamma^2} i\Omega \\ \omega p + \frac{\omega\Gamma}{\omega^2+\Gamma^2} i\Omega p \end{pmatrix} \right] \tag{4.1}$$

with $\tilde{H}$ and $\tilde{j}$ the normalized magnitudes of the Oersted-field and the spin-polarized current, $\Omega = 2\pi f_{\mathrm{ex}}$ the driving frequency, $\omega = 2\pi f_0$ the free oscillation frequency, Γ the damping constant and $|D_0/G_0|$ a ratio related to exact magnetic distribution inside the nanoisland. The non-adiabaticity parameter ξ describes the ratio between non-adiabatic and adiabatic contributions in the LLG equation.

The scalar prefactor together with the vector define a trajectory in the form of an ellipse. Due to its symmetry, the matrix in ((4.1)) only introduces a rotation and an isotropic dilation to this ellipse. Parameters such as the ellipticity and the phase of the gyration (i.e., the position of the core with respect to the major axis of the ellipse at $t = 0$) are independent of this matrix. Therefore, we can simplify Eq. (4.1) to

$$\begin{pmatrix} X \\ Y \end{pmatrix} = \mathrm{Re}\left[-\frac{e^{i\Omega t}}{\omega^2 + (i\Omega + \Gamma)^2}\, A\, \hat{R}(\theta) \cdot \begin{pmatrix} \frac{\omega^2}{\omega^2+\Gamma^2} i\Omega \\ \omega p + \frac{\omega\Gamma}{\omega^2+\Gamma^2} i\Omega p \end{pmatrix} \right] \tag{4.2}$$

with an isotropic dilation A and a rotation of the ellipse by angle θ defined by the rotation matrix $\hat{R}(\theta)$. From the vector in Eq. (4.2) it follows directly that the sense of the rotation depends only on the core polarization p, with $p = +1/-1$ resulting in a counter-clockwise/clockwise rotation [146].

The trajectory in Eq. (4.2) has five measurable parameters, which equals the number of degrees of freedom of an ellipse (length of the two semiaxes, tilt, frequency) plus an initial phase. This allows us to directly fit the model to our measurement of the continuously driven oscillation by solving the overdetermined system of 42 equations ($X(t)$ and $Y(t)$ for every delay t). As the driving frequency is known, we fix it to $f_{\mathrm{ex}} = 101.5\,\mathrm{MHz}$. The best fit ($f_0 = 97.9 \pm 2.1\,\mathrm{MHz}$, $\Gamma = 74 \pm 13\,\mathrm{MHz}$) is shown as solid line in Fig. 4.2 b (white) and Figs. 4.2 c, d (blue). The errors in the fitted values correspond to 1σ-confidence intervals determined by bootstrapping [190].

Data availability

The data that support the findings of this study are available from the corresponding author on request.

Acknowledgement

We thank Johannes Riebold for his help in designing and testing the *in-situ* TEM Holder. Furthermore, we acknowledge useful discussions with Mathias Kläui, Henning Ulrichs and Michael Vogel and assistance from the Göttingen UTEM Team, especially Armin Feist, Nara Rubiano da Silva, Nora Bach, Thomas Danz and Karin Ahlborn. This work was funded by the Deutsche Forschungsgemeinschaft (DFG) in the Collaborative Research Center "Atomic Scale Control of Energy Conversion" (DFG-SFB 1073, project A05) and via resources from the Gottfried Wilhelm Leibniz-Price. We gratefully acknowledge support by the Lower Saxony Ministry of Science and Culture and funding of the instrumentation by the DFG and VolkswagenStiftung.

Author Information

Contributions

C.R., S.S. and M.M. conceived the project. M.M. prepared the sample. M.M. conducted the experiment with help from J.H.G.. M.M. and J.H.G. evaluated the data and dis-

cussed the results with all authors. M.M. and C.R. wrote the paper with inputs from all authors.

Competing interests

The authors declare no competing interests.

4.4 | Supplementary Information

4.4.1 | Supplementary Note 1

To evaluate the saturation magnetization of the magnetic material, we simulate Fresnel images based on micromagnetic simulations and compare the results to the measured Fresnel image in Fig. 4.4 a. We calculate the magnetic configuration in the nanostructure using the MuMax3 software package [63]. To this end, we set up a simulation in a volume of $2100 \times 2100 \times 26\,\mathrm{nm}^3$ with $512 \times 512 \times 8$ cells. We choose an exchange stiffness of $A_{\mathrm{ex}} = 1.1 \times 10^{-11}\,\mathrm{J\,m^{-1}}$ and calculate the magnetic ground state for various values of the saturation magnetization M_{S}.

Based on the magnetization integrated along the z-axis, we calculate the Aharonov-Bohm phase acquired by the electron passing through the sample [64]. This phase can be used to simulate a Fresnel micrograph via a multiplication with the contrast transfer function of the microscope in momentum space [58]. For the image simulation, we used the same imaging conditions as in Fig. 4.4 a, i.e., a defocus value of $\Delta f = 600\,\mu\mathrm{m}$ and a beam divergence of $10\,\mu\mathrm{rad}$. An electron transmission through the permalloy of 32 % was deduced from an in-focus micrograph.

Figure 4.5 shows a close-up region of the experimental Fresnel image (a), simulations for three different saturation magnetizations (b-d) and difference images (f-h). The simulated image for the entire square is shown in (e). Best agreement of experiment and simulation is obtained for $M_{\mathrm{S}} = 600\,\mathrm{kA\,m^{-1}}$, for which the residual difference (f-h) in the region of the vortex feature is at the level of the noise.

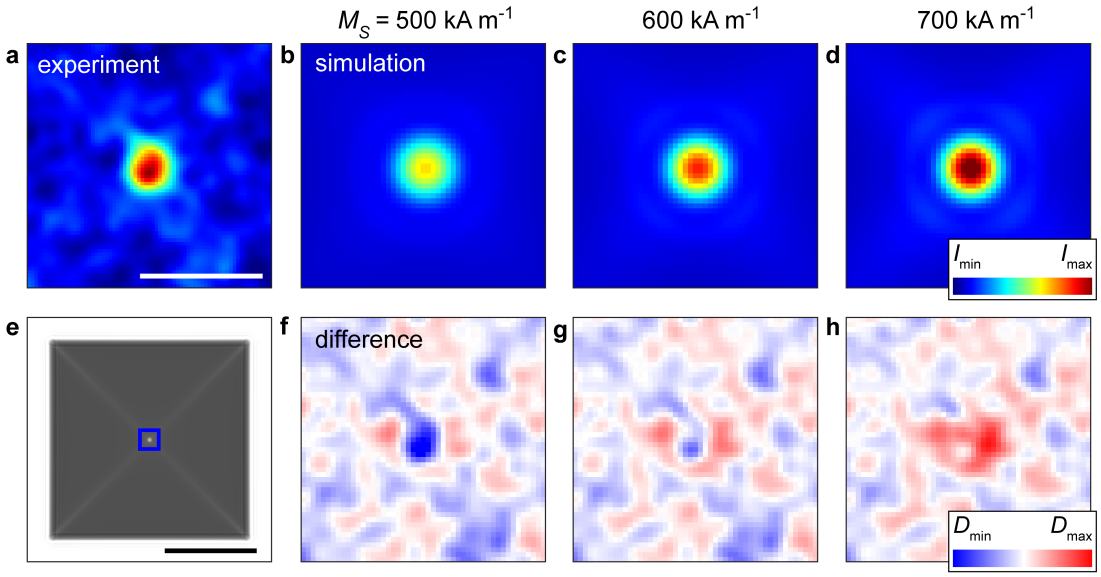

Figure 4.5: **Determination of the saturation magnetization by a comparison of simulated and experimental Fresnel images.** (a) Detailed view of the Fresnel micrograph in Fig. 4.4 a (scale bar: 100 nm). A Gaussian filter with standard deviation $\sigma = 5.8$ nm was applied. (b-d) Identical image section as in (a) for simulated Fresnel images based on micromagnetic simulations using the saturation magnetization stated above the image. (e) Total view of a simulated Fresnel image, here using the example of $M_S = 600\,\mathrm{kA\,m^{-1}}$ (scale bar: 1000 nm). Blue square corresponds to the region shown in (bd). (f-h) Difference images between the experimental micrograph and the simulated images.

5

Pinning and gyration dynamics of magnetic vortices revealed by correlative Lorentz and bright-field imaging

Marcel Möller[1,2], John H. Gaida[1,2], and Claus Ropers[1,2]

Physical Review Research **4**, 013027

[1]Max Planck Institute for Biophysical Chemistry, 37077 Göttingen, Germany.
[2]4[th] Physical Institute-Solids and Nanostructures, University of Göttingen, 37077 Göttingen, Germany.

DOI:https://doi.org/10.1103/PhysRevResearch.4.013027

Abstract

Topological magnetic textures are of great interest in various scientific and technological fields. To allow for precise control of nanoscale magnetism, it is of great importance to understand the role of intrinsic defects in the host material. Here we use conventional and time-resolved Lorentz microscopy to study the effect of grain size in polycrystalline permalloy films on the pinning and gyration orbits of vortex cores inside magnetic nanoislands. To assess static pinning, we use in-plane magnetic fields to shift the core across the island while recording its position. This enables us to produce highly accurate two-dimensional maps of pinning sites. Based on this technique, we can generate a quantitative map of the pinning potential for the core, which we identify as being governed by grain boundaries. Furthermore, we investigate the effects of pinning on the dynamic behavior of the vortex core using stroboscopic Lorentz microscopy, harnessing a new photoemission source that accelerates image acquisition by about two orders of magnitude. We find characteristic changes to the vortex gyration in the form of increased dissipation and enhanced bistability in samples with larger grains.

5.1 | Introduction

Microscopic magnetic objects such as vortices [1, 23, 118] and skyrmions [3–5] have attracted a sustained interest in the past decade. Due to their stability and unique topological properties, these textures have sparked ideas for a vast number of technological applications such as (racetrack) memories [10, 11, 191, 192], logical-gates [13, 14] and neuromorphic computing [16]. While various control schemes for the manipulation of these textures by means of external magnetic fields [29, 124], electrical currents [26, 126, 193], or optical pulses [23, 26, 194] are widely established, studies probing their interaction with defects are still highly sought after.

Previous investigations addressed the influence of artificial [132, 151, 154, 156] and intrinsic [157–160, 162, 163, 195] defects on the static pinning [132, 151, 156, 157] and the dynamics of magnetic vortices [154, 158–160, 195, 196]. A majority of these studies utilized magneto-optical microscopy [158–160, 162, 195], which helped, for example, to link pinning to surface roughness in soft magnetic samples [160]. Higher real-space resolution is offered by spin-polarized scanning tunneling microscopy in scenarios with atomic-scale defects on flat surfaces [156, 197]. This method revealed a Sombrero-shaped pinning potential between vortex cores and surface adsorbates [156]. Excellent spatial resolution for polycrystalline samples with higher surface roughness is possible using electron microscopy techniques [172] and was used to characterize core

pinning via one-dimensional differential-phase-contrast line scans [132]. Moreover, recent advances in time-resolved Lorentz microscopy enable imaging magnetic dynamics at simultaneous high spatial and temporal resolution [44, 48–50, 108, 198]. To date, however, the full capabilities of electron microscopy in both magnetic and structural imaging have yet to be leveraged in correlated studies.

In this work, we investigate the influence of the microcrystalline structure of permalloy thin films on the pinning of vortex cores by correlating the grain structure in bright-field images to the magnetic configuration in Lorentz micrographs. In order to obtain maps of pinning sites, we developed TRaPS (**T**EM **Ra**stering of **P**inning **S**ites). This procedure locates defects by laterally shifting the vortex core across a nanostructure and imaging its position with high resolution. This allows us to directly calculate a quantitative two-dimensional representation of the pinning potential. Moreover, we use time-resolved Lorentz microscopy with an improved photoemission source to assess the effect of grain size on the core gyration. We find that annealing leads to a more corrugated pinning potential and larger average distances between pinning sites. Our findings suggest preferential pinning at grain boundaries and vortex orbits that avoid particularly large grains, demonstrating the combined strengths of correlated and *in-situ* magnetic and structural characterization.

5.2 | Methods

5.2.1 | Sample System

The sample system we investigate is a magnetic vortex confined in a square permalloy ($Ni_{80}Fe_{20}$) nanoisland [1, 118]. A magnetic vortex is a flux-closure type domain configuration which is predominantly oriented in-plane and curls either counter-clockwise ($c = +1$) or clockwise ($c = -1$) around its central core. At the core region, the magnetization rotates out-of-plane and, either points up or down, said to have a polarization of $p = +1$ or $p = -1$, respectively [118].

A schematic representation of the sample is depicted in Figs. 5.1 a,b (light and scanning-electron images of the sample are in Fig. 5.11). The permalloy square has a thickness of 30 nm and an edge length of 2 µm. To electronically excite the sample, we overlap 100 nm thick gold contacts on two opposing sides of the square, which extend to wire-bonding pads. The nanoisland is positioned at the center of a $15 \times 15\,\mu m^2$ large amorphous silicon nitride window. At a thickness of 30 nm the window is near electron-transparent and is supported by a 200 µm thick silicon frame.

The sample fabrication processes involve electron-beam lithography using a positive-tone electron resist as well as electron-beam and thermal evaporation for the deposition of permalloy and gold, respectively. We take special care to remove any resist prior to metal deposition by subjecting the developed sample to a short oxygen plasma.

The contacts on either side of the microstructure allow us to excite the vortex with in-plane RF-currents, forcing its core on an elliptical trajectory [30, 92, 146]. This gyrotropic motion is a consequence of a combination of spin-transfer torques and current-induced Oersted fields [138, 146]. Generally, these systems allow for a resonance frequency between 10 MHz and 10 GHz, depending on the material and nanostructure size. For the parameters of the current sample, we expect resonance frequencies around 100 MHz [198].

To identify the effects of the nanocrystalline structure on the pinning of vortex core, we investigate one annealed sample **A** as well as two non-annealed samples **N1** and **N2**. We prepared all three samples under identical conditions on the same silicon frame. Annealing is carried out by heating a single nanostructure using a low-frequency alternating current (5 kHz, 450 mV_{rms}, 4.9 mA_{rms}, 30 min) and monitoring the progress via a resistance measurement (for further details, see Chap. 5.5.2).

5.2.2 | TRaPS

We introduce "**T**EM **Ra**stering of **P**inning **S**ites" (TRaPS) as a method to identify and locate static magnetic pinning sites using Fresnel-mode Lorentz microscopy. This imaging method is sensitive to a curl of the in-plane components of the magnetization and offers a point-resolution on the order of some tens of nanometers, depending on the imaging conditions such as defocus and source coherence [58, 183]. In order to minimize the magnetic field at the sample, for Lorentz imaging, the main objective lens is usually turned off, and a mini-lens farther from the sample is used to produce the image. For the vortex samples studied here, Fresnel imaging visually highlights the position of the four domain walls as bright lines (cf. Fig. 5.1 c). At their intersection, a peak is formed, marking the position of the vortex core. Although this peak is not a direct consequence of the out-of-plane magnetization of the core, both properties are geometrically linked. As we note below, we can localize the core with a precision far below the point resolution of the imaging technique [198]. To perform a TRaPS measurement, we shift the core across the film in a rasterized fashion using in-plane magnetic fields and record Lorentz micrographs at each raster step. A repeated occurrence of the core at the same position can then indicate the location of a pinning site.

We generate the in-plane magnetic field components H_x, H_y along the x and y direc-

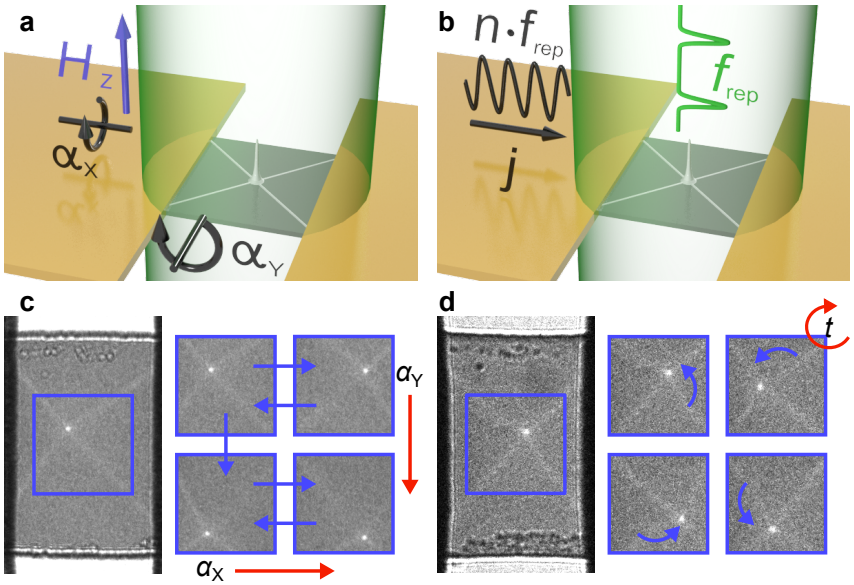

Figure 5.1: (a) Sketch of the TRaPS measurement: The magnetic nanoisland (dark grey) is illuminated with a continuous collimated electron beam (green) and subjected to an external magnetic field H_z. Tilting the sample along the two tilt axes α_x and α_y enables us to move the vortex core within the nanostructure. (b) Sketch of the time-resolved experimental setup: Here, the nanoisland is imaged using a pulsed electron beam at a repetition rate of f_{rep} and excited with a synchronized alternating current at an integer multiple of the frequency of $f_{\text{ex}} = n \cdot f_{\text{rep}}$. (c) Four micrographs illustrating the displacement of the core during a TRaPS measurement. A tilt along α_x or α_y has the same effect as applying an in-plane field H_y or H_x, respectively. (d) Example of four time-resolved Lorentz-micrographs acquired at different phases φ of the exciting current relative to the pulsed electron beam. The bright lines indicate the position of the domain walls within the nanostructure, with their intersection marking the location of the vortex core. Between frames, the core is visibly displaced and moving on a counterclockwise trajectory.

tions of the sample by applying an out-of-plane field H_z and tilting the sample along the two tilt axes α_x,α_y, as indicated in Figs. 5.1 a,c. For sufficiently small angles, the resulting field components are $(H_x, H_y) \approx H_z \cdot (\alpha_y, \alpha_x)$. We create the out-of-plane magnetic field H_z by weakly exciting the main objective lens of the microscope. This introduces a small additional defocus to the imaging system, which can easily be compensated for with the objective mini-lens.

5.2.3 | Time-resolved Lorentz microscopy

Time-resolved Lorentz microscopy is carried out at the Göttingen ultrafast transmission electron microscope (UTEM), a modified JEOL 2100F transmission electron microscope (TEM) featuring a high-brightness photoemission electron source [46, 198]. For the present study, we equipped the UTEM with a RF-generator that is electronically synchronized to the photoemission laser, using a methodology introduced in Ref. [198]. One output of the RF-generator (Keysight 81160A) feeds into a custom TEM holder that enables TEM imaging under *in-situ* current excitation with frequencies up to the GHz regime. A second output triggers the photoemission laser, a gain-switched diode laser (custom Onefive Katana 05-HP) operating at a wavelength of 532 nm. With its continuously variable repetition rate of $f_{\mathrm{rep}} = 20 - -80$ MHz and a pulse duration of 35 ps, this laser enables us to increase the electron-pulse duty cycle by more than two orders of magnitude compared to previous studies [198]. Thus, we can reduce the image acquisition time of a single stroboscopic micrograph from several minutes to a few seconds and compile much larger data sets that allow deeper insights into the vortex gyration.

We compile time-resolved movies of the vortex dynamics by exciting it at frequencies that are integer multiples of the laser repetition rate $f_{\mathrm{ex}} = n \cdot f_{\mathrm{rep}}$ and by incrementally changing the excitation phase between frames (see Fig. 5.1 b,d).

5.2.4 | Bright-field imaging and vortex core localization

To assess the nanocrystalline structure of our samples, we recorded bright-field images in low-magnification mode (Figs. 5.2 a,b) by filtering out scattered parts of the beam using an aperture. In bright-field imaging, contrast variations in a film arise from spatially varying diffraction conditions of differently oriented grains. This allows us to compare the vortex core positions we find in time-resolved and TRaPS measurements to the grain structure of the films. Therefore, we track the core in the Lorentz micrographs and map the results on top of the bright-field images. The tracking process involves calculating the center-of-mass of the pixels corresponding to the bright peak at the core position, which we identify as the largest pixel cluster above an intensity threshold. This method enables a core localization with few-nanometer precision, well below the typical point-resolution of Lorentz microscopy (usually tens of nanometers) [198]. To map the core positions onto the bright-field images, we use a geometric transformation [199], which is derived from the location of easily identifiable image features in both Lorentz and bright-field images. Using this approach, we can translate position information between both reference frames.

5.3 | Results

5.3.1 | TRaPS Measurements

TRaPS measurements are performed on the non-annealed sample **N1** and on sample **A**. In their bright-field images (Figs. 5.2 a,b), the bright and dark regions surrounding the grey permalloy nanostructure are bare silicon-nitride and the opaque gold contacts, respectively. A thin residue of permalloy, stemming from a partially coated undercut of the electron beam resist, is faintly visible at the top and bottom of the squares and can also be seen in the Lorentz images (e.g., Fig. 5.1 d). The bright-field images in Figs. 5.2 c,d reveal a significant increase in grain size in the annealed sample **A** over the non-annealed sample **N1**. This change in grain size is less significant in the vicinity of the gold contacts as these locally increase the thermal coupling, resulting in an inhomogeneous temperature profile during the annealing process.

For the TRaPS measurements, we apply an external field of $H_z = 35.8\,\mathrm{kA\,m^{-1}}$ and vary both tilt axes in a range from -2.2° to 2.2° in increments of 0.2°. This corresponds to a change in-plane field of about $620\,\mathrm{A\,m^{-1}}$ per one degree of tilt. For these small tilt angles, we do not expect a significant contribution from the out-of-plane magnetization of the vortex core to affect its localization. For comparison, in Ref. [200], a tilt from 30° to -30° shifted the peak of the Lorentz contrast at the core position by about 10 nm. Along the primary tilt direction α_x the samples are tilted back and forth once for every tilt position of the secondary axis α_y. Additionally, each sweep of α_x includes an approach step at either $\alpha_x = 3.0^\circ$ or -3.0°. Supplementary Movies 1 and 2 show, apart from the approach steps, the complete TRaPS measurements of either sample, with some example micrographs of sample **N1** presented in Fig. 5.1 c [201].

As an example, we marked the path of the core during one sweep of α_x in Figs. 5.2 c,d, where we see that the core does not move in straight lines but rather zigzags and occasionally gets trapped. All tracked positions are marked with dots in Figs. 5.2 e,f where they are plotted on top of the bright-field image of the corresponding region. An alternative depiction of the data is provided in Fig. 5.12, with the dots color-coded as a function of tilt angle α_y. Due to the small size of the grains in sample **N1**, there is no apparent visual correspondence between the nanocrystalline structure and the core positions (Fig. 5.2 e). However, we cannot exclude possible correlations on length scales smaller than those resolved in the bright field images.

As for the annealed sample **A**, we find numerous pinning sites located directly at boundaries of larger grains (see arrows Fig. 5.2 f). Furthermore, it stands out that the core never resides within one of the large grains. An in-depth analysis of the image

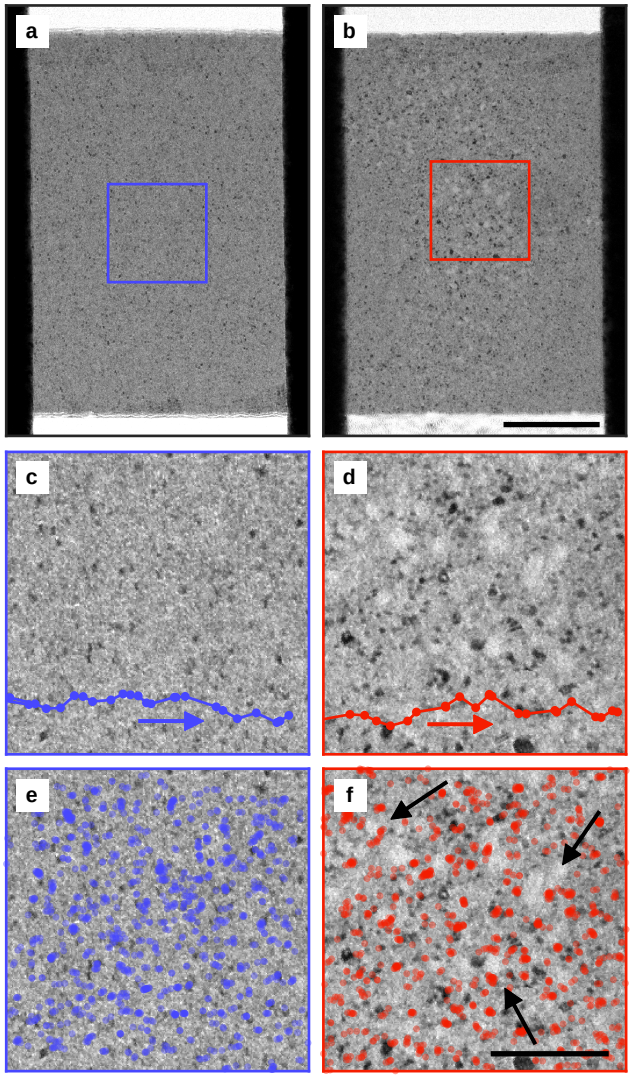

Figure 5.2: Bright field images of the non-annealed sample **N1** (a) and the annealed sample **A** (b). (c,d) Close-ups of the regions marked in (a) and (b). The annealed sample shows a drastically increased grain size in the depicted area. The lines indicate the path of the vortex core during an exemplary tilt of primary tilt axis α_x, while α_y is kept constant. (e,f) Tracked vortex core positions overlaid on top of the bright-field images in (c) and (d). A single tracked position is plotted with a partial transparency, such that if the core is encountered at the same location repeatedly, the superimposed dots appear more saturated and opaque. An alternative depiction of the data in (e,f) is given in Fig. 5.12 indicating the angle of the slow tilt axis α_y.

intensities at the core positions is given in Chap. 5.5.3 and confirms these findings. For sample **A** the analysis shows that the core rather resides at intermediate image intensi-

ties found outside of dark or bright grains. Together, these observations clearly demonstrate that grain boundaries can pin vortex cores in polycrystalline films. While this behavior was suspected before [162], it has, to our knowledge, never been directly observed. Interestingly, however, we can not find direct evidence for a movement of the vortex core along large domain boundaries. This indicates that grain boundaries rather serve as a necessary than a sufficient condition for pinning, suggesting additional contributions to the final position of the pinning site.

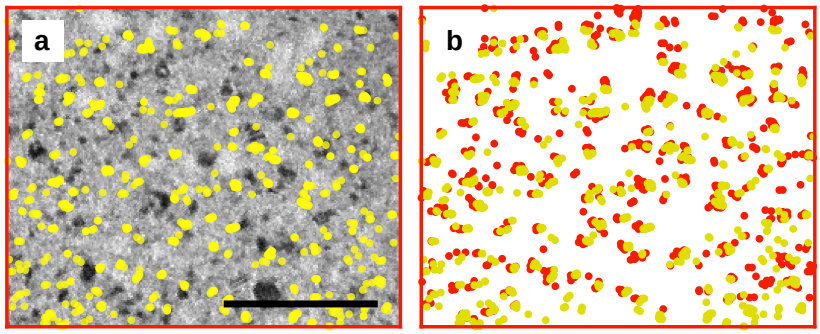

Figure 5.3: Comparison between TRaPS measurement on sample **A** with clockwise curl $c = -1$ and underfocus imaging conditions (red dots) and counter-clockwise curl $c = +1$ and overfocus imaging conditions (yellow dots). (a) Tracked vortex core position overlaid onto bright-field image of sample **A**. (b) Depiction of the tracked vortex position of both measurements in the reference frame of the bright-field image in (a). Both datasets are in good agreement with each other, with only a minor offset between the two. The difference in the overall center of both TRaPS measurements can be explained with a residual magnetic in-plane field at the sample position (see text).

To assess the accuracy of our measurement technique, we repeat the tracking and the transform calculation for a second set of experimental conditions on sample **A**. The results presented in Fig. 5.2 d are acquired with a clockwise curl ($c = -1$), necessitating underfocused imaging conditions to achieve a bright spot at the core position [117]. For the second measurement, we simultaneously alter the domain state to a counter-clockwise curl ($c = +1$), and employ overfocused imaging conditions. This serves two purposes: Firstly, the magnetic image contrast will again appear bright, which is necessary for the core tracking algorithm to work properly [117]. Secondly, the electrostatic contributions in the Lorentz image will significantly change. Therefore, the process of correlating the Lorentz to the bright-field micrographs has to be repeated completely independently from the first data set, whose accuracy can thus be verified. The results for the second set of tracking data are shown in Fig. 5.3 a, and are in excellent agreement with the previous results. This is particularly evident when we plot both data sets to-

gether in the same reference frame as in Fig. 5.3 b, where the only discernible difference is a minor lateral displacement of about 6 nm. In addition to confirming that TRaPS allows for accurate localization of pinning sites, this comparison also demonstrates that the underlying process is independent of the vortex curl.

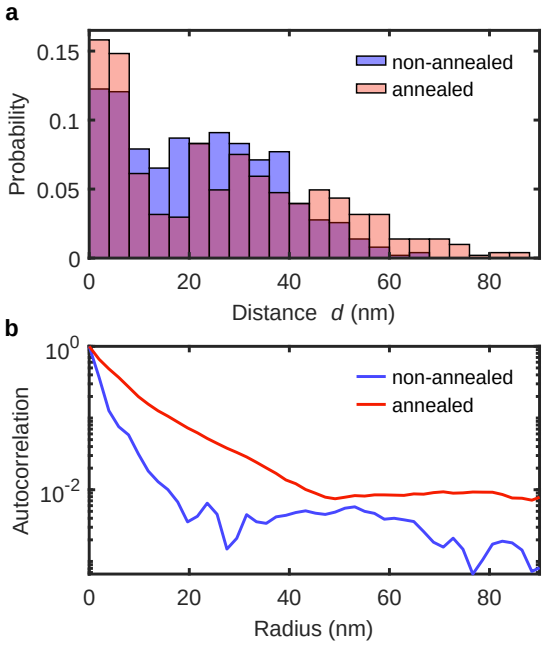

Figure 5.4: (a) Probability that the vortex core moved by distance d between two TRaPS steps. (b) Radial autocorrelation of the bright field images displayed in Fig. 5.2 c,d.

To further analyze our data, we calculate the distance d traveled by the vortex between two consecutive steps of a TRaPS scan. Fig. 5.4 a shows histograms of the jump distances for both samples (the initialization steps at $\alpha_x = \pm 3°$ are not included in these statistics). The most prominent feature in both distributions is a strong peak at small distances $d < 8$ nm. For these distances, we can assume that the vortex has remained at the same pinning site, and as we would expect, this happens more frequently for sample **A**. In contrast, we identify substantial differences between both samples for distances $d > 8$ nm: Firstly, the vortex in the annealed sample rarely moves by distances in the range of 8 nm to 20 nm, and secondly, it more frequently jumps over longer distances beyond 40 nm, which evidently is a result of larger grain sizes.

For comparison, we also compute the average grain size in both samples using the

full-width-half-maximum of the radial autocorrelation function[1] [202, 203]. From the autocorrelation functions in Fig. 5.4 b we estimate grain sizes of 4 nm and 10 nm for sample **N1** and **A**, respectively. This demonstrates that the typical jump distances span up to several grain diameters, suggesting that not every grain boundary causes effective pinning.

5.3.2 | Quantifying the Pinning Potential

In the following, we will detail how, based on our TRaPS data, we can quantitatively assess the pinning potential in our samples. To this end, we choose a simplistic approach to obtain a two-dimensional representation of the potential as a whole (instead of treating each pinning site individually). As illustrated in Fig. 5.5a, we assume that each core position $\left(X_{i,\mathrm{exp}}, Y_{i,\mathrm{exp}}\right)$ (grey) measured at every individual step of the TRaPS measurement i contributes to the potential with an identical Gaussian dip (depth: E_{pin}, width: σ_{pin}) [156, 157, 162, 195]. The overall pinning potential is then given by the sum of all Gaussians, ensuring a deeper and/or broader potential in regions where the core is encountered more frequently, and reads

$$E_{\mathrm{pin,all}} = -E_{\mathrm{pin}} \sum_i \exp\left(-\frac{r_i^2}{2\sigma_{\mathrm{pin}}^2}\right) , \tag{5.1}$$

where $r_i^2 = \left(X - X_{i,\mathrm{exp}}\right)^2 + \left(Y - Y_{i,\mathrm{exp}}\right)^2$ is the squared distance to the core position measured at tilt step i.

Under these assumptions, the pinning potential results directly from the TRaPS measurement and the two values E_{pin} and σ_{pin}, which are to be determined in the following. To compare different choices of E_{pin} and σ_{pin}, we perform multiple TRaPS simulations based on $E_{\mathrm{pin,all}}$ and choose the value tuple which best reproduces the experimental data.

During a single TRaPS simulation, we replicate how the core is trapped and moves between pinning sites by scanning a quadratic potential across $E_{\mathrm{pin,all}}$. We derive the quadratic potential from the rigid vortex model [131], for which the energy of the vortex domain configuration is expressed in terms of the core position (X, Y) and the external magnetic field

$$E_{\mathrm{quad}} = \frac{1}{2}k(X^2 + Y^2) + ck\chi\left(-H_x Y + H_y X\right) . \tag{5.2}$$

[1] It is worth noting that dark-field images were used for this assessment in the original publications. However, we believe that for a rough estimate, we are interested here, bright-field images are equally suitable.

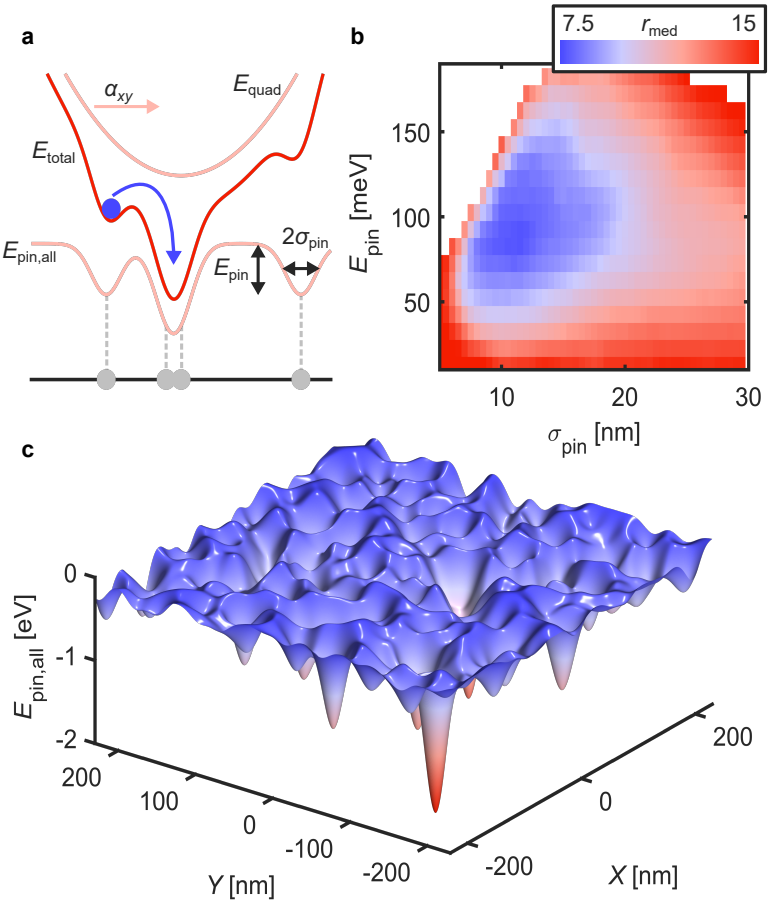

Figure 5.5: Reconstruction of the pinning potential from TRaPS data of sample **N1**. (a) Illustration of model potential E_{total} used for the simulated TRaPS data. E_{quad} is a quadratic plus a field-dependent linear potential (here, as a function of the tilt angle $\alpha_{x,y}$) that defines the equilibrium position of the vortex core in the absence of any pinning. $E_{\text{pin,all}}$ is composed of a Gaussian potential for each experimentally measured pinning position (grey dots), all having the same depth E_{pin} and width σ_{pin}. By increasing/decreasing the tilt angle, the vortex core is dragged along and probes the pinning potential. (b) Median radial deviation r_{med} between the experimental and simulated TRaPS data for various combinations of E_{pin} and width σ_{pin}. The best agreement is obtained at $r_{\text{med}} = 7.6\,\text{nm}$ with $E_{\text{pin}} = 80\,\text{meV}$ and $\sigma_{\text{pin}} = 11\,\text{nm}$. Values of E_{pin} and σ_{pin} which do not improve r_{med}, compared to a case of no pinning potential, are left blank. (c) 2D representation of the pinning potential $E_{\text{pin,all}}$ for $E_{\text{pin}} = 80\,\text{meV}$ and $\sigma_{\text{pin}} = 11\,\text{nm}$.

Here, k is the stiffness factor of the quadratic potential, and χ is the displacement susceptibility. For our sample geometry, we calculate a stiffness factor of $k = 1.63 \times 10^{-3}\,\mathrm{eV\,nm^{-2}}$ using micromagnetic simulations [63]. This simulation is performed with a $512 \times 512 \times 4$ cell geometry, an exchange coupling of $A_{\mathrm{ex}} = 1.11 \times 10^{-11}\,\mathrm{J\,m^{-1}}$ [204], and a saturation magnetization[2] of $M_{\mathrm{S}} = 440\,\mathrm{kA\,m^{-1}}$.

The equilibrium core position in the absence of pinning, i.e., the minimum of E_{quad}, is given by

$$\begin{pmatrix} X \\ Y \end{pmatrix} = c\chi \begin{pmatrix} -H_y \\ H_x \end{pmatrix} = c \underbrace{\chi H_z}_{=:\tilde{\chi}} \begin{pmatrix} -\alpha_x \\ \alpha_y \end{pmatrix} . \tag{5.3}$$

Here, we replace χ with a modified displacement susceptibility $\tilde{\chi} = \chi H_z$, which specifies the core movement per tilt angle. By fitting Eq. 5.3 to our data, we find $\tilde{\chi}$ to be $98\,\mathrm{nm}/^\circ$ and $108\,\mathrm{nm}/^\circ$ for sample **N1** and **A**, respectively. It is worth noting that the effects of the short-range pinning sites are negligible for the overall core displacement used in this fit. The results are in good agreement with the micromagnetic simulation, which predicted a value of $\tilde{\chi} = 123\,\mathrm{nm}/^\circ$.

A single TRaPS simulation is fed with the same sequence of tilt angles as in the experiment. At each tilt step i, we find the next local minimum $(X_{i,\mathrm{sim}}, Y_{i,\mathrm{sim}})$ of $E_{\mathrm{total}} = E_{\mathrm{quad}} + E_{\mathrm{pin,all}}$ in the direction of the steepest descent. This is done using a numerical gradient descent minimization, where we supply the algebraic form of the gradient and the Hessian matrix of E_{total} for maximum robustness. The starting point of each minimization is the simulated minimum from the previous tilt step $i-1$, just like in the experiment. The result of a TRaPS simulation is a set of simulated core positions $(X_{i,\mathrm{sim}}, Y_{i,\mathrm{sim}})$, which we can compare to the experimental data using the median radial deviation

$$r_{\mathrm{med}} = \mathrm{median}_i \left(\left\| \begin{matrix} X_{i,\mathrm{sim}} - X_{i,\mathrm{exp}} \\ Y_{i,\mathrm{sim}} - Y_{i,\mathrm{exp}} \end{matrix} \right\| \right) . \tag{5.4}$$

Figure 5.5 b shows the median radial deviation for all TRaPS simulations based on the data of sample **N1**. The values of $E_{\mathrm{pin}} = 80\,\mathrm{meV}$ and $\sigma_{\mathrm{pin}} = 11\,\mathrm{nm}$ best reproduce the experimental data, in that they result in the smallest value of r_{med}. In case of sample **A**, we obtain similar values of $E_{\mathrm{pin}} = 90\,\mathrm{meV}$ and $\sigma_{\mathrm{pin}} = 12\,\mathrm{nm}$, which results in an increase of the integrated pinning potential of about 30 %. The simulated core positions

[2]The value of M_{S} was obtained from a comparison of experimental and simulated Lorentz images, using the nominal film thickness of 30 nm. It is somewhat lower than expected from bulk values, which might be caused by uncertainty in the determination of the film thickness. Furthermore, it is worth noting that we found k to be virtually unchanged under an applied field H_z unlike the free gyration frequency, which is a function of the field [205].

are in good agreement with experimental data, as we present in Fig. 5.15, together with images of the pinning potential.

A three-dimensional representation of $E_{\mathrm{pin,all}}$ of sample **N1** is given in Fig. 5.5 c. It has a roughness, estimated by the standard deviation of the potential, of 193 meV and measures -2.0 eV at its deepest point. For the annealed sample, the respective values are 281 meV and -2.4 eV. This analysis demonstrates that polycrystalline samples with larger grains show an overall increase in their pinning potential, with an increased roughness and deeper minima. Furthermore, we note that the demonstrated method is capable of quantifying pinning potentials down to sub-100 meV and spanning multiple orders of magnitude.

5.3.3 | Time-resolved Trajectories

Besides studying the static interaction of the vortex core with pinning sites, we also probed how the dynamic vortex gyration is affected by the nanocrystalline configuration. We, therefore, perform time-resolved measurements on the non-annealed sample **N2** and the annealed sample **A**, where we excite the permalloy square with an alternating current forcing the vortex core on an elliptical trajectory. We recorded this motion in sample **N2** for excitation frequencies from $f_{\mathrm{ex}} = 86$ MHz to 99.5 MHz at a current density of $j = 3.6 \times 10^{10}\,\mathrm{A_{rms}\,m^{-2}}$ and in case of sample **A** for frequencies from 72 MHz to 84 MHz at $j = 8.2 \times 10^{10}\,\mathrm{A_{rms}\,m^{-2}}$. The higher currents and lower frequencies in the case of sample **A** were only necessary after annealing, whereas before, we were able to observe core gyration at similar excitation parameters as for sample **N2**. To measure and ensure a constant excitation current throughout the frequency range, we monitor the sample current I_{S} using an oscilloscope (for details, see Chap. 5.5.1).

At each frequency, we record up to 60 micrographs and incrementally increase the phase between the RF-current and the probing electron beam to cover the whole excitation period. These micrographs are combined into Supp. Movies 4 and 5, and show the time-resolved gyration together with the tracked core positions [201]. Figures 5.6 a,b show a compilation of all trajectories overlaid on the bright-field images (individual depictions in Figs. 5.13 and 5.14).

Similar to our TRaPS measurements, we can also identify grains in the annealed sample in Fig. 5.6 b that appear to be avoided by the core, however, less conclusively as in the static case. We marked two of these grains with arrows in Fig. 5.6 b. Furthermore, we find discontinuous jumps of the vortex position upon cycling the excitation phase, where it appears to switch between two or more equally favorable trajectories. The fact that our stroboscopic method can resolve a single vortex core before and after

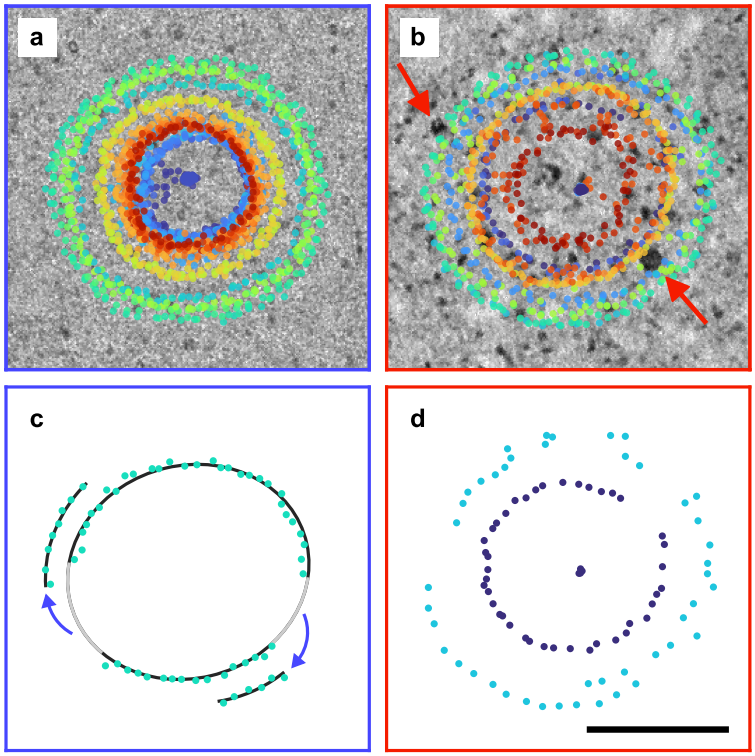

Figure 5.6: (a,b) Trajectories (dots) of the vortex gyration in sample **N2** (a) and sample **A** (b) measured via time-resolved Lorentz microscopy overlaid on top of bright-field images of samples. (c) Example of a segmented trajectory in (a) indicating a bistable gyration. The black line is a guide to the eye, indicating the movement of the core. The greyed-out path and the arrows indicate where the core jumped to another equally favorable orbit. (d) Two examples for jagged trajectories in (b).

a jump indicates that these do not happen randomly during an image acquisition but rather in between. This suggests the phase discontinuity upon a parameter change (excitation frequency or phase) as a cause for such events. Interestingly, this behavior is encountered much more regularly for the annealed sample, both at a larger number of frequencies and during a measurement at a given frequency (see Figs. 5.13 and 5.14). This multistability can be considered the dynamic counterpart of stochastic switching between bistable static pinning sites [157, 163, 206].

To further evaluate the trajectories, we fit them to an ellipse and determine the mean of both semiaxes r [207]. Figure 5.7 shows the resulting radii r divided by the sample current I_S and plotted against the normalized frequency f_{ex}/f_r. The graphs reveal a resonance frequency of the gyration of $f_r = 90.5\,\mathrm{MHz}$ and 76 MHz for sample **N2** and **A**,

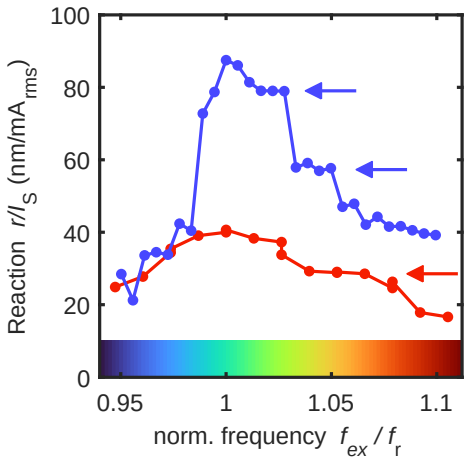

Figure 5.7: Excitation-current-normalized radius r/I_S as a function of normalized frequency f_{ex}/f_r. For some frequency ranges the orbit radius stays constant upon changing the excitation frequency (arrows).

respectively[3]. Here, two observations stand out. First, the radius of the trajectories does not change continuously in size as a function of frequency f_{ex} (see also Refs. [92, 198]), suggesting hysteretic behavior. Instead, we find plateaus, for which trajectories cluster at certain radii (marked with arrows in Fig. 5.7), clearly indicating an orbital stabilization by the pinning potential. Secondly, we find that the current-normalized radius r/I_S is significantly smaller and exhibits a broader resonance in the case of the annealed sample **A**, which is a distinct sign of enhanced dissipation in this sample. Such enhanced dissipation can be attributed to the excitation of additional internal degrees of freedom of the vortex configuration due to the presence of defects [166]. These two observations, together with enhanced multistability in the annealed sample, demonstrate that grain sizes have an important influence on the dynamic behavior of gyrating vortices.

5.4 | Conclusion

Nanocrystallinity and surface roughness have long been linked to the pinning of vortices in soft-magnetic films [132, 160, 162]. The direct real-space identification of grain boundaries as effective pinning sites for the core was enabled by the TRaPS method introduced in this study. The correlation of structural and magnetic imaging in electron

[3]Note that the lack of a significant ellipticity in the studied frequency range agrees with expectations based on Ref. [137].

microscopy can be further developed to trace the microscopic origins of pinning down to the atomic scale, combining high-resolution (scanning) TEM with holography [174, 175] or differential phase contrast [40, 172].

The joint high spatial and temporal resolution of our approach will be critical to explore transient pinning and local damping effects, while the quantitative TRaPS potential will serve as input for future theoretical studies on driven vortex dynamics. The global ansatz for the calculation of the trapping potential based on common properties of pinning sites may be further refined by taking into consideration characteristics of individual defects. The observation of increased roughness, deeper traps, and enhanced bistability for samples with larger grains may become relevant for device fabrication and in the tailoring of annealing processes to mitigate or selectively enhance pinning.

Finally, on the methodological side, the two orders of magnitude increase in time-averaged brightness of the photoemission source will have immediate benefits in picosecond stroboscopic imaging of ultrafast dynamics also beyond magnetism, including nanoscale structural and electronic phenomena.

Acknowledgement

This work was funded by the Deutsche Forschungsgemeinschaft (DFG) in the Collaborative Research Center "Atomic Scale Control of Energy Conversion" (DFG-SFB 1073, project A05) and via resources from the Gottfried Wilhelm Leibniz-Prize. We gratefully acknowledge support by the Lower Saxony Ministry of Science and Culture and funding of the instrumentation by the DFG and VolkswagenStiftung. Furthermore, we acknowledge helpful discussions and assistance from the Göttingen UTEM Team, especially Thomas Danz, Till Domröse, Armin Feist and Karin Ahlborn.

Author contributions

C.R. and M.M. conceived the project. M.M. prepared the sample. M.M. and J.H.G. conducted the experiment. M.M. evaluated the data and discussed the results with J.H.G. and C.R. M.M. and C.R. wrote the paper with inputs from J.H.G.

5.5 | Supplementary Information

5.5.1 | Supplementary Note 1: Electrical setup and corrections

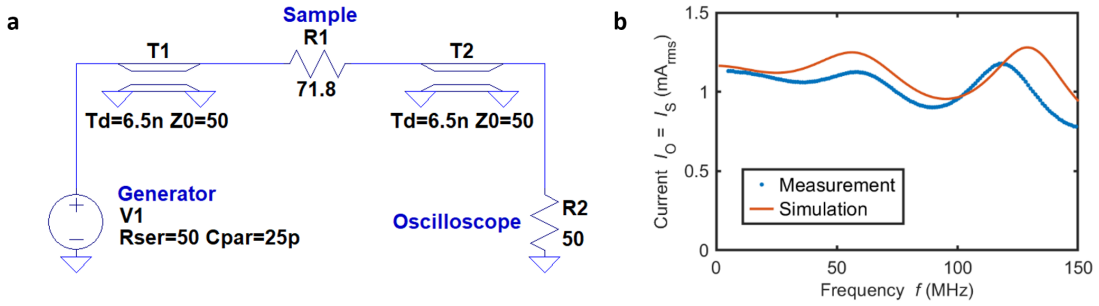

Figure 5.8: **Electrical setup for the time-resolved measurement.** (a) Circuit diagram of the electrical setup consisting of a voltage source ($V_1 = V_G$) with a series resistance (R_{ser}) and a parallel capacitance (C_{par}), two 50 Ω transmission lines with a length of 6.5 ns (T1, T2) as well as a resistor for the sample ($R_1 = R_S$) and the oscilloscope (R_2). (b) Current I_S flowing through the sample as a function of excitation frequency f_{ex} at a generator voltage $V_G = 100\,mV_{rms}$. The blue dots represent data obtained for sample **A**, whereas the red line stems from a frequency-domain simulation of the circuit in (a).

A circuit diagram of the electrical setup we use in the time-resolved measurement is given in Fig. 5.8 a. In the experiment, the sample is connected in series between a Keysight 81160 generator (350 MHz bandwidth) and a Tektronix DPO71604C oscilloscope (16 GHz bandwidth) via two identical coaxial cables to both sides of the sample.

5.5.1.1 | Determining the sample resistance

At low frequencies (DC to kHz-range) this setup can be viewed as a voltage source with three resistors in series, i.e. the 50 Ω resistors of the generator and the oscilloscope and the sample itself. Knowing the voltage V_O at the oscilloscope and the generator output voltage V_G, we can calculate the sample resistance via:

$$R_S = 2 \cdot 50\,\Omega \cdot \frac{V_G - V_O}{V_O} \,. \tag{5.5}$$

Please note, that here V_G refers to the voltage that is set at the front panel of the generator. This corresponds to half the voltage that is applied across the whole circuit, since usually half of the total voltage is dropped at the generator's internal termination and the other half across a matched 50 Ω load. We measure the exemplary value of $R_{S,A} = 71.8\,\Omega$ in Fig. 5.8 a on sample **A** at $V_G = 100\,mV_{rms}$ and $f_{ex} = 5\,kHz$.

5.5.1.2 | Correcting for standing waves

At higher frequencies, a small impedance mismatch at the output of the generator and a larger mismatch at the sample results in a standing wave between these components. If we were to operate the generator at a constant output voltage, the current I_S passing through the sample would vary with the excitation frequency f_{ex}. Since the high-bandwidth input of the oscilloscope shows virtually no reflections in the spectral range used here, there are no standing waves between the sample and the oscilloscope and therefore I_S is equal to current I_O into the oscilloscope ($I_S = I_O$). For the time-resolved measurements we generate a look-up table that adapts the generator output voltage V_G such that I_O – and consequently I_S – is kept constant, while sweeping the frequency. To set up this table, we measure $I_O = 50\,\Omega \cdot V_O$ as a function of frequency, where V_O is the voltage measured at the oscilloscope. Figure 5.8 b presents an example of such a measurement. The data was recorded on sample **A** at $V_G = 100\,\mathrm{mV_{rms}}$. Simulating the circuit in Fig. 5.8 a using LTSpice® XVII[4] reproduces the data obtained from the measurement quite well. The only free parameter in the model is the parasitic capacitance of the generator output. The lengths of the cables were measured using time-domain reflectometry. The good agreement of measurement and simulation shows that our assumptions on the circuit are justified.

5.5.2 | Supplementary Note 2: Annealing and Joule Heating

The time-resolved trajectories presented in the main text were measured at two types of samples. Sample **A** has been annealed at a high current ($V_G = 450\,\mathrm{mV_{rms}}$) for 30 min prior to the time-resolved measurement, while great care has been taken to prevent any amount of annealing for sample **N2**. Before and after the annealing we measure the sample current I_S at various generator voltages V_G. From this data we derive the sample resistance R_S using the equation given in Chap. 5.5.1. The results of this measurements are plotted in Fig. 5.9 a,b and show two distinct features: Most prominent is a substantial reduction in sample resistance as a direct consequence of the annealing process. Secondly, we can identify a transient increase in sample resistance at high currents, which is due to a temperature rise caused by Joule heating. In case of the non-annealed sample, we only allowed for currents below a threshold of non-reversible resistance changes, making sure its grain structure was not altered. The time-resolved measurements have been conducted at currents of $I_S = 4.9\,\mathrm{mA_{rms}}$ and $I_S = 2.2\,\mathrm{mA_{rms}}$ for sample **A** and sample **N2**, respectively. Because of the heat generated by these cur-

[4] LTSpice® is a registered trademark of ANALOG DEVICES, Inc.

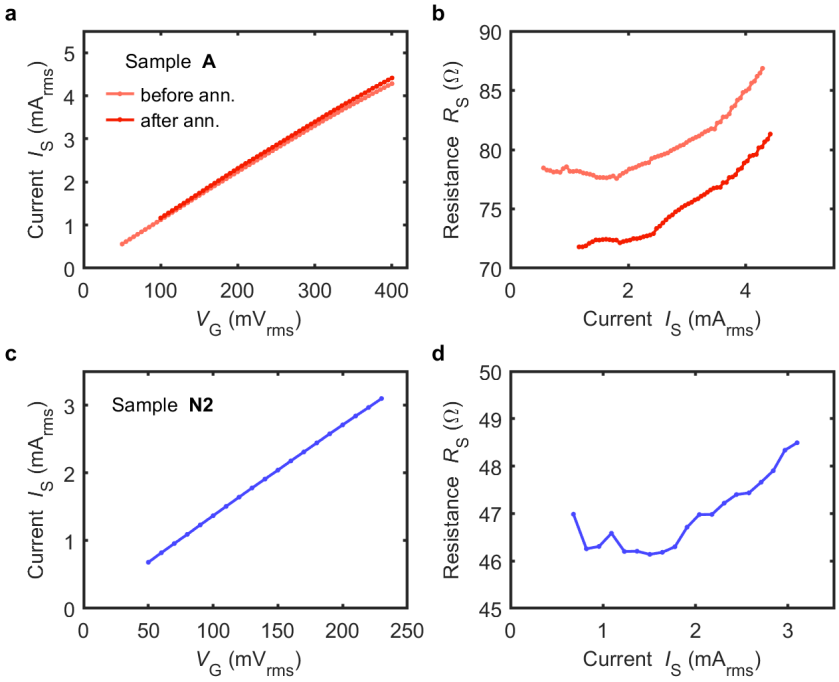

Figure 5.9: Sample current I_S as a function of the generator output voltage V_G and resulting sample resistance R_S for annealed sample **A** (a,b) and non-annealed sample **N2** (c,d). The resistance of sample **A** decreases after annealing, indicating an increase in grain size. For sample **N2** we take special care not to exceed a current threshold that would alter the resistance.

rents, we found a respective drop in the saturation magnetization of 30 % and 10 % with respect to the room-temperature value of about 440 A m^{-1}. These values were derived from Lorentz micrographs of the heated and unheated samples in comparison to simulated Lorentz images. The simulated images were generated using a combination of micro-magnetic [63] and Lorentz image simulation [58]. Details on the technique are discussed in the Chap. 4.4.

5.5.3 | Supplementary Note 3: Correlating image contrast and pinned vortex core positions

In this note, we show that – based on our TRaPS data of sample A – the vortex core is rather pinned at grain boundaries than inside grains. This analysis is based on the fact that grains in bright-field images are identified by either high or low image intensities. Fig. 5.10 displays a histogram of the bright-field image of the annealed sample A presented in Fig. 5.2 d in the main text. The dark gray bars indicate the distribution of

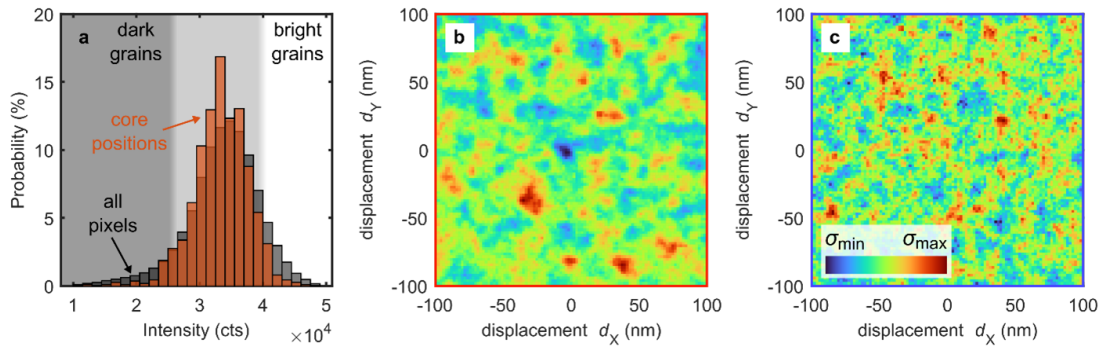

Figure 5.10: Demonstration of a correlation between vortex core positions and intermediate gray values in the bright-field image of sample **A**. (a) Distribution of the image intensity of the bright-field image in Fig. 2d: (gray boxes) all pixels in Fig. 2d. (red boxes) pixels where the core was found in the TRaPS measurement. The narrower distribution of the core- position-pixels indicates that the core rather resides outside of grains. (b) Standard deviation of the intensity distribution of core-position pixels, if the TRaPS data is displaced by (d_X, d_Y). The distribution is minimally dispersed only for displacements around zero. (c) Standard deviation of the intensity distribution of core-position pixels for sample **N1**. Here, we find no correlation between the image intensity and core positions.

the image intensity of all pixels. This distribution has a width, measured by the standard deviation, of $\sigma_{BF} = 5.70 \times 10^3$cts, and significant foothills at high and low values (marked with bright and dark backgrounds). In contrast to that, the red bars show the image intensities found at the tracked vortex core positions (red dots in Fig. 5.2 d). This chart is narrower ($\sigma_{\mathrm{TRaPS}} = 4.26 \times 10^3$cts) with no foothills, which indicates that the core does not reside inside grains. To demonstrate that this is not a coincidental observation we investigate how the width of the distribution evolves if we displace the tracked core positions above the bright-field image. Specifically, we add a displacement vector (d_X, d_Y) to the TRaPS data and recalculate the standard deviation $\sigma_{\mathrm{TRaPS}}^{(d_X,d_Y)}$ for the resulting intensity distribution. If we repeat this process for various (d_X, d_Y) we obtain Fig. 5.10 b. In this figure, we see that the width $\sigma_{\mathrm{TRaPS}}^{(d_X,d_Y)}$ is minimal only for small displacements around zero. This directly indicates a correlation between the measured core positions and intermediate gray values in the bright-field image. We, therefore, conclude that our measurements reveal a vortex core pinning at grain boundaries in the annealed sample A. An identical evaluation based on the TRaPS and bright-field data of the non-annealed sample N1 does not show such a correlation (cf. Fig. 5.10 c). This is in line with the observations based on visual inspection stated in the main text. As we discussed there, this does not mean that no such correlation can exist, since the resolution

of our bright-field image can limit our observations.

5.5.4 | Supplementary Figures

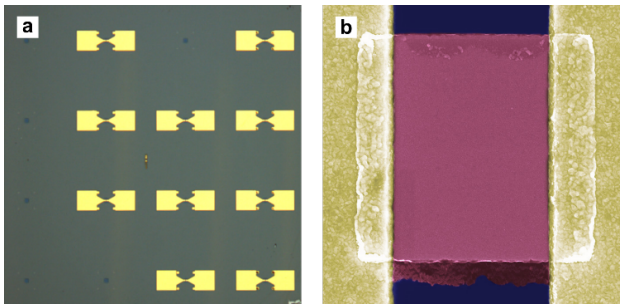

Figure 5.11: Sample system: (a) Light microscope image of a sample frame with 16 silicon nitride windows (small blue squares). The bow-tie-like structures comprise the wire-bonding pads on their sides and taper towards their center, contacting the magnetic microstructure. (b) False-colored scanning electron micrograph sample A. The permalloy square (red) is contacted with cold contacts (yellow) and rests on an amorphous silicon nitride membrane (blue). The micrograph was acquired with an acceleration voltage of 10 kV using an in-lens detector.

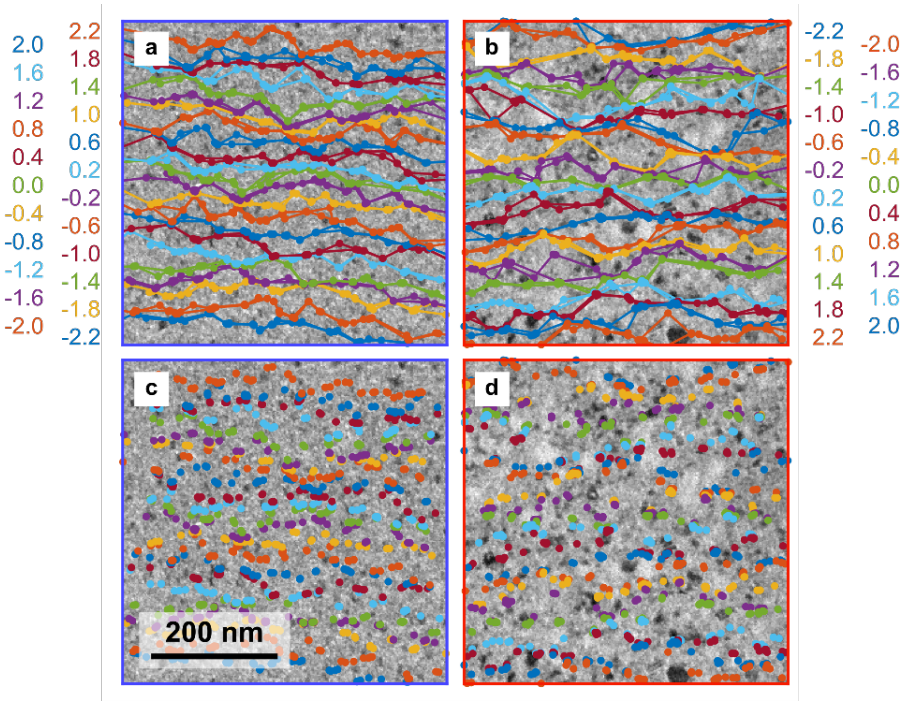

Figure 5.12: TRaPS data visualized as a function of the slow tilt angle α_y. Both sweep directions of α_x are plotted with the same color. The fast sweep direction α_x The lines in (a,b) are guides to the eye.

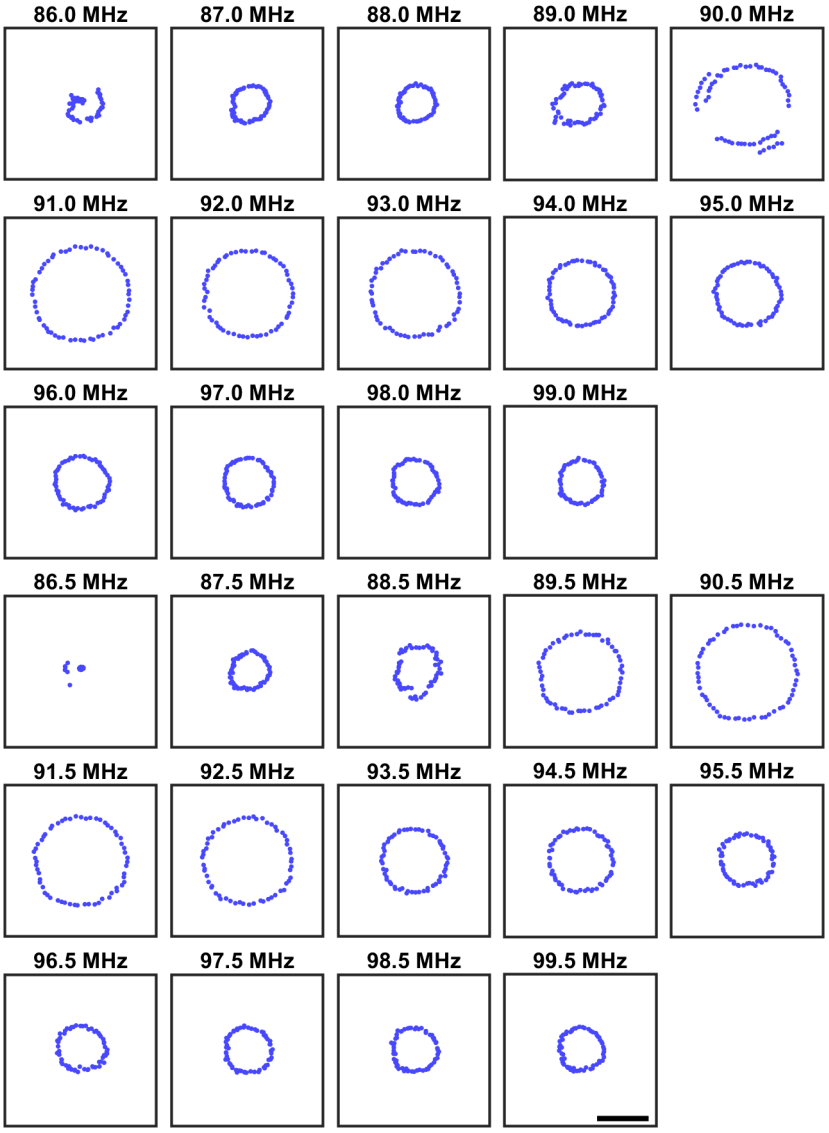

Figure 5.13: Vortex core orbits of non-annealed sample **N2** measured using time-resolved Lorentz microscopy sorted in measurement order (scalebar: 200 nm). For trajectories (e.g., at 90 MHz) appear to be bistable.

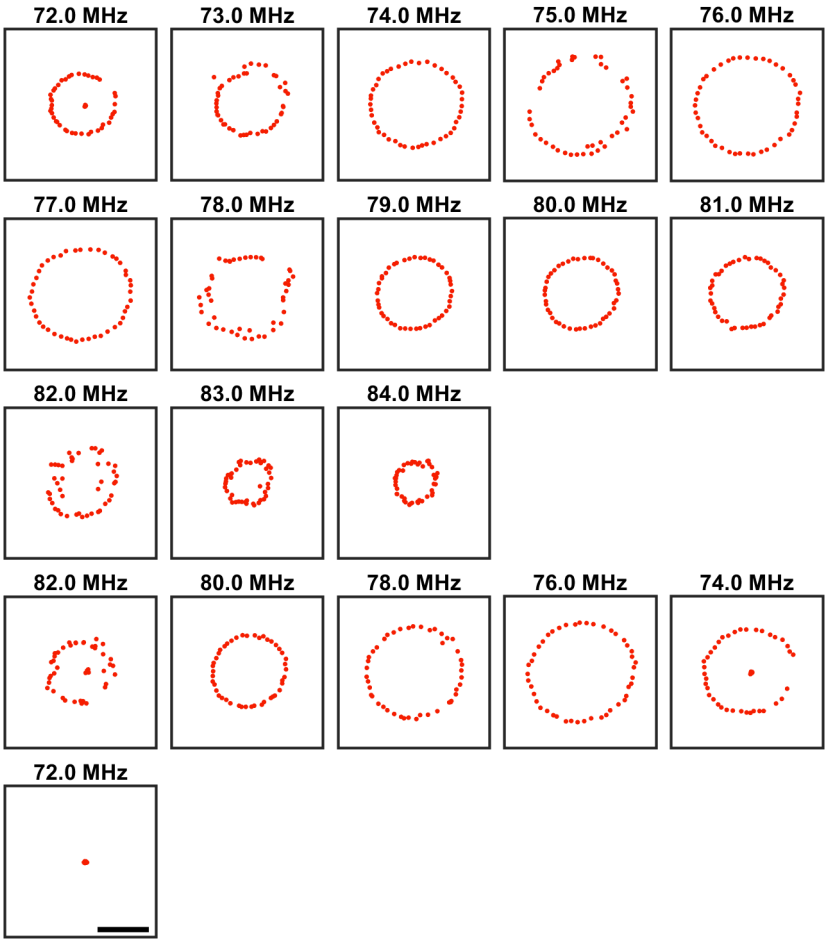

Figure 5.14: Vortex core orbits of non-annealed sample **A** measured using time-resolved Lorentz microscopy sorted in measurement order (scalebar: 200 nm). The number of bistable trajectories is higher than for sample **N2** (see Fig. 5.13).

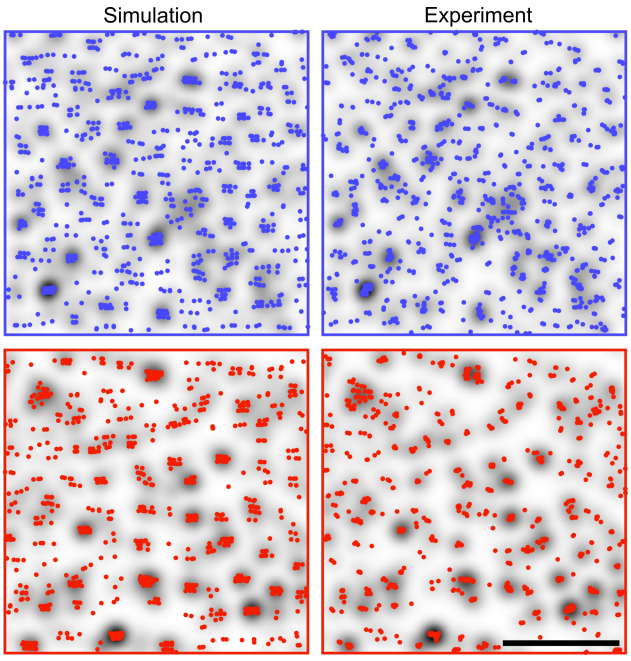

Figure 5.15: Comparison between simulated and experimental TRaPS data for samples **N2** (blue) and **A** (red). The simulated data as well as the underlaid potential (grey) shown here, correspond to the choice of E_{pin} and σ_{pin} which minimizes the median radial deviation for the respective sample (scalebar: 200 nm).

6

Summary and Outlook

Insights into the interaction of magnetic textures with defects intrinsic to polycrystalline films are highly sought-after, especially in the technologically relevant field of current-driven magnetization dynamics [132, 160, 162, 166]. With this thesis, I presented two publications (Chaps. 4 and 5) which represent a significant advance in the field of time-resolved imaging of magnetic dynamics and in the probing of disorder in vortex nanostructures.

In the first paper, I and my coworkers demonstrated the feasibility of time-resolved Lorentz microscopy for the investigation of current-driven magnetization dynamics by studying the spin-transfer torque-driven gyration of a magnetic vortex confined in a permalloy nanostructure. The core achievements of this work are:

- the implementation of time-resolved Lorentz microscopy with radio-frequency current excitation with $< 3\,\mathrm{ps}$ short electron pulses and a point resolution $< 55\,\mathrm{nm}$,
- the demonstration of $\pm 2\,\mathrm{nm}$ vortex core localization precision at few-minute image integration times under said experimental conditions,
- and the identification of a transient change in the frequency and damping of a decaying vortex gyration attributed to disorder in the sample.

This work is continued with the second publication in Chap. 5, where the static and dynamic pinning of magnetic vortices in films of varying grain sizes is studied. The main advances of this work are:

- a reduction in acquisition time of time-resolved Lorentz micrographs by multiple orders of magnitude with the implementation of a new photoemission source,

- the development of "TEM rastering of pinning sites" (TRaPS), a TEM-based technique to locate static pinning centers in vortex nanostructures with a sub-100 meV pinning potential,
- the design of an algorithm to reconstruct the quantitative two-dimensional pinning potential from TRaPS data,
- correlating the time-resolved vortex gyration and data on static pinning provided by TRaPS with structural information of the magnetic film,
- and thus the identification of grain boundaries as a source for vortex core pinning.

In summary, the results presented in this thesis establish ultrafast transmission electron microscopy with *in-situ* current excitation as a viable tool for the study of magnetization dynamics. Together with the findings provided by TRaPS, it allowed insights into the pinning of magnetic vortex cores in polycrystalline samples. The combined findings of both methods provided evidence that grain boundaries are one source of pinning in magnetic films.

6.1 | Future Work

6.1.1 | Origin of vortex core pinning

In Chap. 5, we found evidence that vortex pinning is correlated with grain boundaries in the magnetic film. One possible cause for this behavior is the presence of grooves at grain boundaries [208–210]. Since the vortex core is a region of high exchange and magnetostatic energy, positioning it in a part of the sample with a reduced thickness would be energetically favorable. In its most pronounced form, this has been demonstrated by Uhlig et al. and coworkers, who found the vortex to be attracted by holes in the nanostructure [132].

To investigate this, TRaPS data could be correlated to a topological map of the sample. Such thickness measurements can be provided by TEM, e.g., via electron energy loss spectroscopy [211–213] or convergent beam electron diffraction [51]. Alternatively, specialized methods like scanning tunneling microscopy [214] or atomic force microscopy [215] could be employed.

The results of the sample topology can then be used to perform micromagnetic simulations. Min et al. and coworkers, for example, modeled thickness fluctuations by locally altering the saturation magnetization [165, 166].

6.1.2 | Future of TRaPS

As demonstrated in this thesis, TRaPS is a very capable method for studying the interaction between nanoscopic magnetic objects and defects in their host films. With sub-100 meV resolution in the reconstructed pinning potential, TRaPS is on par or even surpasses other methods developed for this task. Most notably, these other methods are based on the magneto-optical Kerr effect (see Chap. 3.3) [161–164] or nanomechanical torque magnetometry [157, 216, 217]. Where these methods only produce a scalar output when scanning the magnetic field, TRaPS provides a full image of the magnetic configuration at every scan position.

Yet, the implementation of TRaPS presented in this thesis only constitutes a proof-of-concept demonstration of the method. Two experimental improvements which could be implemented with readily available equipment are:

1. The use of a conventional Schottky or cold field emission gun to reduce image acquisition time. In this thesis, we used the modified UTEM gun in its continuous emission mode, which provides at least one order of magnitude lower beam current than a commercial unmodified Schottky emitter.

2. The use of an in-plane magnetizing sample holder instead of tilting the sample in an out-of-plane bias field [218–220]. This would allow to speed up the data acquisition, as it would avoid waiting for the tilt stage to drift to its final position, which accounts for the bulk of the acquisition time.

Additionally, the simple algorithm for the reconstruction of the pinning potential from TRaPS data can be improved upon. The ansatz of a convolution of the TRaPS map with a gaussian pinning potential could be replaced with a treatment of the individual defect sites. One possible alternative approach can be the use of a clustering algorithm to identify these sites [221].

6.1.3 | Beyond Fresnel imaging

Until today all studies imaging magnetization dynamics using UTEM make use of Fresnel contrast, directly [25, 198, 222]. Phase retrieval approaches offer to reconstruct the phase of the electron wave passing the magnetic material. Utilizing aberration-corrected instruments, these have been used to image magnetic solitons in a helical antiferromagnetic phase, which were < 4 nm in size [223]. While phase retrieval has commonly been done via the transport-of-intensity equation [41, 224], recently the use of differential programming has been reported [225]. Favorably for UTEM—where the average beam

current is usually limited—this approach offers to be more resilient against noise in the input image.

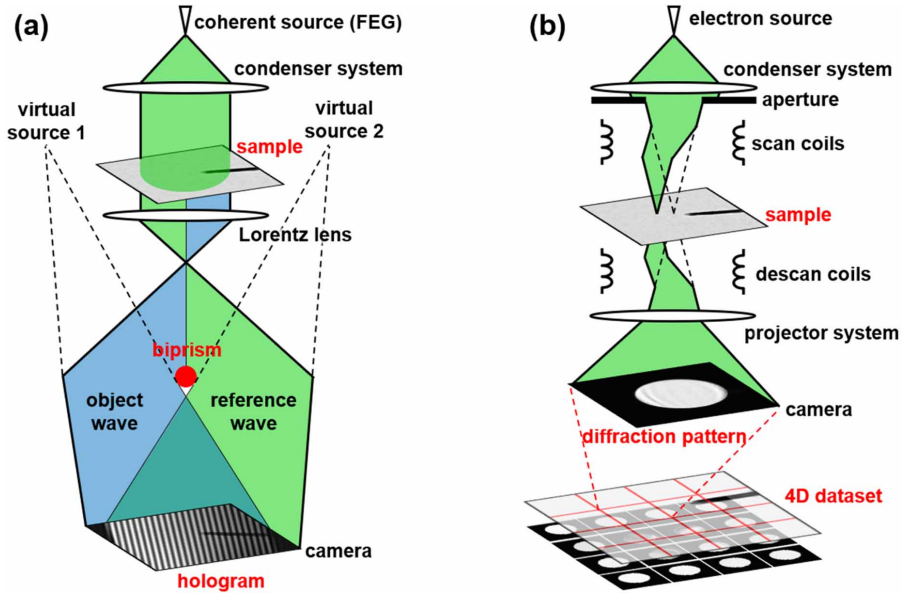

Figure 6.1: **Illustration of electron holography and pixelated DPC.** (a) In electron holography the sample (object wave) is illuminated next to a region of empty space (reference wave). By interfering the object with the reference wave, a hologram is formed, which allows the reconstruction of the phase imprinted on the object wave by the sample. (b) For pixelated DPC a focused electron beam is scanned across the sample. At every scan position, the transmitted electron beam is recorded in the far field. Reprinted from Ref. [226].

In addition, electron holography or differential phase contrast (DPC) could also be combined with UTEM to improve the spatial resolution imaging magnetization dynamics (cf. Fig. 6.1). Electron holography allows direct access to the Aharonov-Bohm phase by interfering a reference wave with part of the wave that passed the magnetic object, using a biprism [60, 227–229]. Recently, it has been demonstrated that electron holography is capable of resolving magnetic field in a CoFeB/Ta multilayer sample with sub-1 nm resolution [42, 230].

DPC, on the other hand, is a method based on scanning transmission electron microscopy (STEM), where a focused probe is scanned across the sample to generate an image. The magnetic induction of the sample is measured by recording the deflection of the electron beam due to the Lorentz force (see Eq. 2.4). Since, for magnetic samples, DPC has to be performed in field-free conditions, a secondary focusing lens further

from the sample has to be utilized, reducing the spatial resolution otherwise available in STEM. While these lenses often suffer from strong spherical aberrations, a resolution of 1 nm has been demonstrated using an aberration corrector in a commercially available instrument [172]. In addition, Shibata et al. and coworkers have developed an objective lens design that allows for atomic resolution with $< 0.2\,\mathrm{mT}$ field at the sample [173]. This was realized, by symmetrically placing two magnetic lenses above and below the sample, with fields that cancel each other at the sample region.

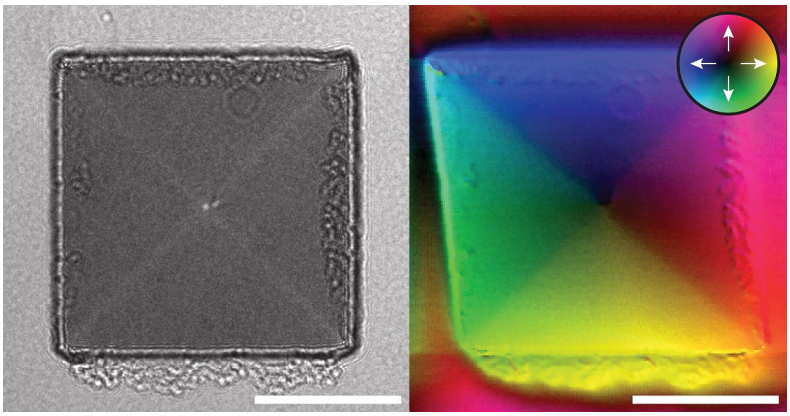

Figure 6.2: **Comparison between the magnetic contrast of a Fresnel micrograph and an image acquired using pixelated DPC.** The sample is a 30 nm thick and $2\,\mu\mathrm{m} \times 2\,\mu\mathrm{m}$ large permalloy ($Ni_{80}Fe_{20}$) square on a 30 nm thick SiN membrane. The DPC has been calculated based on the shift of the center of mass of the bright field disk in the diffraction images. Scalebar: 1 µm. Gratefully provided by John H. Gaida. © 2022 John H. Gaida.

A preliminary DPC image recorded by John H. Gaida at the Göttingen UTEM is shown in Fig. 6.2 next to a Fresnel micrograph. Unlike traditional DPC, where the beam deflection is detected with segmented detector [40, 231], here, a full diffraction image was recorded at every scan position (see also Fig. 6.1b). The deflection angle can then be calculated from the center of mass of the bright-field disk [232]. This method is called pixelated-DPC and is a variant of 4D STEM, where STEM signals are recorded with fast TEM cameras [65, 226, 233–235]. One advantage of pixelated DPC is an increase in information transfer efficiency for many spatial frequencies over segmented detectors [233]. Additionally, DPC has been used to disentangle magnetic and grain contrast [236].

In addition, Lorentz electron ptychography is currently also in development [237]. It combines pixelated DPC with electron holography and also allows for an algorithmic reconstruction of the electron phase. For low-dose cryo-electron microscopy, ptychography has been demonstrated to reduce the necessary electron dose by two orders of

magnitude for the same phase sensitivity compared to Fresnel imaging [238, 239]. If these findings can be reproduced for imaging magnetic samples, this could especially profit UTEM, due to its constraints on the average electron current.

6.2 | Final Remarks

The achievements presented in this cumulative thesis showcase the potential of time-resolved Lorentz microscopy for the study of current-driven magnetization dynamics. With the implementation of more advanced imaging techniques, future studies will see further improvement in spatial resolution and may enable quantitative insight into nanoscale magnetic processes. With the ongoing search for ever-smaller magnetic textures, investigating the role of defects intrinsic to the magnetic host materials will be of increasing importance. Here, TEM will be able to make vital contributions, using methods like TRaPS in combination with the nanoscale characterization of magnetic thin films.

Bibliography

[1] A. Hubert and R. Schäfer, *Magnetic Domains* (Springer Berlin Heidelberg, Berlin, Heidelberg, 1998).

[2] R. P. Cowburn, D. K. Koltsov, A. O. Adeyeye, M. E. Welland, and D. M. Tricker, "Single-Domain Circular Nanomagnets", Physical Review Letters **83**, 1042–1045 (1999).

[3] T. Skyrme, "A unified field theory of mesons and baryons", Nuclear Physics **31**, 556–569 (1962).

[4] S. Mühlbauer, B. Binz, F. Jonietz, C. Pfleiderer, A. Rosch, A. Neubauer, R. Georgii, and P. Boni, "Skyrmion Lattice in a Chiral Magnet", Science **323**, 915–919 (2009).

[5] X. Z. Yu, Y. Onose, N. Kanazawa, J. H. Park, J. H. Han, Y. Matsui, N. Nagaosa, and Y. Tokura, "Real-space observation of a two-dimensional skyrmion crystal", Nature **465**, 901–904 (2010).

[6] A. K. Nayak, V. Kumar, T. Ma, P. Werner, E. Pippel, R. Sahoo, F. Damay, U. K. Rößler, C. Felser, and S. S. P. Parkin, "Magnetic antiskyrmions above room temperature in tetragonal Heusler materials.", Nature **548**, 561–566 (2017).

[7] C. Phatak, A. K. Petford-Long, and O. Heinonen, "Direct Observation of Unconventional Topological Spin Structure in Coupled Magnetic Discs", Physical Review Letters **108**, 067205 (2012).

[8] X. Z. Yu, W. Koshibae, Y. Tokunaga, K. Shibata, Y. Taguchi, N. Nagaosa, and Y. Tokura, "Transformation between meron and skyrmion topological spin textures in a chiral magnet", Nature **564**, 95–98 (2018).

[9] N. Gao, S. .-. Je, M. .-. Im, J. W. Choi, M. Yang, Q. Li, T. Y. Wang, S. Lee, H. .-. Han, K. .-. Lee, W. Chao, C. Hwang, J. Li, and Z. Q. Qiu, "Creation and annihilation of topological meron pairs in in-plane magnetized films", Nature Communications **10**, 5603 (2019).

[10] S. S. P. Parkin, M. Hayashi, and L. Thomas, "Magnetic Domain-Wall Racetrack Memory", Science **320**, 190–194 (2008).

[11] A. Fert, V. Cros, and J. Sampaio, "Skyrmions on the track", Nature Nanotechnology **8**, 152–156 (2013).

[12] L. D. Geng and Y. M. Jin, "Magnetic vortex racetrack memory", Journal of Magnetism and Magnetic Materials **423**, 84–89 (2017).

[13] H. Jung, Y.-S. Choi, K.-S. Lee, D.-S. Han, Y.-S. Yu, M.-Y. Im, P. Fischer, and S.-K. Kim, "Logic Operations Based on Magnetic-Vortex-State Networks", ACS Nano **6**, 3712–3717 (2012).

[14] X. Zhang, M. Ezawa, and Y. Zhou, "Magnetic skyrmion logic gates: conversion, duplication and merging of skyrmions", Scientific Reports **5**, 9400 (2015).

[15] F. Macià, A. D. Kent, and F. C. Hoppensteadt, "Spin-wave interference patterns created by spin-torque nano-oscillators for memory and computation", Nanotechnology **22**, 095301 (2011).

[16] J. Torrejon, M. Riou, F. A. Araujo, S. Tsunegi, G. Khalsa, D. Querlioz, P. Bortolotti, V. Cros, K. Yakushiji, A. Fukushima, H. Kubota, S. Yuasa, M. D. Stiles, and J. Grollier, "Neuromorphic computing with nanoscale spintronic oscillators", Nature **547**, 428–431 (2017).

[17] J. Grollier, D. Querlioz, K. Y. Camsari, K. Everschor-Sitte, S. Fukami, and M. D. Stiles, "Neuromorphic spintronics", Nature Electronics **3**, 360–370 (2020).

[18] F. B. Mancoff, N. D. Rizzo, B. N. Engel, and S. Tehrani, "Phase-locking in double-point-contact spin-transfer devices", Nature **437**, 393–395 (2005).

[19] A. Dussaux, B. Georges, J. Grollier, V. Cros, A. Khvalkovskiy, A. Fukushima, M. Konoto, H. Kubota, K. Yakushiji, S. Yuasa, K. Zvezdin, K. Ando, and A. Fert, "Large microwave generation from current-driven magnetic vortex oscillators in magnetic tunnel junctions", Nature Communications **1**, 8 (2010).

[20] E. Beaurepaire, J.-C. Merle, A. Daunois, and J.-Y. Bigot, "Ultrafast Spin Dynamics in Ferromagnetic Nickel", Physical Review Letters **76**, 4250–4253 (1996).

[21] C. D. Stanciu, F. Hansteen, A. V. Kimel, A. Kirilyuk, A. Tsukamoto, A. Itoh, and T. Rasing, "All-Optical Magnetic Recording with Circularly Polarized Light", Physical Review Letters **99**, 047601 (2007).

[22] T. Kampfrath, A. Sell, G. Klatt, A. Pashkin, S. Mährlein, T. Dekorsy, M. Wolf, M. Fiebig, A. Leitenstorfer, and R. Huber, "Coherent terahertz control of antiferromagnetic spin waves", Nature Photonics **5**, 31–34 (2011).

[23] T. Eggebrecht, M. Möller, J. G. Gatzmann, N. R. d. Silva, A. Feist, U. Martens, H. Ulrichs, M. Münzenberg, C. Ropers, and S. Schäfer, "Light-Induced Metastable Magnetic Texture Uncovered by in situ Lorentz Microscopy", Physical Review Letters **118**, 097203 (2017).

[24] X. Fu, S. D. Pollard, B. Chen, B.-K. K. Yoo, H. Yang, and Y. Zhu, "Optical manipulation of magnetic vortices visualized in situ by Lorentz electron microscopy", Science Advances **4**, eaat3077 (2018).

[25] N. Rubiano, "Ultrafast Lorentz Microscopy using High-Coherence Electron Pulses", (2019).

[26] K. Gerlinger, B. Pfau, F. Büttner, M. Schneider, L.-M. Kern, J. Fuchs, D. Engel, C. M. Günther, M. Huang, I. Lemesh, L. Caretta, A. Churikova, P. Hessing, C. Klose, C. Strüber, C. v. K. Schmising, S. Huang, A. Wittmann, K. Litzius, D. Metternich, R. Battistelli, K. Bagschik, A. Sadovnikov, G. S. D. Beach, and S. Eisebitt, "Application concepts for ultrafast laser-induced skyrmion creation and annihilation", Applied Physics Letters **118**, 192403 (2021).

[27] B. B. Argyle, E. Terrenzio, J. Slonczewski, J. Slonczenwski, Y. Heights, B. B. Argyle, E. Terrenzio, and J. Slonczewski, "Magnetic vortex dynamics using the optical Cotton-Mouton effect", Physical review letters **53**, 190–194 (1984).

[28] J. P. Park, P. Eames, D. M. Engebretson, J. Berezovsky, and P. A. Crowell, "Imaging of spin dynamics in closure domain and vortex structures", Physical Review B **67**, 020403 (2003).

[29] S.-B. Choe, "Vortex Core-Driven Magnetization Dynamics", Science **304**, 420–422 (2004).

[30] S. Kasai, Y. Nakatani, K. Kobayashi, H. Kohno, and T. Ono, "Current-Driven Resonant Excitation of Magnetic Vortices", Physical Review Letters **97**, 107204 (2006).

[31] V. S. Pribiag, I. N. Krivorotov, G. D. Fuchs, P. M. Braganca, O. Ozatay, J. C. Sankey, D. C. Ralph, and R. a. Buhrman, "Magnetic vortex oscillator driven by dc spin-polarized current", Nature Physics **3**, 498–502 (2007).

[32] D. Ralph and M. Stiles, "Spin transfer torques", Journal of Magnetism and Magnetic Materials **320**, 1190–1216 (2008).

[33] L. Liu, T. Moriyama, D. C. Ralph, and R. A. Buhrman, "Spin-Torque Ferromagnetic Resonance Induced by the Spin Hall Effect", Physical Review Letters **106**, 036601 (2011).

[34] S. Emori, U. Bauer, S.-M. Ahn, E. Martinez, and G. S. D. Beach, "Current-driven dynamics of chiral ferromagnetic domain walls", Nature Materials **12**, 611–616 (2013).

[35] K. Litzius, I. Lemesh, B. Krüger, P. Bassirian, L. Caretta, K. Richter, F. Büttner, K. Sato, O. A. Tretiakov, J. Förster, R. M. Reeve, M. Weigand, I. Bykova, H. Stoll, G. Schütz, G. S. D. Beach, and M. Kläui, "Skyrmion Hall effect revealed by direct time-resolved X-ray microscopy", Nature Physics **13**, 170–175 (2017).

[36] S. Tehrani, B. Engel, J. Slaughter, E. Chen, M. DeHerrera, M. Durlam, P. Naji, R. Whig, J. Janesky, and J. Calder, "Recent developments in magnetic tunnel junction MRAM", IEEE Transactions on Magnetics **36**, 2752–2757 (2000).

[37] N. Locatelli, D. Vodenicarevic, W. Zhao, J.-O. Klein, J. Grollier, and D. Querlioz, "Vortex-Based Spin Transfer Oscillator Compact Model for IC Design", 2015 IEEE International Symposium on Circuits and Systems (ISCAS), 589–592 (2015).

[38] B. Engel, J. Akerman, B. Butcher, R. Dave, M. DeHerrera, M. Durlam, G. Grynkewich, J. Janesky, S. Pietambaram, N. Rizzo, J. Slaughter, K. Smith, J. Sun, and S. Tehrani, "A 4-Mb toggle MRAM based on a novel bit and switching method", IEEE Transactions on Magnetics **41**, 132–136 (2005).

[39] M. E. Hale, H. W. Fuller, and H. Rubinstein, "Magnetic Domain Observations by Electron Microscopy", Journal of Applied Physics **30**, 789–791 (1959).

[40] J. N. Chapman, P. E. Batson, E. M. Waddell, and R. P. Ferrier, "The direct determination of magnetic domain wall profiles by differential phase contrast electron microscopy", Ultramicroscopy **3**, 203–214 (1978).

[41] M. D. Graef, "2. Lorentz microscopy: Theoretical basis and image simulations", Experimental Methods in the Physical Sciences **36**, 27–67 (2001).

[42] T. Tanigaki, T. Akashi, A. Sugawara, K. Miura, J. Hayakawa, K. Niitsu, T. Sato, X. Yu, Y. Tomioka, K. Harada, D. Shindo, Y. Tokura, and H. Shinada, "Magnetic field observations in CoFeB/Ta layers with 0.67-nm resolution by electron holography", Scientific Reports **7**, 16598 (2017).

[43] O. Bostanjoglo and T. Rosin, "Ultrasonically Induced Magnetic Reversals Observed by Stroboscopic Electron Microscopy", Optica Acta: International Journal of Optics **24**, 657–664 (1977).

[44] K. B. Schliep, P. Quarterman, J.-P. P. Wang, and D. J. Flannigan, "Picosecond Fresnel transmission electron microscopy", Applied Physics Letters **110**, 222404 (2017).

[45] R. Bormann, S. Strauch, S. Schäfer, and C. Ropers, "An ultrafast electron microscope gun driven by two-photon photoemission from a nanotip cathode", Journal of Applied Physics **118**, 173105 (2015).

[46] A. Feist, N. Bach, N. R. d. Silva, T. Danz, M. Möller, K. E. Priebe, T. Domröse, J. G. Gatzmann, S. Rost, J. Schauss, S. Strauch, R. Bormann, M. Sivis, S. Schäfer, and C. Ropers, "Ultrafast transmission electron microscopy using a laser-driven field emitter: Femtosecond resolution with a high coherence electron beam", Ultramicroscopy **176**, 63–73 (2017).

[47] F. Houdellier, G. M. Caruso, S. Weber, M. Kociak, and A. Arbouet, "Development of a high brightness ultrafast Transmission Electron Microscope based on a laser-driven cold field emission source", Ultramicroscopy **186**, 128–138 (2018).

[48] N. R. d. Silva, M. Möller, A. Feist, H. Ulrichs, C. Ropers, and S. Schäfer, "Nanoscale Mapping of Ultrafast Magnetization Dynamics with Femtosecond Lorentz Microscopy", Physical Review X **8**, 031052 (2018).

[49] M. Zhang, Z.-A. Li, S. Sun, P. Xu, C. Zhu, H. Tian, Z. Li, Y. Zhang, H. Yang, and J. Li, "High Spatiotemporal Resolution ofMagnetic Dynamics in Mn-Ni-Ga via Four-Dimensional Lorentz Microscopy Ming", Physical Review Applied **12**, 034037 (2019).

[50] G. Cao, S. Jiang, J. Åkerman, and J. Weissenrieder, "Femtosecond laser driven precessing magnetic gratings", Nanoscale **13**, 3746–3756 (2021).

[51] D. B. Williams and C. B. Carter, *Transmission Electron Microscopy, A Textbook for Materials Science* (CRC Press, 2009).

[52] L. Reimer and H. Kohl, *Transmission Electron Microscopy* (2008).

[53] E. J. Kirkland, *Advanced computing in electron microscopy* (2010).

[54] E. Abbe, "Beiträge zur Theorie des Mikroskops und der mikroskopischen Wahrnehmung", Archiv für Mikroskopische Anatomie **9**, 413–468 (1873).

[55] E. Ruska, "The early development of electron lenses and electron microscopy.", Microscopica acta. Supplement, 1–140 (1980).

[56] S. J. Pennycook, M. Varela, C. J. D. Hetherington, and A. I. Kirkland, "Materials Advances through Aberration-Corrected Electron Microscopy", MRS Bulletin **31**, 36–43 (2006).

[57] D. A. Muller, "Structure and bonding at the atomic scale by scanning transmission electron microscopy", Nature Materials **8**, 263–270 (2009).

[58] M. D. Graef, *Magnetic Imaging and Its Applications to Materials*, edited by [. Graef, {Zhu, Marc and}, and Yimei"], Vol. 36, Experimental Methods in the Physical Sciences (CRC Press, New York, 2001).

[59] A. Petford-Long and J. Chapman, "Magnetic Microscopy of Nanostructures", in *Magnetic microscopy of nanostructures*, edited by ["Hopster, {Oepen, Herbert and}, and H. Peter"], NanoScience and Technology (Springer Berlin Heidelberg, 2005), pp. 67–86.

[60] R. E. Dunin-Borkowski, A. Kovács, T. Kasama, M. R. McCartney, and D. J. Smith, "Springer Handbook of Microscopy", Springer Handbooks, 767–818 (2019).

[61] R. Wade, "A brief look at imaging and contrast transfer", Ultramicroscopy **46**, 145–156 (1992).

[62] Y. Aharonov and D. Bohm, "Significance of Electromagnetic Potentials in the Quantum Theory", Physical Review **115**, 485–491 (1959).

[63] A. Vansteenkiste, J. Leliaert, M. Dvornik, M. Helsen, F. Garcia-Sanchez, and B. V. Waeyenberge, "The design and verification of MuMax3", AIP Advances **4**, 137133 (2014).

[64] M. Mansuripur, "Computation of electron diffraction patterns in Lorentz electron microscopy of thin magnetic films", Journal of Applied Physics **69**, 2455–2464 (1991).

[65] G. McMullan, A. Faruqi, and R. Henderson, "Chapter One Direct Electron Detectors", Methods in Enzymology **579**, 1–17 (2016).

[66] B. D. A. Levin, "Direct detectors and their applications in electron microscopy for materials science", Journal of Physics: Materials **4**, 042005 (2021).

[67] Direct Electron - Celeritas Camera. Access Date: 05/19/2022. https://www.directelectron.com/products/celeritas/.

[68] T. Poikela, J. Plosila, T. Westerlund, M. Campbell, M. D. Gaspari, X. Llopart, V. Gromov, R. Kluit, M. v. Beuzekom, F. Zappon, V. Zivkovic, C. Brezina, K. Desch, Y. Fu, and A. Kruth, "Timepix3: a 65K channel hybrid pixel readout chip with simultaneous ToA/ToT and sparse readout", Journal of Instrumentation **9**, C05013–C05013 (2014).

[69] E. Frojdh, M. Campbell, M. D. Gaspari, S. Kulis, X. Llopart, T. Poikela, and L. Tlustos, "Timepix3: first measurements and characterization of a hybrid-pixel detector working in event driven mode", Journal of Instrumentation **10**, C01039–C01039 (2015).

[70] A. Oelsner, O. Schmidt, M. Schicketanz, M. Klais, G. Schönhense, V. Mergel, O. Jagutzki, and H. Schmidt-Böcking, "Microspectroscopy and imaging using a delay line detector in time-of-flight photoemission microscopy", Review of Scientific Instruments **72**, 3968–3974 (2001).

[71] T. Weßels, S. Däster, Y. Murooka, B. Zingsem, V. Migunov, M. Kruth, S. Finizio, P.-H. Lu, A. Kovács, A. Oelsner, K. Müller-Caspary, Y. Acremann, and R. E. Dunin-Borkowski, "Continuous illumination picosecond imaging using a delay line detector in a transmission electron microscope", Ultramicroscopy, 113392 (2021).

[72] A. Feist, "Next-Generation Ultrafast Transmission Electron Microscopy – Development and Applications", (2018).

[73] A. Arbouet, G. M. Caruso, and F. Houdellier, "Chapter One Ultrafast Transmission Electron Microscopy: Historical Development, Instrumentation, and Applications", Advances in Imaging and Electron Physics **207**, 1–72 (2018).

[74] L. Zhang, J. P. Hoogenboom, B. Cook, and P. Kruit, "Photoemission sources and beam blankers for ultrafast electron microscopy", Structural Dynamics **6**, 051501 (2019).

[75] O. Bostanjoglo and T. Nink, "Liquid motion in laser pulsed Al, Co and Au films", Applied Surface Science **109**, 101–105 (1997).

[76] O. Bostanjoglo, R. Elschner, Z. Mao, T. Nink, and M. Weingärtner, "Nanosecond electron microscopes", Ultramicroscopy **81**, 141–147 (2000).

[77] A. Gahlmann, S. T. Park, and A. H. Zewail, "Ultrashort electron pulses for diffraction, crystallography and microscopy : theoretical and experimental resolutions", Physical Chemistry Chemical Physics **10**, 2894–2909 (2008).

[78] H. Dömer and O. Bostanjoglo, "High-speed transmission electron microscope", Review of Scientific Instruments **74**, 4369–4372 (2003).

[79] B. W. Reed, T. LaGrange, R. M. Shuttlesworth, D. J. Gibson, G. H. Campbell, and N. D. Browning, "Solving the accelerator-condenser coupling problem in a nanosecond dynamic transmission electron microscope", Review of Scientific Instruments **81**, 053706 (2010).

[80] T. LaGrange, B. W. Reed, and D. J. Masiel, "Movie-mode dynamic electron microscopy", MRS Bulletin **40**, 22–28 (2015).

[81] O. Bostanjoglo and T. Rosin, "Resonance oscillations of magnetic domain walls and bloch lines observed by stroboscopic electron microscopy", physica status solidi (a) **57**, 561–568 (1980).

[82] A. H. Zewail, "Four-Dimensional Electron Microscopy", Science **328**, 187–193 (2010).

[83] B. Barwick, H. S. Park, O.-H. Kwon, J. S. Baskin, and A. H. Zewail, "4D Imaging of Transient Structures and Morphologies in Ultrafast Electron Microscopy", Science **322**, 1227–1231 (2008).

[84] P. Hommelhoff, Y. Sortais, A. Aghajani-Talesh, and M. A. Kasevich, "Field Emission Tip as a Nanometer Source of Free Electron Femtosecond Pulses", Physical Review Letters **96**, 077401 (2006).

[85] C. Ropers, D. R. Solli, C. P. Schulz, C. Lienau, and T. Elsaesser, "Localized Multiphoton Emission of Femtosecond Electron Pulses from Metal Nanotips", Physical Review Letters **98**, 043907 (2006).

[86] G. M. Caruso, F. Houdellier, P. Abeilhou, and A. Arbouet, "Development of an ultrafast electron source based on a cold-field emission gun for ultrafast coherent TEM", Applied Physics Letters **111**, 023101 (2017).

[87] C. Zhu, D. Zheng, H. Wang, M. Zhang, Z. Li, S. Sun, P. Xu, H. Tian, Z. Li, H. Yang, and J. Li, "Development of analytical ultrafast transmission electron microscopy based on laser-driven Schottky field emission", Ultramicroscopy **209**, 112887 (2020).

[88] P. K. Olshin, M. Drabbels, and U. J. Lorenz, "Characterization of a time-resolved electron microscope with a Schottky field emission gun", Structural Dynamics **7**, 054304 (2020).

[89] B. Cook, M. Bronsgeest, K. Hagen, and P. Kruit, "Improving the energy spread and brightness of thermal-field (Schottky) emitters with PHAST—PHoto Assisted Schottky Tip", Ultramicroscopy **109**, 403–412 (2009).

[90] D.-S. Yang, O. F. Mohammed, and A. H. Zewail, "Scanning ultrafast electron microscopy", Proceedings of the National Academy of Sciences **107**, 14993–14998 (2010).

[91] N. Bach, T. Domröse, A. Feist, T. Rittmann, S. Strauch, C. Ropers, and S. Schäfer, "Coulomb interactions in high-coherence femtosecond electron pulses from tip emitters", Structural Dynamics **6**, 014301 (2019).

[92] S. Pollard, L. Huang, K. Buchanan, D. Arena, and Y. Zhu, "Direct dynamic imaging of non-adiabatic spin torque effects", Nature Communications **3**, 1028 (2012).

[93] A. Feist, N. R. d. Silva, W. Liang, C. Ropers, and S. Schäfer, "Nanoscale diffractive probing of strain dynamics in ultrafast transmission electron microscopy", Structural Dynamics **5**, 014302 (2018).

[94] N. Bach, A. Feist, M. Möller, C. Ropers, and S. Schäfer, "Tailored nanophononic wavefield in a patterned bilayer system probed by ultrafast convergent beam electron diffraction", Structural Dynamics **9**, 034301 (2022).

[95] T. Danz, T. Domröse, and C. Ropers, "Ultrafast nanoimaging of the order parameter in a structural phase transition", Science **371**, 371–374 (2021).

[96] A. Feist, K. E. Echternkamp, J. Schauss, S. V. Yalunin, S. Schäfer, and C. Ropers, "Quantum coherent optical phase modulation in an ultrafast transmission electron microscope.", Nature **521**, 200–3 (2015).

[97] B. Schröder, T. Weber, S. V. Yalunin, T. Kiel, C. Matyssek, M. Sivis, S. Schäfer, F. V. Cube, S. Irsen, K. Busch, C. Ropers, and S. Linden, "Real-space imaging of nanotip plasmons using electron energy loss spectroscopy", Physical Review B - Condensed Matter and Materials Physics **92**, 1–7 (2015).

[98] K. E. Echternkamp, A. Feist, S. Schäfer, and C. Ropers, "Ramsey-type phase control of free-electron beams", Nature Physics **12**, 1–6 (2016).

[99] K. E. Priebe, C. Rathje, S. V. Yalunin, T. Hohage, A. Feist, S. Schäfer, and C. Ropers, "Attosecond electron pulse trains and quantum state reconstruction in ultrafast transmission electron microscopy", Nature Photonics **11**, 793–797 (2017).

[100] T. R. Harvey, J.-W. Henke, O. Kfir, H. Lourenço-Martins, A. Feist, F. J. G. d. Abajo, and C. Ropers, "Probing Chirality with Inelastic Electron-Light Scattering", Nano Letters **20**, 4377–4383 (2020).

[101] O. Kfir, H. Lourenço-Martins, G. Storeck, M. Sivis, T. R. Harvey, T. J. Kippenberg, A. Feist, and C. Ropers, "Controlling free electrons with optical whispering-gallery modes", Nature **582**, 46–49 (2020).

[102] T. R. Harvey, N. R. d. Silva, J. H. Gaida, M. Möller, A. Feist, S. Schäfer, and C. Ropers, "Ultrafast electron microscopy for probing magnetic dynamics", MRS Bulletin **46**, 711–719 (2021).

[103] V. I. Petrov, G. V. Spivak, and O. P. Pavlyuchenko, "Electron microscopy of the magnetic structure of thin films", Uspekhi Fizicheskih Nauk **106**, 229 (1972).

[104] H. S. Park, J. S. Baskin, and A. H. Zewail, "4D Lorentz Electron Microscopy Imaging: Magnetic Domain Wall Nucleation, Reversal, and Wave Velocity", Nano Letters **10**, 3796–3803 (2010).

[105] S. Ji, L. Piazza, G. Cao, S. T. Park, B. W. Reed, D. J. Masiel, and J. Weissenrieder, "Influence of cathode geometry on electron dynamics in an ultrafast electron microscope", Structural Dynamics **4**, 054303 (2017).

[106] C. Jing, Y. Zhu, A. Liu, K. Schliep, X. Fu, Y. Zhao, E. Montgomery, W. Rush, A. Kanareykin, M. Katz, and J. Lau, "Tunable electron beam pulser for picoseconds stroboscopic microscopy in transmission electron microscopes", Ultramicroscopy **207**, 112829 (2019).

[107] J. W. Lau, K. B. Schliep, M. B. Katz, V. J. Gokhale, J. J. Gorman, C. Jing, A. Liu, Y. Zhao, E. Montgomery, H. Choe, W. Rush, A. Kanareykin, X. Fu, and Y. Zhu, "Laser-free GHz stroboscopic transmission electron microscope: Components, system integration, and practical considerations for pump–probe measurements", Review of Scientific Instruments **91**, 021301 (2020).

[108] X. Fu, E. Wang, Y. Zhao, A. Liu, E. Montgomery, V. J. Gokhale, J. J. Gorman, C. Jing, J. W. Lau, and Y. Zhu, "Direct visualization of electromagnetic wave dynamics by laser-free ultrafast electron microscopy", Science Advances **6**, eabc3456 (2020).

[109] S. A. Reisbick, M.-G. Han, C. Liu, Y. Zhao, E. Montgomery, C. Jing, V. J. Gokhale, J. J. Gorman, J. W. Lau, and Y. Zhu, "Stroboscopic ultrafast imaging using RF strip-lines in a commercial transmission electron microscope", Ultramicroscopy **235**, 113497 (2022).

[110] W. F. Brown, "THE FUNDAMENTAL THEOREM OF THE THEORY OF FINE FERROMAGNETIC PARTICLES*", Annals of the New York Academy of Sciences **147**, 463–488 (1969).

[111] W. Scholz, K. Guslienko, V. Novosad, D. Suess, T. Schrefl, R. Chantrell, and J. Fidler, "Transition from single-domain to vortex state in soft magnetic cylindrical nanodots", Journal of Magnetism and Magnetic Materials **266**, 155–163 (2003).

[112] M. Goiriena-Goikoetxea, A. García-Arribas, M. Rouco, A. V. Svalov, and J. M. Barandiaran, "High-yield fabrication of 60 nm Permalloy nanodiscs in well-defined magnetic vortex state for biomedical applications", Nanotechnology **27**, 175302 (2016).

[113] S.-H. Chung, R. D. McMichael, D. T. Pierce, and J. Unguris, "Phase diagram of magnetic nanodisks measured by scanning electron microscopy with polarization analysis", Physical Review B **81**, 024410 (2010).

[114] K. L. Metlov and K. Y. Guslienko, "Stability of magnetic vortex in soft magnetic nano-sized circular cylinder", Journal of Magnetism and Magnetic Materials **242**, 1015–1017 (2002).

[115] K. L. Metlov, "Equilibrium large vortex state in ferromagnetic disks", Journal of Applied Physics **113**, 223905 (2013).

[116] M. Goiriena-Goikoetxea, K. Y. Guslienko, M. Rouco, I. Orue, E. Berganza, M. Jaafar, A. Asenjo, M. L. Fernández-Gubieda, L. F. Barquín, and A. García-Arribas, "Magnetization reversal in circular vortex dots of small radius", Nanoscale **9**, 11269–11278 (2017).

[117] M. Schneider, H. Hoffmann, and J. Zweck, "Lorentz microscopy of circular ferromagnetic permalloy nanodisks", Applied Physics Letters **77**, 2909–2911 (2000).

[118] T. Shinjo, T. Okuno, R. Hassdorf, K. Shigeto, and T. Ono, "Magnetic Vortex Core Observation in Circular Dots of Permalloy", Science **289**, 930–932 (2000).

[119] J. Raabe, R. Pulwey, R. Sattler, T. Schweinböck, J. Zweck, and D. Weiss, "Magnetization pattern of ferromagnetic nanodisks", Journal of Applied Physics **88**, 4437–4439 (2000).

[120] A. Wachowiak, J. Wiebe, M. Bode, O. Pietzsch, M. Morgenstern, and R. Wiesendanger, "Direct observation of internal spin structure of magnetic vortex cores", Science **298**, 577–580 (2002).

[121] K. Y. Guslienko, B. A. Ivanov, V. Novosad, Y. Otani, H. Shima, and K. Fukamichi, "Eigenfrequencies of vortex state excitations in magnetic submicron-size disks", Journal of Applied Physics **91**, 8037–8039 (2002).

[122] K. Y. Guslienko, W. Scholz, R. W. Chantrell, and V. Novosad, "Vortex-state oscillations in soft magnetic cylindrical dots", Physical Review B **71**, 144407 (2005).

[123] N. Bukin, C. McKeever, E. Burgos-Parra, P. S. Keatley, R. J. Hicken, F. Y. Ogrin, G. Beutier, M. Dupraz, H. Popescu, N. Jaouen, F. Yakhou-Harris, S. A. Cavill, and G. v. d. Laan, "Time-resolved imaging of magnetic vortex dynamics using holography with extended reference autocorrelation by linear differential operator", Scientific Reports **6**, 36307 (2016).

[124] B. V. Waeyenberge, A. Puzic, H. Stoll, K. W. Chou, T. Tyliszczak, R. Hertel, M. Fähnle, H. Brückl, K. Rott, G. Reiss, I. Neudecker, D. Weiss, C. H. Back, and G. Schütz, "Magnetic vortex core reversal by excitation with short bursts of an alternating field", Nature **444**, 461–464 (2006).

[125] R. Hertel, S. Gliga, M. Fähnle, and C. M. Schneider, "Ultrafast Nanomagnetic Toggle Switching of Vortex Cores", Physical Review Letters **98**, 117201 (2007).

[126] K. Yamada, S. Kasai, Y. Nakatani, K. Kobayashi, H. Kohno, A. Thiaville, and T. Ono, "Electrical switching of the vortex core in a magnetic disk", Nature Materials **6**, 270–273 (2007).

[127] Y. Liu, S. Gliga, R. Hertel, and C. M. Schneider, "Current-induced magnetic vortex core switching in a Permalloy nanodisk", Applied Physics Letters **91**, 112501 (2007).

[128] M. Curcic, B. V. Waeyenberge, A. Vansteenkiste, M. Weigand, V. Sackmann, H. Stoll, M. Fähnle, T. Tyliszczak, G. Woltersdorf, C. H. Back, and G. Schütz, "Polarization selective magnetic vortex dynamics and core reversal in rotating magnetic fields", Physical Review Letters **101**, 197204 (2008).

[129] P. Wohlhüter, M. T. Bryan, P. Warnicke, S. Gliga, S. E. Stevenson, G. Heldt, L. Saharan, A. K. Suszka, C. Moutafis, R. V. Chopdekar, J. Raabe, T. Thomson, G. Hrkac, and L. J. Heyderman, "Nanoscale switch for vortex polarization mediated by Bloch core formation in magnetic hybrid systems", Nature Communications **6**, 1–6 (2015).

[130] R. Antos, Y. Otani, and J. Shibata, "Magnetic vortex dynamics", Journal of the Physical Society of Japan **77**, 1–8 (2008).

[131] K. Y. Guslienko, V. Novosad, Y. Otani, H. Shima, and K. Fukamichi, "Field evolution of magnetic vortex state in ferromagnetic disks", Applied Physics Letters **78**, 3848–3850 (2001).

[132] T. Uhlig, M. Rahm, C. Dietrich, R. Höllinger, M. Heumann, D. Weiss, and J. Zweck, "Shifting and Pinning of a Magnetic Vortex Core in a Permalloy Dot by a Magnetic Field", Physical Review Letters **95**, 237205 (2005).

[133] N. A. Usov and S. E. Peschany, "Magnetization curling in a fine cylindrical particle", Journal of Magnetism and Magnetic Materials **118**, 290–294 (1993).

[134] K. Guslienko, V. Novosad, Y. Otani, H. Shima, and K. Fukamichi, "Magnetization reversal due to vortex nucleation, displacement, and annihilation in submicron ferromagnetic dot arrays", Physical Review B **65**, 1–10 (2001).

[135] M. J. Donahue and D. G. Porter, "OOMMF user's guide, version 1.0", 10.6028/nist.ir.6376 (1999).

[136] J. Burgess, J. Losby, and M. Freeman, "An analytical model for vortex core pinning in a micromagnetic disk", Journal of Magnetism and Magnetic Materials **361**, 140–149 (2014).

[137] B. Krüger, M. Najafi, S. Bohlens, R. Frömter, D. P. F. Möller, and D. Pfannkuche, "Proposal of a Robust Measurement Scheme for the Nonadiabatic Spin Torque Using the Displacement of Magnetic Vortices", Physical Review Letters **104**, 077201 (2010).

[138] B. Krüger, A. Drews, M. Bolte, U. Merkt, D. Pfannkuche, and G. Meier, "Harmonic oscillator model for current- and field-driven magnetic vortices", Physical Review B **76**, 224426 (2007).

[139] L. LANDAU and E. LIFSHITZ, "Perspectives in Theoretical Physics", 51–65 (1992).

[140] T. L. Gilbert, "Classics in Magnetics - A Phenomenological Theory of Damping in Ferromagnetic Materials", IEEE Transactions on Magnetics **40**, 3443–3449 (2004).

[141] S. Zhang and Z. Li, "Roles of Nonequilibrium Conduction Electrons on the Magnetization Dynamics of Ferromagnets", Physical Review Letters **93**, 127204 (2004).

[142] G. Beach, M. Tsoi, and J. Erskine, "Current-induced domain wall motion", Journal of Magnetism and Magnetic Materials **320**, 1272–1281 (2008).

[143] A. A. Thiele, "Steady-State Motion of Magnetic Domains", Physical Review Letters **30**, 230–233 (1973).

[144] A. A. Thiele, "Applications of the gyrocoupling vector and dissipation dyadic in the dynamics of magnetic domains", Journal of Applied Physics **45**, 377–393 (1974).

[145] A. Thiaville, Y. Nakatani, J. Miltat, and Y. Suzuki, "Micromagnetic understanding of current-driven domain wall motion in patterned nanowires", Europhysics Letters (EPL) **69**, 990–996 (2005).

[146] M. Bolte, G. Meier, B. Krüger, A. Drews, R. Eiselt, L. Bocklage, S. Bohlens, T. Tyliszczak, A. Vansteenkiste, B. V. Waeyenberge, K. W. Chou, A. Puzic, and H. Stoll, "Time-Resolved X-Ray Microscopy of Spin-Torque-Induced Magnetic Vortex Gyration", Physical Review Letters **100**, 176601 (2008).

[147] L. Heyne, J. Rhensius, D. Ilgaz, A. Bisig, U. Rüdiger, M. Kläui, L. Joly, F. Nolting, L. J. Heyderman, J. U. Thiele, and F. Kronast, "Direct determination of large spin-torque nonadiabaticity in vortex core dynamics", Physical Review Letters **105**, 1–4 (2010).

[148] S. Finizio, C. Donnelly, S. Mayr, A. Hrabec, and J. Raabe, "Three-Dimensional Vortex Gyration Dynamics Unraveled by Time-Resolved Soft X-ray Laminography with Freely Selectable Excitation Frequencies", Nano Letters **22**, 1971–1977 (2022).

[149] G. Schütz, W. Wagner, W. Wilhelm, P. Kienle, R. Zeller, R. Frahm, and G. Materlik, "Absorption of circularly polarized x rays in iron", Physical Review Letters **58**, 737–740 (1987).

[150] M. Schofield, M. Beleggia, Y. Zhu, and G. Pozzi, "Characterization of JEOL 2100F Lorentz-TEM for low-magnification electron holography and magnetic imaging", Ultramicroscopy **108**, 625–634 (2008).

[151] M. Rahm, R. Höllinger, V. Umansky, and D. Weiss, "Influence of point defects on magnetic vortex structures", Journal of Applied Physics **95**, 6708–6710 (2004).

[152] M. Rahm, J. Stahl, W. Wegscheider, and D. Weiss, "Multistable switching due to magnetic vortices pinned at artificial pinning sites", Applied Physics Letters **85**, 1553–1555 (2004).

[153] K. Kuepper, L. Bischoff, C. Akhmadaliev, J. Fassbender, H. Stoll, K. W. Chou, A. Puzic, K. Fauth, D. Dolgos, G. Schütz, B. V. Waeyenberge, T. Tyliszczak, I. Neudecker, G. Woltersdorf, and C. H. Back, "Vortex dynamics in Permalloy disks with artificial defects: Suppression of the gyrotropic mode", Applied Physics Letters **90**, 062506 (2007).

[154] A. Vansteenkiste, J. D. Baerdemaeker, K. W. Chou, H. Stoll, M. Curcic, T. Tyliszczak, G. Woltersdorf, C. H. Back, G. Schütz, and B. V. Waeyenberge, "Influence of domain wall pinning on the dynamic behavior of magnetic vortex structures: Time-resolved scanning x-ray transmission microscopy in NiFe thin film structures", Physical Review B **77**, 144420 (2008).

[155] K. Y. Guslienko, R. H. Heredero, and O. Chubykalo-Fesenko, "Nonlinear gyrotropic vortex dynamics in ferromagnetic dots", Physical Review B **82**, 014402 (2010).

[156] C. Holl, M. Knol, M. Pratzer, J. Chico, I. L. Fernandes, S. Lounis, and M. Morgenstern, "Probing the pinning strength of magnetic vortex cores with sub-nanometer resolution", Nature Communications **11**, 2833 (2020).

[157] J. A. J. Burgess, A. E. Fraser, F. F. Sani, D. Vick, B. D. Hauer, J. P. Davis, and M. R. Freeman, "Quantitative Magneto-Mechanical Detection and Control of the Barkhausen Effect", Science **339**, 1051–1054 (2013).

[158] R. L. Compton and P. A. Crowell, "Dynamics of a Pinned Magnetic Vortex", Physical Review Letters **97**, 137202 (2006).

[159] R. L. Compton, T. Y. Chen, and P. A. Crowell, "Magnetic vortex dynamics in the presence of pinning", Physical Review B **81**, 144412 (2010).

[160] T. Y. Chen, M. J. Erickson, P. A. Crowell, and C. Leighton, "Surface Roughness Dominated Pinning Mechanism of Magnetic Vortices in Soft Ferromagnetic Films", Physical Review Letters **109**, 097202 (2012).

[161] R. Badea, J. Frey, and J. Berezovsky, "Magneto-optical imaging of vortex domain deformation in pinning sites", Journal of Magnetism and Magnetic Materials **381**, 463–469 (2015).

[162] R. Badea and J. Berezovsky, "Mapping the Landscape of Domain-Wall Pinning in Ferromagnetic Films Using Differential Magneto-Optical Microscopy", Physical Review Applied **5**, 064003 (2016).

[163] R. Badea, M. S. Wolf, and J. Berezovsky, "Exploiting bistable pinning of a ferromagnetic vortex for nitrogen-vacancy spin control", Applied Physics Letters **109**, 132403 (2016).

[164] J. Trimble and J. Berezovsky, "Barkhausen Imaging: A magneto-optical approach to mapping the pinning landscape in soft ferromagnetic films", Journal of Magnetism and Magnetic Materials **523**, 167585 (2021).

[165] H. Min, R. D. McMichael, M. J. Donahue, J. Miltat, and M. D. Stiles, "Effects of Disorder and Internal Dynamics on Vortex Wall Propagation", Physical Review Letters **104**, 217201 (2010).

[166] H. Min, R. D. McMichael, J. Miltat, and M. D. Stiles, "Effects of disorder on magnetic vortex gyration", Physical Review B **83**, 064411 (2011).

[167] A. Krasyuk, A. Oelsner, S. Nepijko, A. Kuksov, C. Schneider, and G. Schönhense, "Time-resolved photoemission electron microscopy of magnetic field and magnetisation changes", Applied Physics A **76**, 863–868 (2003).

[168] W. K. Hiebert, A. Stankiewicz, and M. R. Freeman, "Direct Observation of Magnetic Relaxation in a Small Permalloy Disk by Time-Resolved Scanning Kerr Microscopy", Physical Review Letters **79**, 1134–1137 (1997).

[169] P. Fischer, "Magnetic soft X-ray transmission microscopy", Current Opinion in Solid State and Materials Science **7**, 173–179 (2003).

[170] C. v. K. Schmising, B. Pfau, M. Schneider, C. M. Günther, M. Giovannella, J. Perron, B. Vodungbo, L. Müller, F. Capotondi, E. Pedersoli, N. Mahne, J. Lüning, and S. Eisebitt, "Imaging Ultrafast Demagnetization Dynamics after a Spatially Localized Optical Excitation", Physical Review Letters **112**, 217203 (2014).

[171] O. Kfir, S. Zayko, C. Nolte, M. Sivis, M. Möller, B. Hebler, S. S. P. K. Arekapudi, D. Steil, S. Schäfer, M. Albrecht, O. Cohen, S. Mathias, and C. Ropers, "Nanoscale magnetic imaging using circularly polarized high-harmonic radiation", Science Advances **3**, eaao4641 (2017).

[172] S. McVitie, D. McGrouther, S. McFadzean, D. MacLaren, K. O'Shea, and M. Benitez, "Aberration corrected Lorentz scanning transmission electron microscopy", Ultramicroscopy **152**, 57–62 (2015).

[173] N. Shibata, Y. Kohno, A. Nakamura, S. Morishita, T. Seki, A. Kumamoto, H. Sawada, T. Matsumoto, S. D. Findlay, and Y. Ikuhara, "Atomic resolution electron microscopy in a magnetic field free environment", Nature Communications **10**, 2308 (2019).

[174] H. Lichte and M. Lehmann, "Electron holography—basics and applications", Reports on Progress in Physics **71**, 016102 (2008).

[175] P. A. Midgley and R. E. Dunin-Borkowski, "Electron tomography and holography in materials science", Nature Materials **8**, 271–280 (2009).

[176] D. Wolf, L. A. Rodriguez, A. Béché, E. Javon, L. Serrano, C. Magen, C. Gatel, A. Lubk, H. Lichte, S. Bals, G. V. Tendeloo, A. Fernández-Pacheco, J. M. D. Teresa, and E. Snoeck, "3D Magnetic Induction Maps of Nanoscale Materials Revealed by Electron Holographic Tomography", Chemistry of Materials **27**, 6771–6778 (2015).

[177] G. Berruto, I. Madan, Y. Murooka, G. M. Vanacore, E. Pomarico, J. Rajeswari, R. Lamb, P. Huang, A. J. Kruchkov, Y. Togawa, T. LaGrange, D. McGrouther, H. M. Rønnow, and F. Carbone, "Laser-Induced Skyrmion Writing and Erasing in an Ultrafast Cryo-Lorentz Transmission Electron Microscope", Physical Review Letters **120**, 117201 (2018).

[178] F. J. T. Goncalves, G. W. Paterson, D. McGrouther, T. Drysdale, Y. Togawa, D. S. Schmool, and R. L. Stamps, "Probing microwave fields and enabling in-situ experiments in a transmission electron microscope", Scientific Reports **7**, 11064 (2017).

[179] M. Vogel, "Imaging of magnetization dynamics in temperature gradients", PhD thesis (2018).

[180] N. Browning, M. Bonds, G. Campbell, J. Evans, T. LaGrange, K. Jungjohann, D. Masiel, J. McKeown, S. Mehraeen, B. Reed, and M. Santala, "Recent developments in dynamic transmission electron microscopy", Current Opinion in Solid State and Materials Science **16**, 23–30 (2012).

[181] R. Frömter, F. Kloodt, S. Rößler, A. Frauen, P. Staeck, D. R. Cavicchia, L. Bocklage, V. Röbisch, E. Quandt, and H. P. Oepen, "Time-resolved scanning electron microscopy with polarization analysis", Applied Physics Letters **108**, 142401 (2016).

[182] A. Bisig, C. A. Akosa, J.-H. Moon, J. Rhensius, C. Moutafis, A. v. Bieren, J. Heidler, G. Kiliani, M. Kammerer, M. Curcic, M. Weigand, T. Tyliszczak, B. V. Waeyenberge, H. Stoll, G. Schütz, K.-J. Lee, A. Manchon, and M. Kläui, "Enhanced Nonadiabaticity in Vortex Cores due to the Emergent Hall Effect", Physical Review Letters **117**, 277203 (2016).

[183] J. Zweck, "Imaging of magnetic and electric fields by electron microscopy", Journal of Physics: Condensed Matter **28**, 403001 (2016).

[184] Supplementary moives are available at: https://doi.org/10.1038/s42005-020-0301-y.

[185] B. V. d. Wiele, L. Laurson, and G. Durin, "Effect of disorder on transverse domain wall dynamics in magnetic nanostrips", Physical Review B **86**, 144415 (2012).

[186] J. Leliaert, B. V. d. Wiele, A. Vansteenkiste, L. Laurson, G. Durin, L. Dupré, and B. V. Waeyenberge, "Influence of material defects on current-driven vortex domain wall mobility", Physical Review B **89**, 064419 (2014).

[187] A. Drews, B. Krüger, G. Selke, T. Kamionka, A. Vogel, M. Martens, U. Merkt, D. Möller, and G. Meier, "Nonlinear magnetic vortex gyration", Physical Review B **85**, 144417 (2012).

[188] S. E. Stevenson, C. Moutafis, G. Heldt, R. V. Chopdekar, C. Quitmann, L. J. Heyderman, and J. Raabe, "Dynamic stabilization of nonequilibrium domain configurations in magnetic squares with high amplitude excitations", Physical Review B **87**, 054423 (2013).

[189] K. Y. Guslienko, O. V. Sukhostavets, and D. V. Berkov, "Nonlinear magnetic vortex dynamics in a circular nanodot excited by spin-polarized current", Nanoscale Research Letters **9**, 386 (2014).

[190] B. Efron, "Bootstrap Methods: Another Look at the Jackknife", The Annals of Statistics **7**, 1–26 (1979).

[191] N. S. Kiselev, A. N. Bogdanov, R. Schäfer, and U. K. Rößler, "Chiral skyrmions in thin magnetic films: new objects for magnetic storage technologies?", Journal of Physics D: Applied Physics **44**, 392001 (2011).

[192] A. Fert, N. Reyren, and V. Cros, "Magnetic skyrmions: advances in physics and potential applications", Nature Reviews Materials **2**, 17031 (2017).

[193] S. Woo, K. Litzius, B. Krüger, M.-Y. Im, L. Caretta, K. Richter, M. Mann, A. Krone, R. M. Reeve, M. Weigand, P. Agrawal, I. Lemesh, M.-A. Mawass, P. Fischer, M. Kläui, and G. S. D. Beach, "Observation of room-temperature magnetic skyrmions and their current-driven dynamics in ultrathin metallic ferromagnets", Nature Materials **15**, 501–506 (2016).

[194] S. G. Je, P. Vallobra, T. Srivastava, J. C. Rojas-Sánchez, T. H. Pham, M. Hehn, G. Malinowski, C. Baraduc, S. Auffret, G. Gaudin, S. Mangin, H. B\'ea, and O. Boulle, "Creation of Magnetic Skyrmion Bubble Lattices by Ultrafast Laser in Ultrathin Films", Nano Letters **18**, 7362–7371 (2018).

[195] T. Y. Chen, A. T. Galkiewicz, and P. A. Crowell, "Phase diagram of magnetic vortex dynamics", Physical Review B **85**, 180406(R) (2012).

[196] J.-S. Kim, O. Boulle, S. Verstoep, L. Heyne, J. Rhensius, M. Kläui, L. J. Heyderman, F. Kronast, R. Mattheis, C. Ulysse, and G. Faini, "Current-induced vortex dynamics and pinning potentials probed by homodyne detection", Physical Review B **82**, 104427 (2010).

[197] C. Hanneken, A. Kubetzka, K. v. Bergmann, and R. Wiesendanger, "Pinning and movement of individual nanoscale magnetic skyrmions via defects", New Journal of Physics **18**, 055009 (2016).

[198] M. Möller, J. H. Gaida, S. Schäfer, and C. Ropers, "Few-nm tracking of current-driven magnetic vortex orbits using ultrafast Lorentz microscopy", Communications Physics **3**, 36 (2020).

[199] A. Goshtasby, "Image registration by local approximation methods", Image and Vision Computing **6**, 255–261 (1988).

[200] D.-T. Ngo and S. McVitie, "Visualization of vortex core polarity in NiFe nanodots by tilted Fresnel images", Ultramicroscopy **111**, 1276–1285 (2011).

[201] Supplementary moives are available at: https://link.aps.org/supplemental/10.1103/PhysRevResearch.4.013027.

[202] R. P. Heilbronner, "The autocorrelation function: an image processing tool for fabric analysis", Tectonophysics **212**, 351–370 (1992).

[203] B. Zang, K. Suzuki, and A. C. Liu, "Estimation of volume-weighted average grain size in Fe-based nanocrystalline soft magnetic materials by autocorrelation function", Materials Characterization **142**, 577–583 (2018).

[204] Y. Yin, F. Pan, M. Ahlberg, M. Ranjbar, P. Dürrenfeld, A. Houshang, M. Haidar, L. Bergqvist, Y. Zhai, R. K. Dumas, A. Delin, and J. Åkerman, "Tunable permalloy-based films for magnonic devices", Physical Review B **92**, 024427 (2015).

[205] G. d. Loubens, A. Riegler, B. Pigeau, F. Lochner, F. Boust, K. Y. Guslienko, H. Hurdequint, L. W. Molenkamp, G. Schmidt, A. N. Slavin, V. S. Tiberkevich, N. Vukadinovic, and O. Klein, "Bistability of Vortex Core Dynamics in a Single Perpendicularly Magnetized Nanodisk", Physical Review Letters **102**, 177602 (2009).

[206] R. Badea, E. Haber, and J. Berezovsky, "Stochastic Dynamics of a Ferromagnetic Vortex Revealed by Single-Spin Magnetometry", Physical Review Applied **10**, 064031 (2018).

[207] O. Gal, *fit_ellipse - File Exchange - MATLAB Central*.

[208] W. W. Mullins, "Theory of Thermal Grooving", Journal of Applied Physics **28**, 333–339 (1957).

[209] W. Mullins, "The effect of thermal grooving on grain boundary motion", Acta Metallurgica **6**, 414–427 (1958).

[210] M. J. Rost, D. A. Quist, and J. W. M. Frenken, "Grains, Growth, and Grooving", Physical Review Letters **91**, 026101 (2003).

[211] T. Malis, S. C. Cheng, and R. F. Egerton, "EELS log-ratio technique for specimen-thickness measurement in the TEM", Journal of Electron Microscopy Technique **8**, 193–200 (1988).

[212] R. Egerton, *Electron Energy-Loss Spectroscopy in the Electron Microscope* (2011).

[213] K. Iakoubovskii, K. Mitsuishi, Y. Nakayama, and K. Furuya, "Thickness measurements with electron energy loss spectroscopy", Microscopy Research and Technique **71**, 626–631 (2008).

[214] C. Bai, *Scanning tunneling microscopy and its application*, Vol. 32 (Springer Science & Business Media, 2000).

[215] P. Eaton and P. West, *Atomic force microscopy* (Oxford university press).

[216] J. Moreland, "Micromechanical instruments for ferromagnetic measurements", Journal of Physics D: Applied Physics **36**, R39 (2003).

[217] J. P. Davis, D. Vick, P. Li, S. K. N. Portillo, A. E. Fraser, J. A. J. Burgess, D. C. Fortin, W. K. Hiebert, and M. R. Freeman, "Nanomechanical torsional resonator torque magnetometry (invited)", Journal of Applied Physics **109**, 07D309 (2011).

[218] T. Uhlig, M. Heumann, and J. Zweck, "Development of a specimen holder for in situ generation of pure in-plane magnetic fields in a transmission electron microscope.", Ultramicroscopy **94**, 193–6 (2003).

[219] M. Arita, R. Tokuda, K. Hamada, and Y. Takahashi, "Development of TEM Holder Generating In-Plane Magnetic Field Used for In-Situ TEM Observation", MATERIALS TRANSACTIONS **55**, 403–409 (2014).

[220] A. Sugawara, T. Shimakura, H. Nishihara, T. Akashi, Y. Takahashi, N. Moriya, and M. Sugaya, "A 0.5-T pure-in-plane-field magnetizing holder for in-situ Lorentz microscopy.", Ultramicroscopy **197**, 105–111 (2018).

[221] D. Arthur and S. Vassilvitskii, *k-means++: The Advantages of Careful Seeding*, Technical Report 2006-13 (Stanford InfoLab).

[222] M. Möller, J. H. Gaida, and C. Ropers, "Pinning and gyration dynamics of magnetic vortices revealed by correlative Lorentz and bright-field imaging", Physical Review Research **4**, 013027 (2022).

[223] T. Nagai, K. Kimoto, K. Inoke, and M. Takeguchi, "Real-space observation of nanoscale magnetic phase separation in dysprosium by aberration-corrected Lorentz microscopy", Physical Review B **96**, 100405 (2017).

[224] D. Paganin and K. a. Nugent, "Noninterferometric phase imaging with partially coherent light", Physical Review Letters **80**, 2586–2589 (1998).

[225] T. Zhou, M. Cherukara, and C. Phatak, "Differential programming enabled functional imaging with Lorentz transmission electron microscopy", npj Computational Materials **7**, 141 (2021).

[226] V. Boureau, M. Staňo, J.-L. Rouvière, J.-C. Toussaint, O. Fruchart, and D. Cooper, "High-sensitivity mapping of magnetic induction fields with nanometer-scale resolution: comparison of off-axis electron holography and pixelated differential phase contrast", Journal of Physics D: Applied Physics **54**, 085001 (2020).

[227] D. GABOR, "A New Microscopic Principle", Nature **161**, 777–778 (1948).

[228] M. E. Haine and T. Mulvey, "The Formation of the Diffraction Image with Electrons in the Gabor Diffraction Microscope", Journal of the Optical Society of America **42**, 763 (1952).

[229] G. Möllenstedt and H. Düker, "Fresnelscher Interferenzversuch mit einem Biprisma für Elektronenwellen", Naturwissenschaften **42**, 41–41 (1955).

[230] T. Tanigaki, T. Akashi, T. Yoshida, K. Harada, K. Ishizuka, M. Ichimura, Y. Murakami, K. Mitsuishi, Y. Tomioka, D. Shindo, X. Yu, Y. Tokura, and H. Shinada, "In-Plane Magnetic Field Evaluation with 0.47-nm Resolution by Aberration-Corrected 1.2-MV Holography Electron Microscope", Microscopy and Microanalysis **25**, 54–55 (2019).

[231] J. Zweck, J. Chapman, S. McVitie, and H. Hoffmann, "Reconstruction of induction distributions in thin films from DPC images", Journal of Magnetism and Magnetic Materials **104**, 315–316 (1992).

[232] N. J. Zaluzec, "Quantitative Measurements of Magnetic Vortices using Position Resolved Diffraction in Lorentz Stem", Microscopy and Microanalysis **8**, 376–377 (2002).

[233] C. Ophus, "Four-Dimensional Scanning Transmission Electron Microscopy (4D-STEM): From Scanning Nanodiffraction to Ptychography and Beyond", Microscopy and Microanalysis **25**, 563–582 (2019).

[234] M. W. Tate, P. Purohit, D. Chamberlain, K. X. Nguyen, R. Hovden, C. S. Chang, P. Deb, E. Turgut, J. T. Heron, D. G. Schlom, D. C. Ralph, G. D. Fuchs, K. S. Shanks, H. T. Philipp, D. A. Muller, and S. M. Gruner, "High Dynamic Range Pixel Array Detector for Scanning Transmission Electron Microscopy", Microscopy and Microanalysis **22**, 237–249 (2016).

[235] J. A. Mir, R. Clough, R. MacInnes, C. Gough, R. Plackett, I. Shipsey, H. Sawada, I. MacLaren, R. Ballabriga, D. Maneuski, V. O'Shea, D. McGrouther, and A. I. Kirkland, "Characterisation of the Medipix3 detector for 60 and 80keV electrons.", Ultramicroscopy **182**, 44–53 (2016).

[236] K. X. Nguyen, X. S. Zhang, E. Turgut, M. C. Cao, J. Glaser, Z. Chen, M. J. Stolt, C. S. Chang, Y.-T. Shao, S. Jin, G. D. Fuchs, and D. A. Muller, "Disentangling Magnetic and Grain Contrast in Polycrystalline FeGe Thin Films Using Four-Dimensional Lorentz Scanning Transmission Electron Microscopy", Physical Review Applied **17**, 034066 (2022).

[237] Z. Chen, E. Turgut, Y. Jiang, K. X. Nguyen, G. C. Correa, M. J. Stolt, S. Jin, D. C. Ralph, G. D. Fuchs, and D. A. Muller, "Resolving Internal Magnetic Structures of Skyrmions by Lorentz Electron Ptychography", Microscopy and Microanalysis **25**, 32–33 (2019).

[238] P. M. Pelz, W. X. Qiu, R. Bücker, G. Kassier, and R. J. D. Miller, "Low-dose cryo electron ptychography via non-convex Bayesian optimization", Scientific Reports **7**, 9883 (2017).

[239] L. Zhou, J. Song, J. S. Kim, X. Pei, C. Huang, M. Boyce, L. Mendonça, D. Clare, A. Siebert, C. S. Allen, E. Liberti, D. Stuart, X. Pan, P. D. Nellist, P. Zhang, A. I. Kirkland, and P. Wang, "Low-dose phase retrieval of biological specimens using cryo-electron ptychography", Nature Communications **11**, 2773 (2020).